עבודת גמר (תזה) לתואר
דוקטור לפילוסופיה

מוגשת למועצה המדעית של
מכון ויצמן למדע
רחובות, ישראל

Thesis for the degree
Doctor of Philosophy

Submitted to the Scientific Council of the
Weizmann Institute of Science
Rehovot, Israel

מאת
ליאורה חנה שיין-לובומירסקי

By
Leora Hannah Schein-Lubomirsky

תהודה מגנטית גרעינית - מדימות מבוסס גזרת מגנטית ועד מדידת משטחים מולקולרים - הדרך לגרעין-דימות מגנטי משטחי

Nanoscale magnetic resonance – from gradient magnetic field imaging to sensing molecular surfaces – towards nanoscale surface magnetic resonance imaging

מנחה:
ד"ר עמית פינקלר

Advisor:
Dr. Amit Finkler

אייר , ה'תשפ"ה

April, 2025

In memory of Dr. Zechariah Haber[1] OB"M, who made every moment matter.

Contents

Listing of figures

Abstract

The discovery of magnetic resonance has enabled the development of a toolbox for studying structure and composition of samples ranging from molecules to solid powders. Within this toolbox, magnetic resonance imaging, or MRI, has changed medicine by giving the ability to image structure and composition of human organs in a non-invasive manner. The vision to bring this accomplishment to the nanoscale and provide imaging of individual proteins and nano-structures, such as molecular monolayers, is under pursuit by a variety of methods. This field is known as nanoMRI.

Chiral induced spin selectivity (CISS) is a phenomenon describing the preferential interaction between "handedness" and spin orientation in organic chiral molecules. It has been observed in two main settings, one is in electron transport through the chiral molecule and the other in adhesion on ferromagnets, and in a two-dimensional electron gas (2DEG) where magnetic effects are observed. The underlying mechanism is not fully understood, and specifically the role of spin-orbit coupling (SOC) and the role of the surface are open questions.

The nitrogen-vacancy (NV) center in diamond, an atomic defect, stands out as a magnetic sensor that can be used to conceive a technique for nanoMRI. Research on the NV center has advanced over the past decades providing sensing protocols for detecting electron and nuclear spins and enabling the use of single NVs at room temperature. Existing methods for nanoMRI using NV centers have limited contrast due to the detrimental effect of permanent magnetic fields that are not aligned with the NV center axis. Other NV based methods do not provide flexibility in the position of the magnetic field and are limited in the amplitude of the gradient.

In this thesis, I developed and implemented a method for nanoMRI that overcomes the drawbacks of a permanent magnet and provides temporal and spatial flexibility of the magnetic field. I developed a current focusing device (CFD) in the form of a wire that is deposited along a quartz tip, controlled by atomic force microscopy (AFM) feedback for surface proximity and incorporated in an NV confocal microscope. Heat simulations show that an apex on the order of 1300 nm is required to sustain the current without damage to the device. At the same time, magnetic field simulations show the field is expected to be weak and not interfere with the readout as with a permanent magnetic. I present measurements of the of the magnetic field and show that for a pulsed current of 1.54 mA the gradient achieved is 1 μT/nm. Additionally, a destructive current ramp showed the device can sustain a current up 13.4 mA which allows more than 8-fold increase in the gradient. Using the low current gradient, electrons can be images with a resolution of 3.6 nm. A modification of the Rabi time of the NV was also shown to occur due to the proximity of the tip to the

surface. An increase of 3.5-fold was measured relative to the base line Rabi time - this allows shorter Rabi times without increasing microwave (MW) power thus avoiding heating. Additionally, the Rabi power spatial dependence can be used in the future for a second gradient method in which spins can be selectively addressed. The scanning electromagnet can be used beyond nanoMRI applications for applying local switchable electromagnetic fields.

A second aspect of nanoscale magnetic resonance that is studied in this thesis is sensing self-assembled monolayers (SAMs), where molecules are absorbed on a surface and have a uniform orientation. First, I developed protocols to form an SAM in the vicinity of the NV center. An SAM with a spin label, i.e., a free electron, is measured with the NV, yet the signal is masked by electrons native to the surface, highlighting the need to improve surface preparation. In addition, the magnetic nature of the surface adhesion shown in CISS motivated the study of a chiral SAM with the NV. A chiral SAM is formed on a 2 nm layer on alumina that is on the diamond and magnetic fluctuations are shown to increase under the adsorption of the chiral monolayer. These measurements can be used to model the CISS effect whose mechanism is not fully understood.

In a broader perspective, the two aspects studied here, namely nanoMRI and molecular surfaces, can be combined. Together, one can image molecular surfaces and answer questions regarding structure and composition with nanoscale resolution and ideally image such molecular surfaces.

Acknowledgments

I would like to thank my advisor Dr. Amit Finkler for the continuous support throughout my Ph.D research. For giving me the opportunity to explore, having my back when I want to try a new research direction and assisting with everything from science to administration. For teaching me to "just do it", that only natures laws stand in our way, to be creative when finding solutions, to try methods from the simple to the technically challenging, to dream big.

Thank you to my group members who first and foremost friends with whom I shared frustration and success. Thanks for the many scientific discussions, without you I would not have come this far and the way would have been dull. To Dr. Dan Yudilevich, Dr. Jitender Kumar, Dr. Inbar Zohar, Ariel Smooha, John Woodrow Rosenberg and Asad Awadalla. And to the new members that made the final days optimistic, to Eyal Laster, Ariel Nakav and Nadav Deutsch.

Thank you to the many people who made this work possible - To Dr. Yuri Myasoedov for all assistance with tip fabrication; To Haim sede, Alex Jahanfard and Alexander Kuprienko for solving all fabrication challenges; To Dr. Hagai Cohen and Dr. Tatyana Bendikov for XPS measurements and detailed explanations; To Dr. Anu Gupta and Dr. Francesco Tassinari for collaborating to measure chiral samples; To Dr. Yarden Mazor for the fruitful collaboration and theoretical insight; To Kayta Rachav for the tedious time spent working on the FIB; To the clean room staff - Assaf Hazzan, Leonid Tunik, Sharon Garusi and Alex Yoffe for training, guidance and insight.

Thank you to my parents who believe I can pursuit any dream. Thank you to Yuri, who makes me smile every day and to my children, Eden, Boaz, Maya and Roni who make it all worthwhile.

Declaration

I hereby declare that this thesis summarizes my own independent research. I certify that, to the best of my knowledge and belief, this work contains no material that was previously published or written by another person except where due reference has been made in the text.
The following is the list of contributions by other authors:

- Dr. Andrej Denisenko and Dr. Rainer Stöhr, Physikalisches Institut, Universität Stuttgart, fabricated the diamond membrane used in the experiment of Chapter 4.
- Dr. Yarden Mazor, School of Electrical Engineering, Tel Aviv University performed the theoretical analysis and simulation of the Rabi enhancement in Chapter 4.7 and in Appendix D.
- The setup used to fabricate the tip was developed in the lab of Prof. Eli Zeldov with the assistance of Dr. Yuri Myasoedov and the students in the lab.
- Dr. Dan Yudilevich, Department of Chemical and Biological Physics, WIS, contributed to the automation and control software discussed in Chapter 2.
- The chiral SAM preparation in Ch. 5.3 was performed by Dr. Anu Gupta from the lab of Prof. Ron Naaman.
- Ariel Samooha, Department of Chemical and Biological Physics, WIS, assisted with the surface characterization and measurements of the spin radical in 5.2.
- Dr. Sidney Cohen conducted the AFM measurement on the tip described in Ch. 5.
- XPS measurements were performed by Dr. Hagai Cohen and Dr. Tatyana Bendikov, Department of Chemical Research Support, WIS.
- The Weizmann Instrument Design Unit designed the tip holder described in Ch. 3.

List of Abbreviations

Table 1: List of abbreviations used in the text.

AC	Alternating current
ALD	Atomic layer deposition
APD	Avalanche photodiode
AFM	Atomic force microscopy
AWG	Arbitrary waveform generator
CFD	Current focusing device
CVD	Chemical vapor deposition
DC	Direct current
DEER	Double electron-electron resonance
EPR	Electron paramagnetic resonance
ESR	Electron spin resonance
FOV	Field of view
FTIR	Fourier-transform infrared spectroscopy
MPA	3-Mercaptopropionic acid
MRFM	Magnetic resonance force microscopy
MW	Microwave
NMR	Nuclear magnetic resonance
NV	Nitrogen-vacancy
ODMR	Optically detected magnetic resonance
PL	Photoluminescence
PLL	phase locked loop
RF	Radio-frequency
RT	Room-temperature
SEM	Scanning electron microscope
SNR	Signal-to-noise ratio
SRIM	Stopping and range of ions in matter
UV	Ultra-violet
WIS	Weizmann Institute of Science
XPS	X-ray photoelectron spectroscopy

1 Introduction

Science is to the Objective
as Art is to the Subjective

L.H.SL

Surface science plays a central role in understanding systems ranging from two-dimensional materials and molecular monolayers to complex interfaces and biological membranes. A diverse array of techniques have been developed to study and characterize the physical, chemical, and structural properties of surfaces — including imaging methods and various forms of spectroscopy. Traditional techniques such as X-ray photoelectron spectroscopy[2] (XPS), Fourier-transform infrared spectroscopy[3] (FTIR), scanning electron microscopy[4] (SEM), confocal microscopy[5], and atomic force microscopy[6] (AFM) provide valuable insights into surface composition, molecular identity, and morphology. However, each method is typically limited either by spatial resolution, the specific physical properties it probes or by the averaging nature of the detection, which often spans micron-scale areas.

As surface science advances, increasingly detailed questions emerge: what is the precise arrangement of molecules at specific locations, how are molecular orientations distributed across a surface, and how uniform is a monolayer at the nanoscale? Conventional tools are not equipped to resolve these features at the single-molecule or nanometer level. In response, new sensing technologies are being developed[7,8,9] that exploit quantum sensors and molecular spin properties for highly localized, non-invasive measurements. These emerging methods have the potential to transform our ability to image, characterize, and manipulate surfaces with unprecedented resolution.

More broadly, studying science and technology at the nanometer scale and beyond has advanced

our understanding of the world and achieved technological leaps over the past few decades. We have learned to study interactions and structures that occur at the nanoscale and influence macroscopic phenomena, from electronic devices to molecular interactions. A variety of techniques exist to probe nano-phenomena, each leveraging different fundamental properties, such as charge, force, or light. Among the physical properties that can be exploited for nanoscale sensing, magnetic interactions offer a particularly valuable opportunity. Magnetism is of interest both from the perspective of basic science and for technological applications. It can be used as a tool to study nature, such as molecular structure in nuclear magnetic resonance (NMR), and it is a natural force in and of itself that is of interest.

Several tools exist for nanoscale magnetometry, such as the superconducting quantum interference device (SQUID)[10], magnetic force microscopy (MFM)[11] and nitrogen-vacancy (NV) centers in diamond. The choice of technique depends on the sample that is studied as each method has specific advantages. SQUID microscopy uses a scanning tip, which works at low temperatures and is utilized to scan nanostructures and measure the magnetic field. MFM combines atomic force measurements with a magnetic AFM tip to detect the magnetic force between the sample and the tip the sample surface.

The NV center is an atomic defect in diamond and can be used as a magnetic sensor[12,13]. It has several working methods - scanning tip where the NV is within a tip placed above the sample, nanodiamonds that are placed within a sample, or as a thin membrane surface where a sample is placed atop it. Diamonds have many advantages for sensing - they are bio-compatible, they function at both low temperatures and room temperature, they can be synthesized in a controlled manner, and they provide high spatial resolution. Magnetic sensing using NV centers is the workhorse of this work.

This thesis explores two key aspects of nanoscale magnetometry, each introduced in the sections that follow. Sec. 1.1 presents nanoscale magnetic resonance imaging (nanoMRI) as a method for spatially resolved magnetic sensing with nanometer precision. The principle of magnetic resonance imaging is introduced, and existing approaches to nanoMRI are reviewed. The second topic addressed in this work is sensing magnetic properties of molecular surface using the NV sensor and is discussed in Sec. 1.2. Finally, Sec. 1.3 introduces chiral-induced spin selectivity (CISS), an effect which couples spin to molecular handedness and is observed in a monolayer of chiral molecules. The magnetic properties of a chiral monolayer are studied in this work with the NV sensor. This introduction builds the motivation for the goals that conclude this chapter and are presented in Sec. 1.4.

1.1 nanoMRI

Magnetic resonance imaging (MRI) is a form of magnetic sensing, and it has had a profound effect on medicine today, giving humanity the ability to image a cross-section of the human body and see what is inaccessible to the eye[14]. It relies on the physics of magnetic resonance, the physics that describes the response of a spin to a magnetic field, which can be modeled as a precession of the spin probability at a natural frequency (see Fig. 1.1), known as the Larmor frequency, of

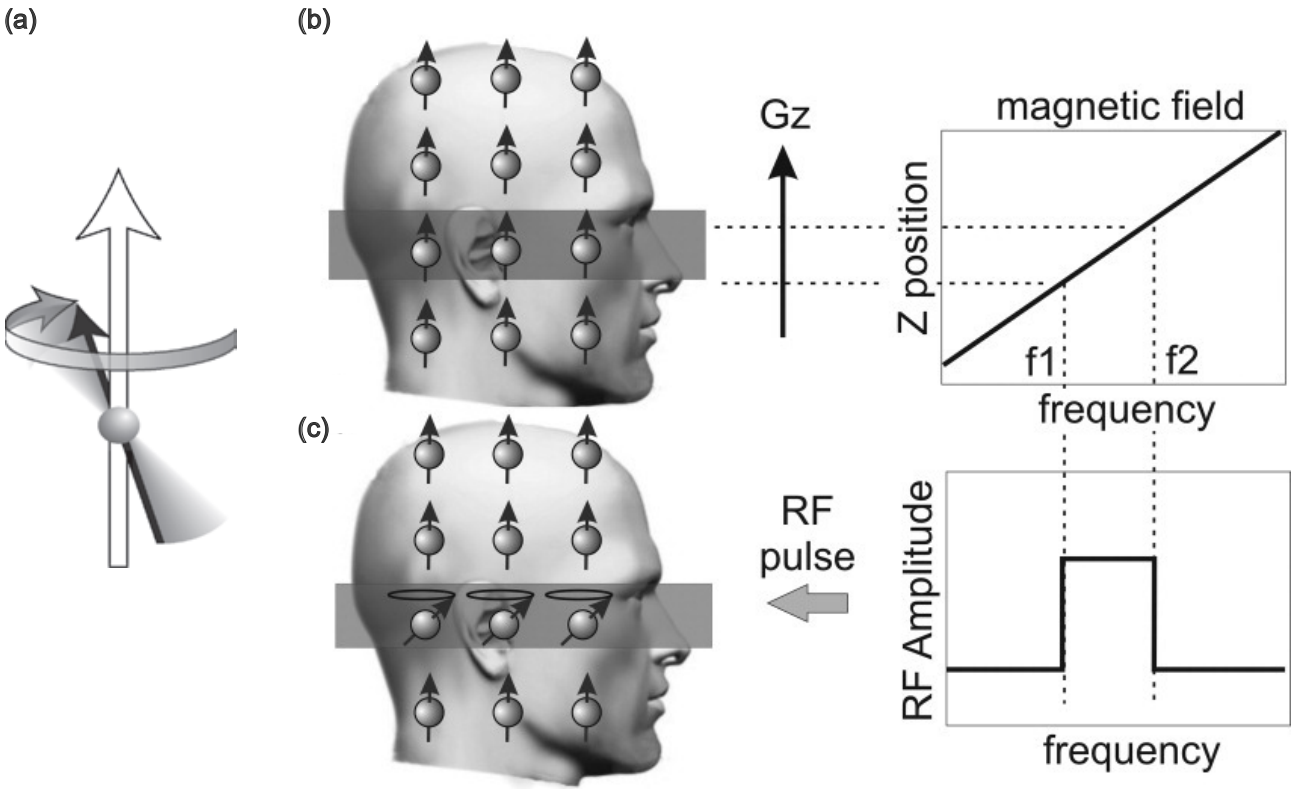

Figure 1.1: Schematic of MRI principle. (a) A spin in the presence of a magnetic field can be described as a precession around the axis of the magnetic, the rate, known as the Larmor frequency, is $\vec{f} = \gamma\vec{B}$. The figure is from "Spin Dynamics", M. Levitt[18]. (b,c) Schematic of principle of MRI. (b) The spins in the sample are initially aligned according to an external magnetite field. A gradient magnetic field is applied to the spins, shifting the local resonance of each spin. (c) An RF pulse that is applied and rotates only the spins that are on resonance with the pulse, this selects a specific slice within the sample. Image from "Physics of MRI: A primer", D. B. Plewes and W. Kucharczyk[17].

$f(\vec{r}) = \gamma_i B(\vec{r})$, where γ_i is the gyro-magnetic ratio of the detected species and $B(\vec{r})$ is the magnetic field[15]. Detecting this frequency gives information about the chemical structure of the sample, in NMR this is most often a liquid solution. Image reconstruction[16,17] is achieved by adding another step and applying a non-uniform magnetic field around the sample, such as the human brain. With such a gradient in the magnetic field, spins at different locations in the sample will precess at different rates, thus coupling frequency information to spatial information. Typically, in medical devices, the gradient field is on the order of 10 mT/m.

Nano-MRI aims to achieve similar structural insight for samples at the nanoscale and down to the single-molecule level. It has the potential to gain insight in the vast world of chemistry, biology and physics where conventional nuclear magnetic resonance (NMR) is limited by sample size[19] and conventional MRI is limited by magnetic field gradients to the micron scale[20]. A variety of techniques exist in the field of nanoMRI, among them are - magnetic resonance force microscopy (MRFM)[21], electron spin resonance using scanning tunneling microscopy (ESR-STM)[22], a recently published method based on electron spin resonance using atomic force microscopy (ESR-AFM)[23] and the nitrogen-vacancy (NV) center in diamond.

In MRFM force measurements detect the resonance excitation of the molecular sample, the main limitation being the smallest detectable force which in turn limits the sample size. Modern cantilevers allow detection of about 10^2 molecules[7] with an impressive 10 nm resolution[24,25].

Additional gradients were applied by a focused planar device below the AFM tip, resulting in resolution better than 2 nm[26]. Alternatively, in ESR-STM the sample is detected by its tunneling interaction with the STM atomic tip[7,27]. ESR-STM is limited by its sensitivity and the type of systems that can currently be explored, future techniques which enable the indirect sample detection are expected to advance this method. Both techniques, despite achieving significant milestones, remain technically demanding, such that each new sample presents a unique set of challenges.

NV center-based magnetometry is a leading technique for magnetic resonance detection[7,28,13] and has advanced significantly from the initial work showing the potential ability to measure magnetic resonance[12]. The NV is an atomic solid state defect in diamond that can be used as a magnetic sensor due to its interaction with the environment combined with the ability to control and read out its state. Experiments measuring nuclear magnetic resonance (NMR) signals with nanoscale sample size detecting as few as 10^4 nuclear spins[29,30] have been reported. In these experiments, the signal is integrated over all the spins interacting with the NV. The opportunity to resolve spatial information, i.e., nanoMRI, by applying local gradients to NVs, was not overlooked and was demonstrated by Grinolds et al.[31] In this work, a ferromagnetic tip was placed in the vicinity of the NV to induce strong gradients and enable nanoMRI. The subnanometer resolution achieved is impressive, yet its Achilles' heel lies in the arbitrary direction and permanency of the magnetic field of the ferromagnet. The NV center possesses a natural symmetry axis determined by the diamond lattice and the orientation of the defect. This axis defines the system's eigenstates in the absence of an external magnetic field. However, when magnetic fields are applied at an angle to this axis, the eigenstates are mixed, leading to a substantial reduction in readout contrast[32]— to the extent that sample detection becomes impractical. Consequently, there remains a strong need for robust techniques in nanoscale MRI.

Current-induced magnetic fields provide an opportunity to overcome this challenge. The Biot-Savart law (Eq. 3.2) tells us that a current running through a wire will induce a magnetic field around it. Such a current can be used to control the magnetic field, by switching it on and off throughout the experiment - thus avoiding the detrimental off-axis fields that hinder NV sensing. In this way, we can have a strong gradient that will not hinder the NV contrast, and imaging will be practical.

1.2 Molecular surface and sample challenges

ESR (electron spin resonance)[33] is a fundamental tool used to study molecular structure and chemical composition. Similar to such studies using ESR on macroscopic samples, this interaction can be used to study molecular structure and properties at the nanoscale using the single NV as a MR sensor. Studying spins external to the diamond with magnetic resonance tools is an ongoing pursuit in quantum sensing with single NVs. In contrast to proof of concept detection within the diamond, studying external spins utilizes the NV sensor a tool to examine new scientific realms To achieve this, the sample must be placed in close vicinity to the NV center, since the dipole-

dipole[34,35] interaction decreases with r^3 (Eq. 1.1).

$$\mathcal{H} = -\sum_i \frac{\mu_0 \gamma_{e,i} \gamma_{NV} \hbar^2}{4\pi |r|^3} (3(S_{NV} \cdot \hat{r})(S_{e,i} \cdot \hat{r}) - S_{NV} \cdot S_{e,i}) \tag{1.1}$$

Eq. 1.1 describes the dipole-dipole interaction where $\gamma_{i(NV)}$ is the gyromagnetic ratio for the i-th electron (NV), $S_{i(NV)}$ is the spin of the i-th electron (NV) and r is the vector connecting the sample electron to the NV. For a field aligned with the NV, this term can be written as

$$\mathcal{H} = -\sum_i \frac{\mu_0 \gamma_{e,i} \gamma_{NV} \hbar^2}{4\pi |r|^3} (3\cos^2 \theta_{i-NV} - 1) \tag{1.2}$$

Detecting external electron spins has been demonstrated in several works, some examine electrons native to the diamond surface[36], others study electrons from a polymer layer that was spin coated on the diamond[37,38]. Direct chemical bonding to the diamond was demonstrated by Grotz et al.[34], where the diamond surface was boronated, followed by silane chemistry as a linker to a free radical. An alternative surface modification allowed amine bonds on the surface, which were leveraged for nuclear sensing[39]. However, functionalization of the diamond surface is challenging[40,41], may suffer from low efficiency[42] and it is not clear it forms a uniform monolayer structure[43]. A variety of chemical terminations are native to the diamond surface, and all these affect the NV centers. Particularly, some attract charge states on the surface[44]. These challenges have led to an alternative route to direct bonding where a thin alumina layer is deposited on the surface and a monolayer is created on the oxide[45]. NMR sensing was demonstrated on this surface using ensembles of NV which provide resolution on the micron scale[46,8,9]. Increased resolution down to nanoscale magnetic resonance (MR) sensing is of interest and can be achieved using single NV centers[29]. However, sensing surfaces with single NVs presents distinct challenges compared to ensemble-based approaches, primarily due to the lower signal-to-noise ratio. In ensembles, the collective response of multiple NV centers enhances the overall signal, whereas single NV sensing requires strategies to maximize signal strength. Consequently, minimizing the NV-sample distance is crucial. Developing novel molecular adhesion techniques will expand the range of detectable molecular samples, specifically with different chemical terminations. Furthermore, demonstrating the detection of electron spins attached to the diamond surface but separated by a bonding layer will contribute to advancements in nanoscale MR sensing.

1.3 Chiral induced spin selectivity

Chiral-Induced Spin Selectivity (CISS) refers to the phenomenon in which electron spin becomes coupled to molecular chirality[47], leading to spin-selective transport through chiral organic molecules. This effect is typically observed in systems where chiral molecules form a self-assembled monolayer (SAM) on a substrate, resulting in a uniform molecular orientation. It has been demonstrated that when electrons pass through such a monolayer, their transmission efficiency depends on the alignment between their spin and the molecular chirality. In this context, the chiral molecule behaves as

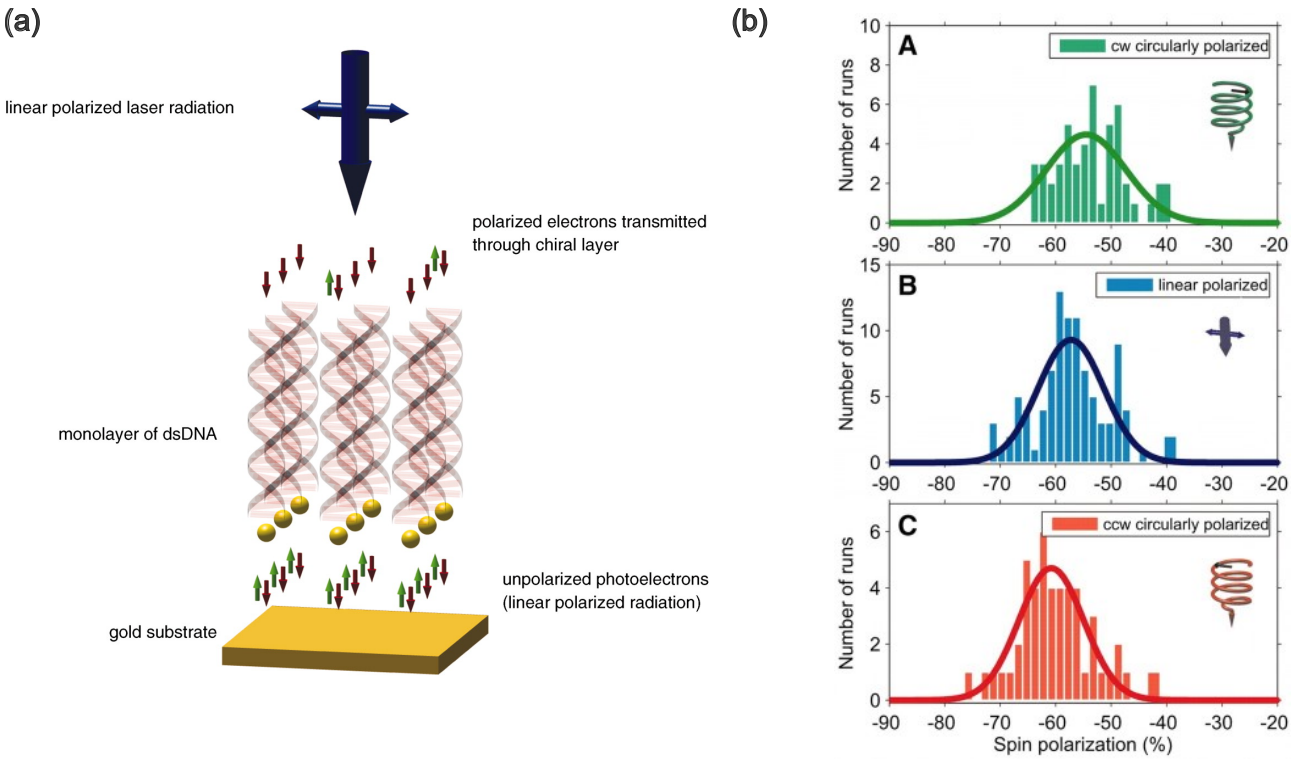

Figure 1.2: Figure from Göhler et al.[49]. (a) Schematic of the experiment measuring spin polarization of photo-emitted electrons transmitted through a chiral monolayer. Polarized light excites electrons from a gold substrate, the excited electrons have a specific polarization defined by the light. They then travel through the layer of chiral molecules and their polarization is measured at the other side (b). Measurements of the polarization of electrons after passing through the organic chiral monolayer for three different initial light polarizations. The measured polarization is independent on the initial polarization of the electrons (as determined by the excitation light) and depends on the molecular chirality.

a spin filter, preferentially transmitting electrons whose spin orientation matches the handedness of the molecule.

Early experiments[48,49] uncovered the phenomena when observing the effect of chiral molecules on electron transport. In these experiments, photoexcited electrons were transported through a mono-layer of chiral molecules (double-stranded DNA) and the polarization of the electrons was measured. It was shown that the after the chiral monolayer the electrons have a preferred polarization and that this depends on the chirality of the mono-layer (see Fig.1.2). In a second experiment[50], a transport measurement was conducted for a current going through a chiral molecular layer adhered to a ferromagnet (FM). It was shown that the current strength depends on the alignment of the ferromagnet with the handedness of the chiral molecules.

Other experiments examined the effect of chiral molecules on surface magnetization. One such experiment demonstrated[51] that chiral molecules adsorbed on a ferromagnetic surface can control the magnetization of the ferromagnetic. The molecules adsorbed on the surface dictate the polarization of the electrons on the surface, and due to the chirality, there is a preferred spin direction according to the handedness. This, in turn, determines the magnetization of the ferromagnet in the region below the polarized molecules, shown schematically in Fig. 1.3(b). A second experiment[52] achieved magnetization in a non-magnetic structure composed of chiral molecules above a semiconductor hosting a two-dimensional electron gas (2DEG). A voltage was applied between

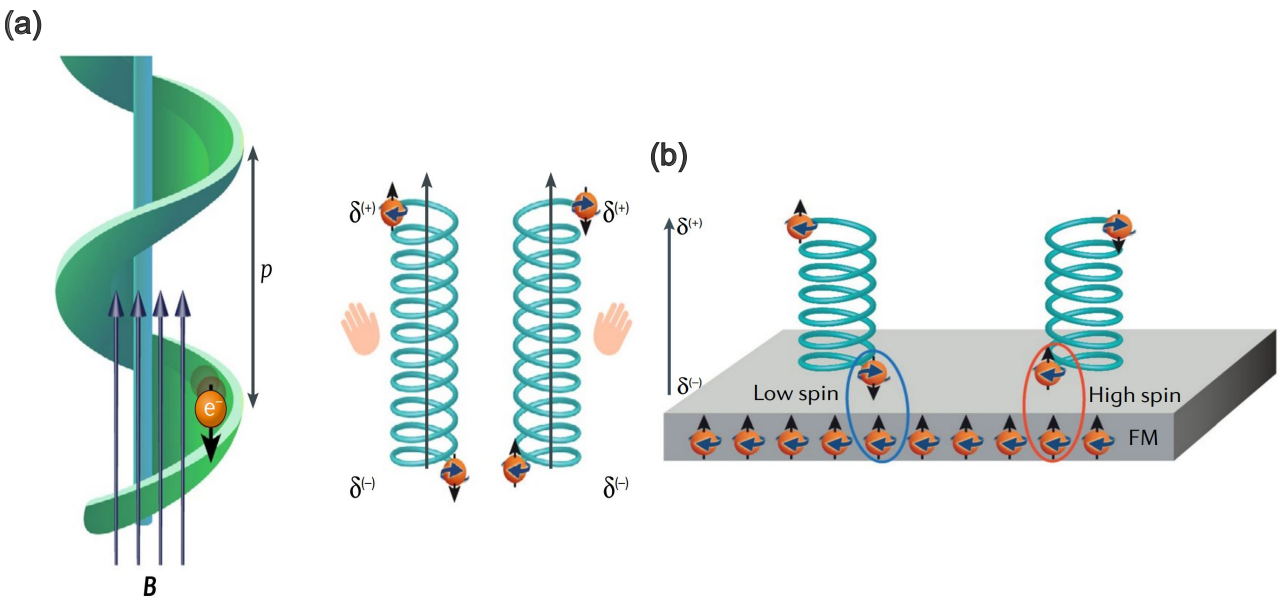

Figure 1.3: Schematic CISS mechanism from Naaman et al.[54]. (a) Schematic coupling between the electron transport to the molecular handedness where the molecule applies an effective magnetic field and interacts with the electron spin such that a specific spin orientation is preferentially transported. (b) Schematic coupling between the molecular handedness to the spins in a ferromagnetic surface.

the molecular layer and the 2DEG, which polarized the molecules and there was a charge transfer across the layers. It is thought that the charge transfer is spin-polarized according to the chirality. In turn, the semiconductor acts as a ferromagnet with the magnetization dictated by the chirality. Absorption of chiral molecules on a ferromagnet was studied with NV center ensembles[53]. It was demonstrated that the molecules induce a magnetization in the layer, and the direction depends on the direction of the chirality and the tilt angle of the monolayer.

These experiments paint a picture of the properties and interactions of the chiral molecules. In the transport experiment, the chiral molecule couples the spin orientation to the velocity, electrons with the "correct" spin orientation have a higher probability of transferring through the molecules. To explain the experimental results, the electron transport through the chiral molecule can be described as an effective magnetic field that depends on the handedness of the molecule and interacts with the spin. Spins with the preferred direction are stabilized and so their transport is promoted while spins with opposite direction are more likely to back scatter and their transport is suppressed[54], shown schematically in Fig. 1.3(a)[54]. In the surface measurements, where chirality induces magnetization there is a coupling between the spin polarization in the surface and the chirality

This understanding, however, does not give a precise description of the phenomena and does not provide quantitative predictions, as such there are still open questions regarding the fundamental mechanism[55,47]. To overcome this gap several theoretical approaches were taken[56,57,58,59,60,61] yet there is no consensus as to the precise description. Some of the schemes describe a centripetal force[54] on the electron as it travels through the chiral molecule, this relates the chirality to the angular momentum of the electron. Many models assume that such interactions involve spin-orbit coupling (SOC)[47]. Yet the calculations of the SOC for such organic molecules give low values,

on the order of few meV[58,62]. This leaves the question as to how the interaction is strong, reflecting an effective strong SOC (on the order of hundreds of meV[63]), even though the SOC of the molecule is weak. Thus, the strength of the SOC remains one of the open questions regarding chiral molecules. One direction suggested is that the source of the strong SOC is orbital angular momentum of the electrons which come from the metal surface[62,64]. This motivates new measurements that observe CISS from different perspectives and can promote a more precise mechanism describing the interaction.

1.4 Research goals

In this work I use NV centers for nanoscale magnetometry to approach the following advances in the field:

1. **nanoMRI.** I aimed to develop a methodology that will allow nanoMRI and overcome the existing limitations. As such I developed a scanning electromagnetic tip that is incorporated in the NV setup. I aimed for the device to meet the following requirements:

    - **Strong gradient**. The gradient required was one that can differentiate electrons spaced at a distance of 1 nm, for that we required a field gradient strength of 1 $\mu T\,nm^{-1}$.
    - **Controllable within the time frame of NV detection**. The switching time of the current on and off must allow for NV pulse sequences, thus it must be significantly less than the T_1 time of the NV, which is on the order of 1 ms.
    - **Controllable in space**. The magnetic field can be moved in spaced and allow one to localize the field around a specific NV.
    - **Withstand current**. The device must carry a current that is strong enough to induce the required magnetic field without overheating.

2. **Measuring a spin-labeled monolayer.** The possibility of studying surfaces with single NVs will allow nanoscale characterization of molecular self-assembled monolayers. As such, I aimed to:

    - Develop a method for creating a SAM on the diamond surface and label the surface with free radical spin labels.
    - Measure the signal from the free radical using a single NV. This would be a proof of concept for sensing molecular monolayers labeled with a spin radical with the NV.

3. **Observing CISS with the NV.** In this work I examine CISS in a noval manner, specifically without introducing a current or a magnetic material. Moreover, the detection method used is sensitive to magnetic noise, which has yet to be probed. Examining the phenomena from a new perspective can shed light on the fundamental physics governing the interaction. As such I aimed to:

- Measure the magnetic fluctuations included by the chiral mono-layer and detected by the NV using relaxometry and dephasing methods.

Together, achieving these goals present an advancement to the field of nanoscale magnetic resonance sensing and open new avenues for future research.

2
NV physics

If I have seen further it is by standing on the shoulders of giants

Isaac Newton
1675

The NV's combined properties make it a practical choice for sensing. In general, a sensor requires interaction with the field that is being sensed along with the ability of the user to interact with the sensor and stability relative to noise external to the field being sensed. The NV interacts with the magnetic and electric fields in the environment, can be read out optically, and is stable for time scales that allow both the interaction and read-out. In addition, it is stable at room temperature, and being an atomic defect, it has a natural nanometer sensing scale. In this work the NV center is used at room temperature for sensing magnetic fields with nanometer spatial resolution. This chapter has three parts: First, I describe the basic physics and literature regarding NV centers that is relevant for this work. In the second part, I discuss basic sensing methods, and lastly details regarding the NV sensing setup are presented.

2.1 Physical Properties

2.1.1 NV properties

The NV is an atomic defect in the diamond lattice, where a substitutional nitrogen atom replaces a carbon atom and there is an adjacent vacancy site[65] (figure 2.2(b)). It can exist in two different charge states[66], negative (NV^-) and neutral (NV^0), the negative state is used for sensing and unless

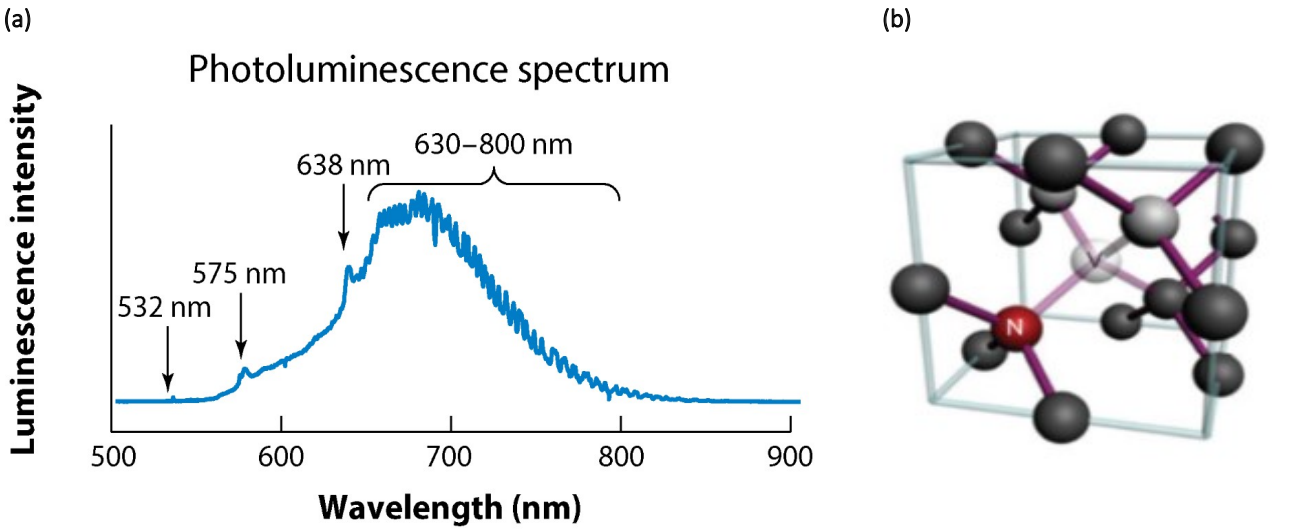

Figure 2.1: NV structure and emission. (a) NV emission spectrum showing the zero phonon line for the two charge states and the broad emission spectra, plot from Schirhagl et al.[13] (b) The diamond lattice with a nitrogen replacing a carbon and an adjacent vacancy (figure from Rondin et al.[65]).

stated otherwise is referred to here as simply NV. The NV^- state consist of six electrons[67], three from the vacancy dangling bonds, two from the nitrogen substitution, and one that is assumed to be sourced from the diamond lattice, possibly a P1 center (nitrogen substitution). The two charge states also differ in their fluorescence spectra and specifically in the zero-phonon-line[68], which is $\lambda = 637$ nm for (NV^-) and $\lambda = 575$ nm for (NV^0), see Fig 2.1(a). Although the defect exists in nature, for sensing purposes it is preferable to fabricate the diamond to control for purity and defect concentration. In a common route[69], the diamond is fabricated by chemical vapor deposition (CVD), and a controlled implantation of nitrogen ions creates defects in the diamond. This is followed by high-temperature annealing (ranging from 600°C to 1200°C), which allows the mobility of the vacancies; if they are adjacent to a nitrogen, an NV center can be created. The implantation energy dictates the depth of the centers in a statistical manner which can be calculated using stopping and range of ions (SRIM). The density of implantation is controlled to create either single NVs, which can individually be addressed optically, or an ensemble of NVs where many NVs are addressed optically simultaneously.

2.1.2 The NV Hamiltonian

The defect energy diagram (Fig 2.2 consists of a ground and excited electronic states that are isolated from the diamond lattice energy states and each consists of a spin triplet state. Within each triplet, there is a spin $|0\rangle$ state and two degenerate spin $|\pm 1\rangle$ states that are separated in the presence of a magnetic field via Zeeman splitting. The Hamiltonian[65,70] describing the NV magnetic interactions is

$$\mathrm{H} = DS_z^2 + \gamma_e B_0 S_z + \gamma_e (B_x S_x + B_y S_y) + \sum_{ij} A_{ij} S_i I_j \tag{2.1}$$

where $D = 2.87$ GHz is the zero field splitting, $S_i = \hbar\sigma_i$ are the spin operators where σ_i are the Pauli matrices, $\gamma_e \approx 2\pi \cdot 2.8$ MHz·G^{-1} is the gyromagnetic ratio and A_{ij} is the hyperfine coupling

to an external spin I_j. Additional terms describing electric field interaction, strain and temperature are not included here[71]. For the case when $B_{x,y} \ll D \pm B_z$ the NV eigenstate is parallel to the NV

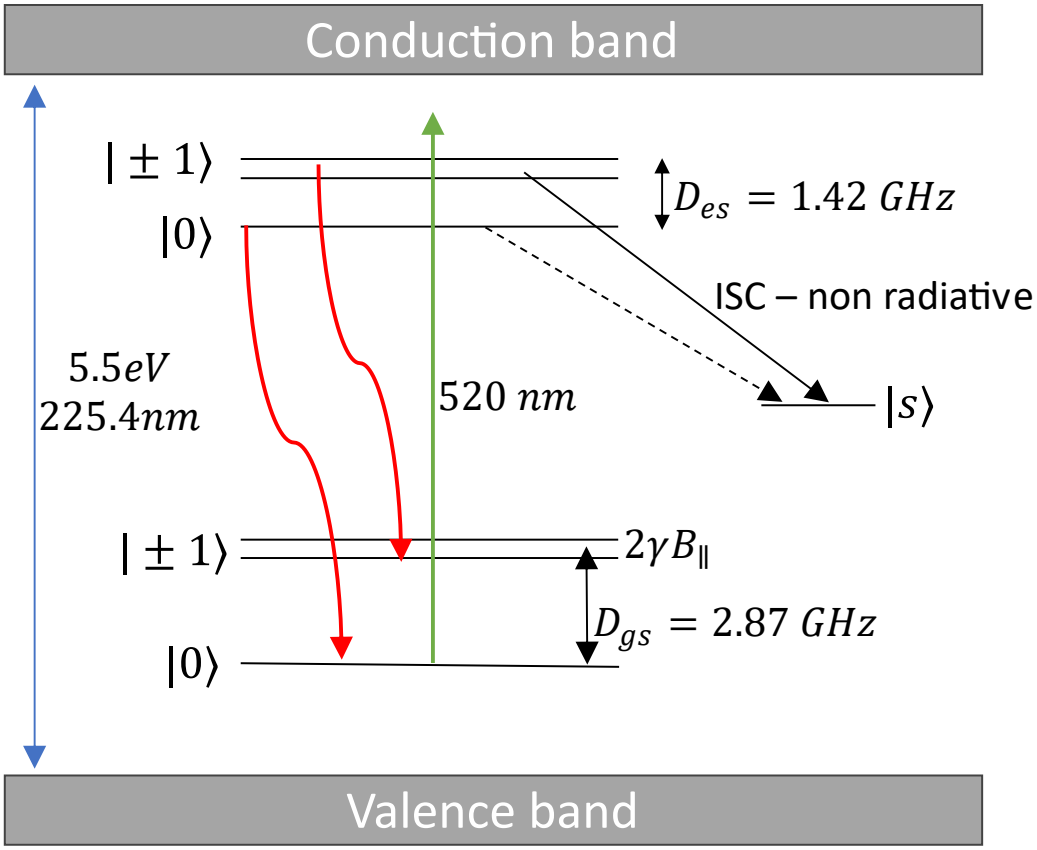

Figure 2.2: NV Energy levels. Energy diagram of the N-V center within the diamond lattice. The N-V states are isolated from the valence and conduction band. The degeneracy in the spin $|\pm 1\rangle$ state is lifted when a magnetic field is applied. Off-resonance excitation at 520 nm excites the system, which then decays in two paths - radiative spin conserving decay (red arrow) and non-radiative non spin conserving to the singlet state (black arrows). The excited state's spin $|\pm 1\rangle$ are partially coupled to the singlet state while the spin $|0\rangle$ state is weakly coupled.

axis defined as"z" and the states will be $\psi = |0, \pm 1\rangle_z$. The $|0\rangle$ to $|1\rangle$ transition acts like an effective two-level system that can be manipulated by microwave (MW) pulses. The qubit can be described using Bloch sphere notation where the two poles are the $|0\rangle$ and $|\pm 1\rangle$ states, see Fig. 2.3. Rabi[28] oscillations (Eq. 2.2) are observed when applying MW at the resonance frequency $\omega_0 = D \pm \gamma B_{\|}$ of the transition between the $|0\rangle$ and $|\pm 1\rangle$ states. The Rabi transition probability for an applied MW field $\mathbf{B}_{mw} = B_1 \cos(\omega t)$

$$P_{\text{Rabi}} = \frac{\omega_1^2}{\Omega^2} \sin^2(\frac{\Omega}{2} t) \tag{2.2}$$

where $\omega_1 = \gamma B_1$ is the amplitude of the applied MW and $\Omega = \sqrt{\Delta\omega^2 + \omega_1^2}$ where $\Delta\omega = \omega - \omega_0$ is the difference between the applied frequency to the resonance frequency.

2.1.3 Qubit Relaxation

The NV is characterized by two types of relaxation[15] - longitudinal T_1 relaxation and transverse T_2 dephasing. When depicting the spin state on the Bloch sphere, T_1 describes shortening of the projection on the z axis and is typically on the order of 1 ms (at room temperature). In the world of

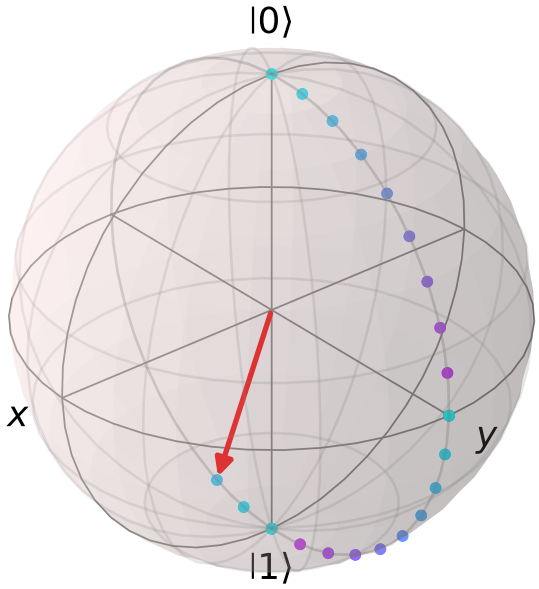

Figure 2.3: Bloch sphere view of Rabi driving showing the NV state as a red arrow rotated from the $|0\rangle$ state to the $|1\rangle$ state and returning to $|0\rangle$ as a function of the time the pulse is applied.

NMR, where there is a macroscopic spin bath, this rate describes the return to the thermal equilibrium of the bath due to "spin-lattice-relaxation". A similar thermal equilibrium exists for single NVs and particularly due to ergodicity; sampling a single NV many times is statistically similar to probing many spins all at once. The dephasing time, T_2 describes the loss of coherence in the x-y plane in the bloch sphere, the typical time scale is $1-10$ µs and this can be extended using dynamical decoupling pulse sequences[72,73]. Each NV is characterized by its local environment, particularly defect centers such as ^{13}C and P_1 centers (nitrogen substitution lattice sites). This dictates the coherence time of the specific NV center.

2.1.4 Optical contrast

The ground and excited orbital states can be optically probed via photon excitation and emission[67]. When illuminated with off-resonance green laser light, the system is excited from the ground level in a spin-conserving manner. The system can then decay either via fluorescence in the red spectrum to the ground state or in a non-fluorescent manner via an inter-system crossing (ISC) to a singlet state, see Fig 2.2. The non-radiative decay to the singlet state is more probable for the $|\pm1\rangle$ state compared to the $|0\rangle$ state due to the difference in coupling between the triplet to singlet states[74,32,75]. This results in less fluorescence of the $|\pm1\rangle$ state compared to the $|0\rangle$ state which allows one to differentiate between the two states via optical detection of this fluorescence[12]. An example of the time trace detected from the two states is shown in Fig. 2.4.

The contrast between the two states is at the core of the read-out of the NV spin state. The natural basis for spin contrast, $|j^0\rangle$ is defined by the lattice and is along the N-V axis, this direction is denoted as "z". DC magnetic fields that are parallel to this axis split the $|+1\rangle$ and $|-1\rangle$ states in the "z" basis, as defined by the zero-field splitting D_0. Yet, perpendicular magnetic fields cause state

mixing, and if they are strong enough, will cause a decrease in the read-out contrast[32]. Following Tetienne et al., a seven-level system can be used to calculate the contrast as a function of the magnetic field $C(\mathbf{B})$ from Eq. 2.3

$$C(\mathbf{B}) = \frac{R(0) - R(1)}{R(0)} \tag{2.3}$$

where $R(0)$, $R(1)$ is the photoluminescence rate from the $|0\rangle$,$|1\rangle$ state respectively. These rates can be calculated in the mixed bases according to Eq. 2.4

$$R(\mathbf{B}) = \eta \sum_{i=4}^{6} \sum_{j=1}^{3} \bar{n}_i k_{ij} \tag{2.4}$$

where η is the collection efficiency, $\bar{n}_i$ is the steady state population and k_{ij} is the transition rate from state $|i\rangle$ to $|j\rangle$. The transition rates for the natural basis, k^0_{pq}, were found experimentally yet under a perpendicular magnetic field the eigenstates are mixed and the rates are calculated according to the new eigenstates, Eq. 2.5

$$|i\rangle = \sum_{j=1}^{7} \alpha_{ij}(\mathbf{B}) \, |j^0\rangle \tag{2.5}$$

where $|i\rangle$ are the mixed states due to the field $\mathbf{B}$ and $\alpha_{ij}(\mathbf{B})$ are the coefficients relating the natural states $|j^0\rangle$ to the mixed state and can be calculated by diagonalizing the Hamiltonian including the

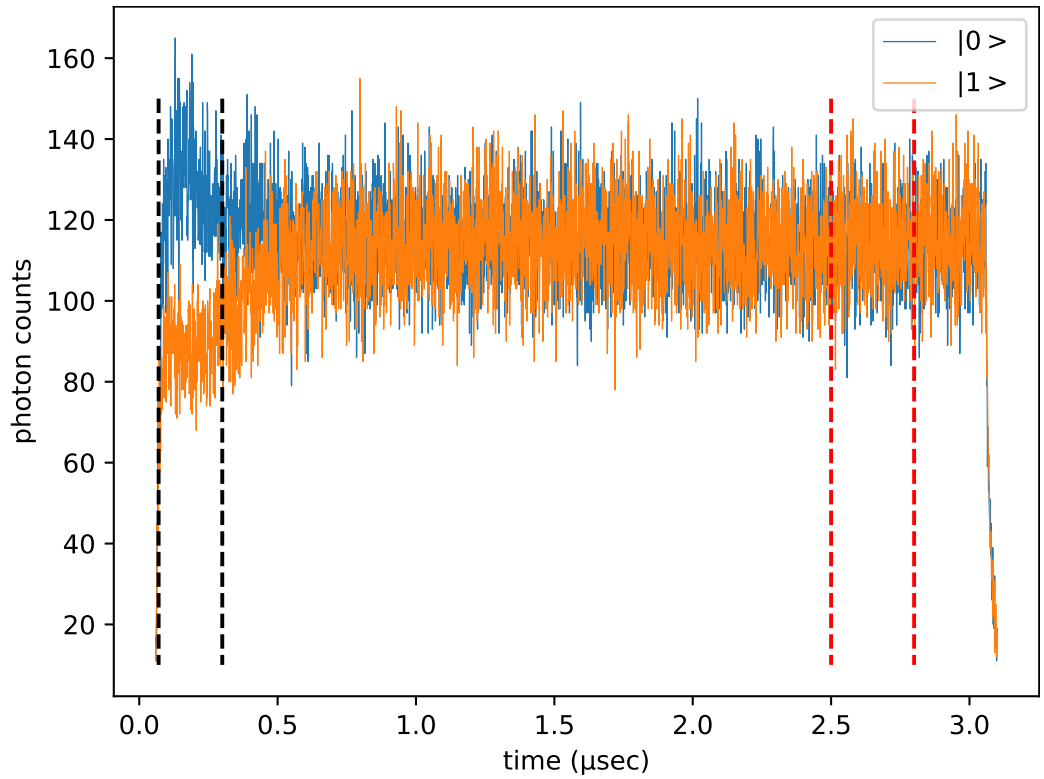

Figure 2.4: The time trace of the fluorescence of the two states $|0\rangle$ and $|\pm1\rangle$. Photons are accumulated over many repetitions and combined to form the time trace. The black dashed lines mark the measurement window and the red dashed lines mark the reference window. In this example the pulse sequence was repeated roughly $8 \cdot 10^5$ times and the data was collected for roughly 5 minutes.

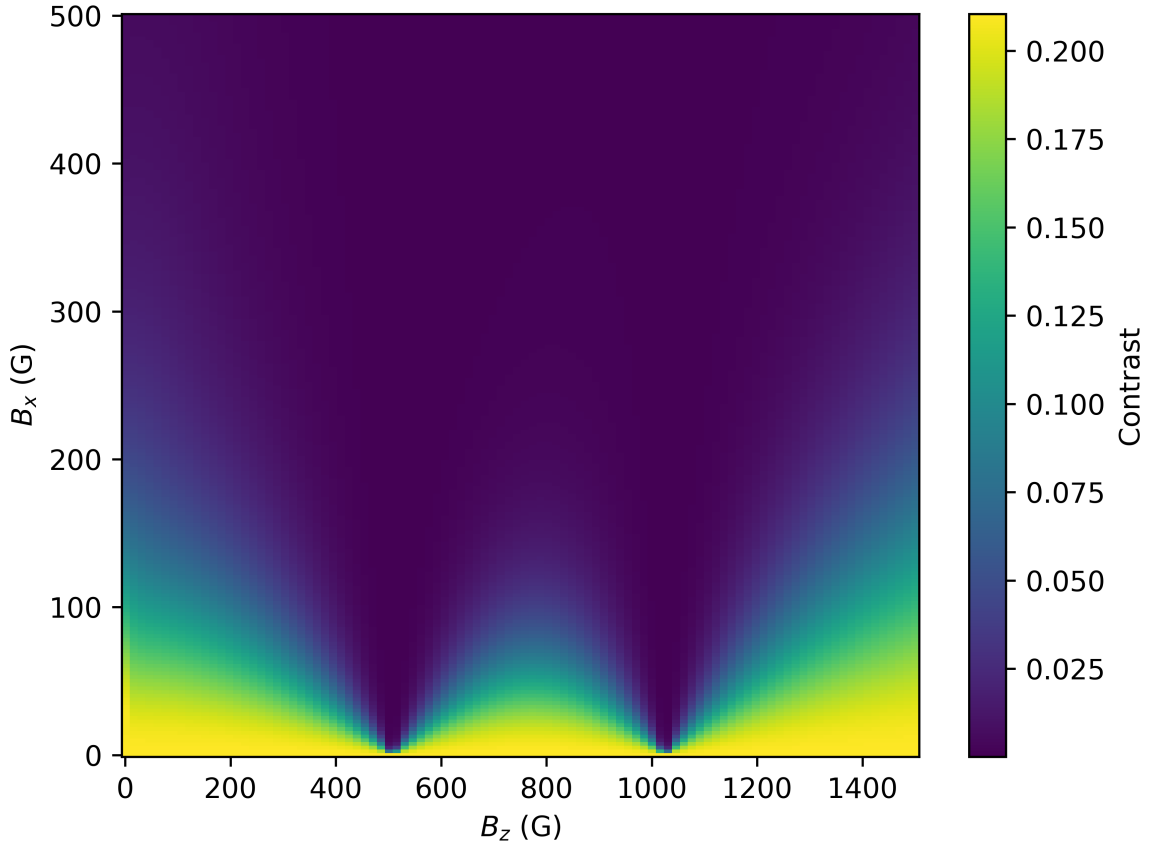

Figure 2.5: NV contrast for vector magnetic field. NV contrast calculated as a function of the magnetic field strength perpendicular (B_x) and parallel (B_z) to the NV. The bright regions have good contrast for sensing while the dark regions have low contrast deeming it less useful for sensing magnetic fields.

off-axis terms B_xS_x and B_yS_y. The new transition rates are then Eq. 2.6

$$k_{ij}(\mathbf{B}) = \sum_{p=1}^{7}\sum_{q=1}^{7} |\alpha_{ip}|^2 |\alpha_{jq}|^2 k^0_{pq} \tag{2.6}$$

The population in each state, n_i that appears in the rate equation is calculated by solving the steady-state rate equation

$$0 = \frac{dn_i}{dt} = \sum_{j=1}^{7} (k_{ji}n_j - k_{ij}n_i) \tag{2.7}$$

Using these equations, the NV contrast as a function of magnetic field is calculated and presented in Fig.,2.5. The results show that magnetic fields applied perpendicular to the NV axis significantly reduce the photoluminescence contrast. This sensitivity to off-axis fields is exploited to align the magnetic field with the NV axis. A permanent magnet is mounted on a movable stage and scanned across the area above the NV center. By recording the photoluminescence at each position, the point of maximum emission is identified. This corresponds to the optimal alignment, where the magnetic field is parallel to the NV axis and transverse components are minimized.

2.1.5 SINGLE EMITTER

The NV center is an atomic defect and if isolated such that an individual center is addressed optically it acts like a single photon source and can be characterized by the correlation function $g^{(2)}(t)$[76,77]. The correlation function is given by

$$\begin{aligned} g^{(2)}(t) &= \frac{\langle I(t+\tau)I(t)\rangle}{\langle I(t)\rangle^2} \\ &= \frac{P_2(\tau|0)}{P_1(0)} \end{aligned} \tag{2.8}$$

where $P_2(\tau|0)$ is the conditional probability to detect a photon at time $t = \tau$ given a photon at time $t = 0$ and $P_1(0)$ is the single-photon detection rate used for normalization. The $g^{(2)}(t)$ function is used to characterize a light source. For classical light $g^{(2)}(t) \geq 1$ since the photon arrival time is uncorrelated, yet for single emitters, antibunching is observed and $g^{(2)}(t) \leq 1$ since the observation of a photon at time $t = \tau$ is correlated to the previous time. The correlation at zero delay[76], $\tau = 0$ is related to the number of emitters n and follows

$$g^{(2)}(\tau = 0) = 1 - \frac{1}{n} \tag{2.9}$$

Thus, for a single emitter we expect $g^{(2)}(0) = 0$. In practice, it does not fall to zero due to noise which allows a second photon to arrive that is not from the emitter. A value of $g^{(2)}(0) < 0.5$ indicates a single emitter, while a higher value indicates the possibility of two or more emitters, according to the specific value measured. The bunching effect describes $g^{(2)}(t) > 1$ at non-zero delay times and is evident in correlation measurements. This indicates a shelving effect[78] and depends on laser power, where a minimal three-level system is used to describe the rate equations, and the decay has two pathways, one direct to the ground state and the other via an intermediate metastable state. In the NV system the direct path is the spin conserving decay from the excited spin triplet to the ground state triplet and the shelved state is the singlet state where an ISC crossing is involved. The correlation can then be fit to the function

$$g^{(2)}(t) = 1 - \beta \exp(-\gamma_1 t) + (\beta - 1)\exp(-\gamma_2 t) \tag{2.10}$$

Where γ_1 and γ_2 are related to the transition rates, the full relation is shown by Berthel et al[78]. An example of the correlation measurement is shown in Fig. 2.6.

2.2 SENSING SCHEMES

A general sensing scheme has three parts - initialization, spin manipulation, and readout. First, a well-defined spin state is achieved; this is followed by an interaction phase with the environment and is accompanied by MW pulses to the sample and the NV that modify the interaction. Finally, the spin state is read out. Different pulse sequences are used to sense different fields according to the frequency and bandwidth that is being sensed.

Initialization is achieved by cycling the spin state between the orbital ground and the excited state by optical pumping[79]. Here, this is achieved by continuous illumination with a 520 nm green laser. This excites the system from the ground to the excited state in a spin-conserving manner. Decay from the $|0\rangle$ excited state will return to the $|0\rangle$ ground state with high fidelity, yet decay from the $|\pm 1\rangle$ state may undergo an intersystem crossing (ISC) to the singlet side-band which is coupled to the ground $|0\rangle$ state. In this way, continuous cycling between the ground and excited states will statistically initialize the system to the ground state with spin $|0\rangle$. There are generally three decay pathways: induced fluorescence, spontaneous fluorescence, and spontaneous non-radiative decay by ISC. Initialization in this method can also be achieved with a pulsed green laser[80] by repeating short laser excitations on the order of 5 ns each. Using the pulsed laser reduces the induced fluorescence and leaves only two pathways for decay, raising the probability of the ISC and so increasing the rate of initialization and reducing the total laser power used. Using the standard polarization process with CW laser, the NV is initialized with roughly 90% fidelity[74,81].

The readout process is the stage where the spin state of the NV qubit is determined after the interaction with the environment. The simplest way to implement this leverages the ISC, as described above, and results in spin-dependent photoluminescence where statistically the $|0\rangle$ state emits more photons than the $|1\rangle$ state (Fig. 2.4). During the readout stage, the system is illuminated

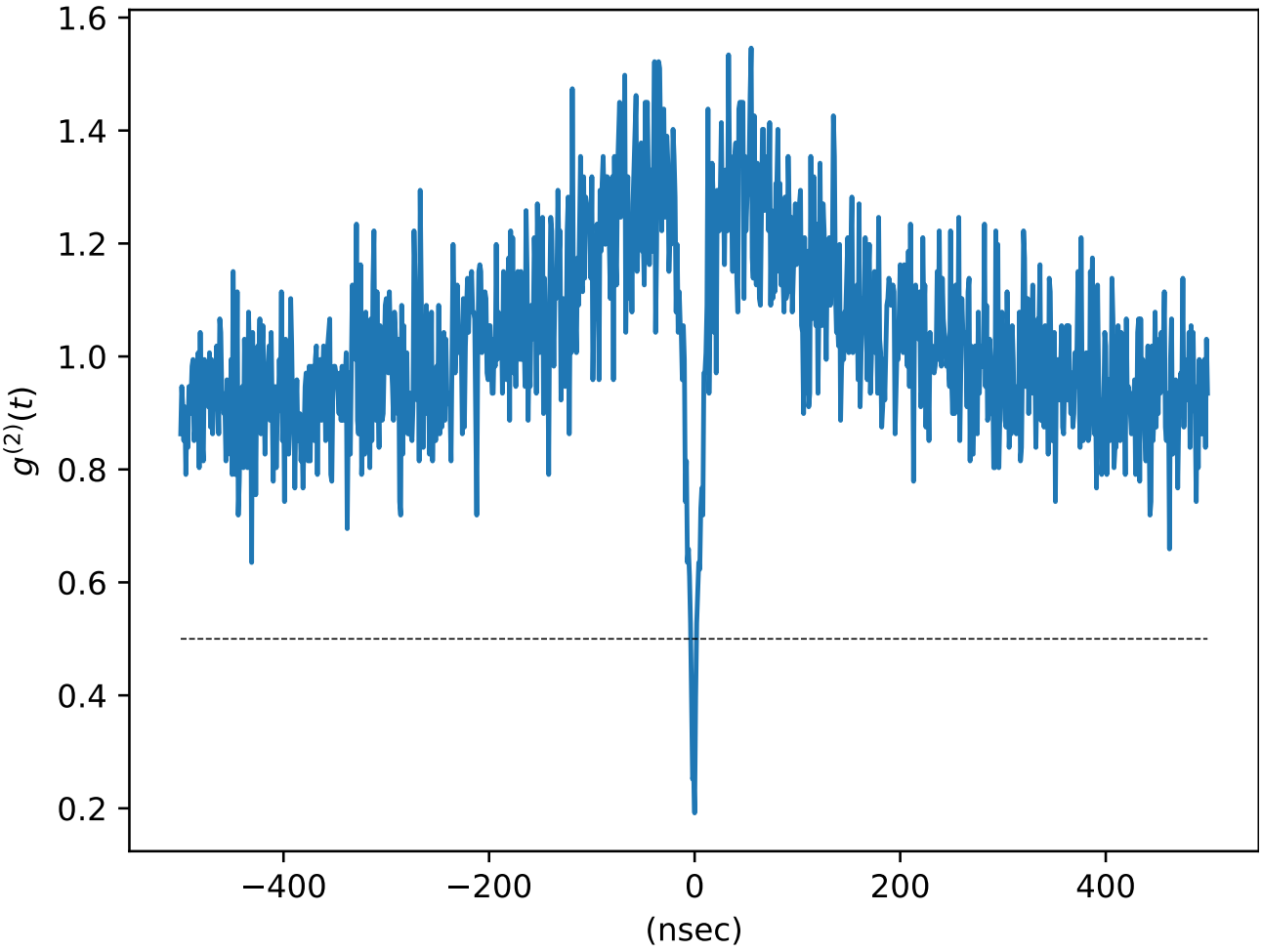

Figure 2.6: Correlation measurement demonstrating a single NV, the correlation at time $t = 0$ falls below 0.5 demonstrating anti-bunching, while the correlation at later time shows a bunching effect where $g^{(2)}(t)$ is greater than 1.

with continuous off-resonance 520 nm green laser and the fluorescence is collected and accumulated to create a histogram of the counts that arrived per time bin during the read-out. The final signal is the mean number of counts collected within a defined window (see Fig. 2.4), it is often normalized relative to the steady-state photon counts as in Eq. 2.11. The error bars for the signal are calculated from the photon counts from the NV time trace collected during the read-out and is shown in Eq. 2.12.

$$S = \frac{\sum t_i/N}{\sum r_i/M} \tag{2.11}$$

where t_i and r_i are the photon counts at time i and N and M are the total number of bins in the signal and reference, respectively. The error for the signal is the propagated error

$$\sigma = \frac{\sum_i t_i/N}{\sum_i r_i/M}\sqrt{\frac{1}{\sum_i t_i} + \frac{1}{\sum_i r_i}} \tag{2.12}$$

This method is not a single shot readout[82,28], and so the full pulse sequence must be repeated many times since in each repetition few photons are emitted, and this is not enough to determine the NV state. Other read-out methods exist, for instance, excited state read-out[83], resonance read-out, and spin-to-charge conversion[84]. These require advanced pulse sequences and additional laser illumination at different wavelengths. At times these are advantageous if single-shot readout is required.

2.2.1 Spin manipulation phase

During the spin manipulation stage the NV interacts with the environment and MW pulses are applied to control this interaction. The interaction of the NV with magnetic fields in the environment is seen in the Hamiltonian in Eq. 2.1. The NV is sensitive to magnetic fields in three main frequency ranges - DC, MHz and GHz, where the precise range depends on the pulse sequence applied. Sensing DC magnetic fields can be achieved using a Ramsey or ODMR pulse sequence, see below. Both are sensitive to the magnetic fields parallel to the NV axis and detect the change in the qubit Larmor frequency. Coherent AC magnetic fields can be detected in the range of a few MHz, depending on the coherence time of the NV. Advanced pulse sequences have shown sub-Hz resolution[85,86], while methods that are simpler to implement can achieve kHz resolution[29,30]. The NMR signal from spins that precess under the influence of a magnetic field have a coherent AC signal and as such these sensing schemes are practical for detecting the NMR signal such as carbon in the diamond or hydrogen external to the diamond[87,88,89]. In addition, noise spectroscopy can be used to detect fluctuating magnetic fields. In this case, the decay rate of the NV is measured as it is sensitive to noise in the environment and both the decay time and the power law indicate the physics of the environment[90].

DC sensing schemes

A Ramsey (known as free inducting decay, FID, in the NMR community) pulse sequence is shown in Fig. 2.7(c). After initialization to the state $|\psi\rangle = |0\rangle$ the qubit is rotated to the equator $|\psi\rangle = \frac{1}{2}(|0\rangle + |1\rangle)$ using a $\frac{\pi}{2}$-pulse. The state then evolves freely under the influence of the external field that is perpendicular to the x-y plane. Finally, a second $\frac{\pi}{2}$-pulse projects the spin back to the z-axis for read-out (expanded details in Appendix A.1). In this manner, the qubit accumulates a phase that is proportional to the detuning between the external field to the frequency of the applied $\frac{\pi}{2}$-pulse and DC shifts in the magnetic field parallel to the z-axis are measured. The decay time in the measurement is known as T_2^*; it is due to low-frequency noise and related to inhomogeneities in the magnetic field[15].

In ODMR (alternatively known as electron spin resonance or ESR), Fig. 2.7(b), the DC magnetic field that is parallel to the NV axis, $B_\parallel$ is detected. After initialization, a π-pulse is applied with varying frequency, $B = B_1 \cos(\omega t)$. If the pulse is on resonance with the qubit transition, $\omega = \omega_0 = D \pm \gamma B_z$ the spin state will flip, $|\psi\rangle = |1\rangle$, according to the Rabi transition probability, Eq. 2.2. The resulting curve is fit to a Lorentzian[91,92], and the resonance frequency is deduced from the central dip. For an MW pulse with low power (equivalent to a long time), the broadening[93] is due to the dephasing time $\Delta f = T_2^*$ and can be extracted from the FWHM (full width at half maximum). When power broadening is significant, the curve is fit to a Gaussian, which accounts for additional noise sources.

Coherent AC sensing

A Hahn echo pulse sequence can be used to detect AC signals[94] and extend the coherence time to T_2, an order of magnitude longer than T_2^*. In this sequence, shown in Fig. 2.8, the spin is initialized to the $|\psi\rangle = \frac{1}{2}(|0\rangle + |1\rangle)$ state and after half the evolution time, $\frac{\tau}{2}$, an additional π-pulse is applied, followed by a second evolution time $\frac{\tau}{2}$. In this manner, low-frequency noise is canceled in the second half of the evolution, and only fast oscillations influence the qubit and are detected. More advanced pulses[95,96,29], such as XY-8-n shown in Fig. 2.8, can be used to achieve better noise cancellation and result in a narrow bandwidth filter that is used to sense a specific desired AC signal. A coherent AC signal is detected as a dip in the echo signal when the evolution time matches the inverse of the frequency[88], $\tau = \frac{2\pi(2k-1)}{2\omega_{L,i}+A}$, where τ is the inter-pulse time as shown in Fig. 2.8, k is the order of the resonance, $\omega_{L,i}$ is the Larmor frequency of the detected (nuclear) spin and A is the parallel component of the hyperfine interaction.

Detecting an electron signal

Electron spins are commonly detected with two pulse sequences where additional pulses are applied to the detected electron. The first is known as a double-electron-electron-resonance (DEER) sequence, where a Hahn-echo sequence is applied to the NV, and an additional π_e-pulse is applied to the external electron spin. The frequency of the π_e-pulse applied to the auxiliary electron spin is swept and when on-resonance with the auxiliary spin, it will be flipped. This will change the

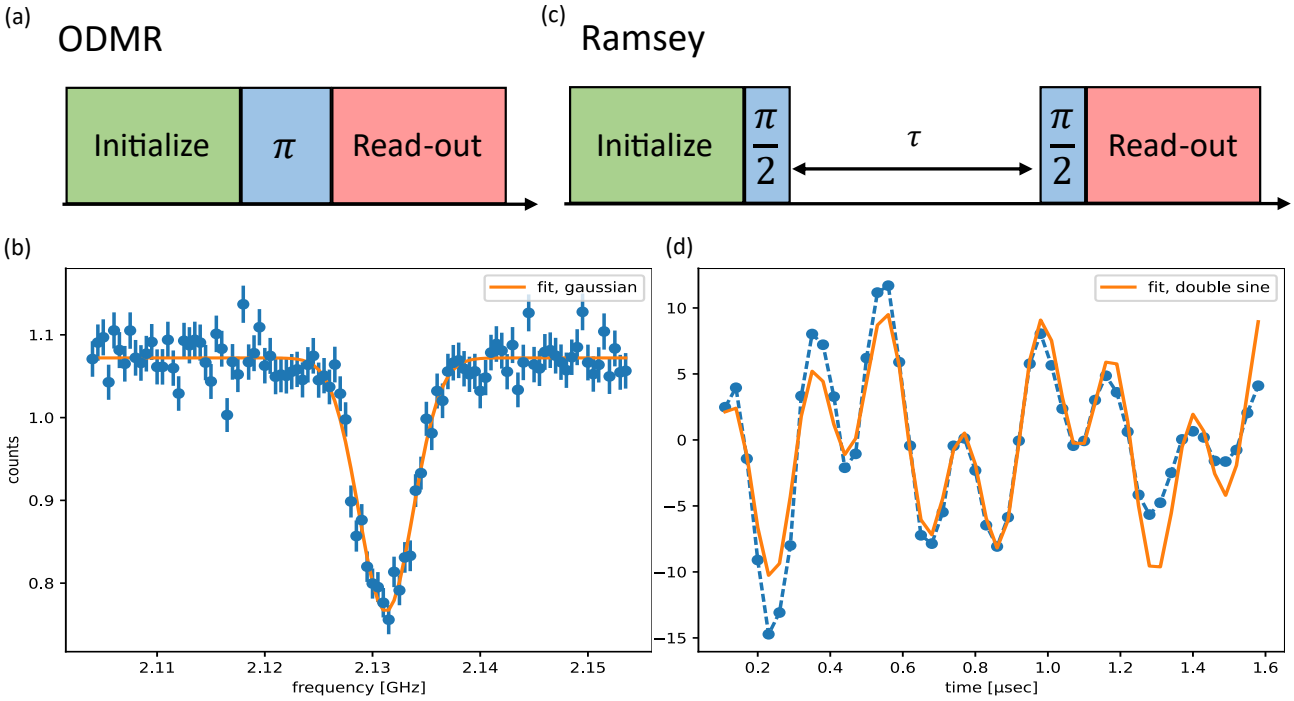

Figure 2.7: Pulse sequences for DC sensing. (a) ODMR pulse sequence where a MW pulse is applied and the frequency of the pulse is scanned. If the pulse is on resonance with the transition the state is flipped. (b) An example of a ODMR measurement fit to a Gaussian $f = A\exp(-\frac{(x-f_0)^2}{\sigma^2})$, where $f_0 = 2.13\,\text{GHz}$, equivalent to a magnetic field of $B_{||} = 286(G)$ parallel to the NV axis. (c) Ramsey pulse sequence, the spin state evolves on the equator and acquires a phase proportional to the magnetic field. (d) An example of a Ramsey measurement, the data is fit to a double sine (see Appendix A.1), where the two frequencies fit are $f_1 = 1.8\,\text{MHz}$ and $f_2 = 4.77\,\text{MHz}$. Note that the Ramsey and ODMR measurements that are shown here are done at different magnetic fields.

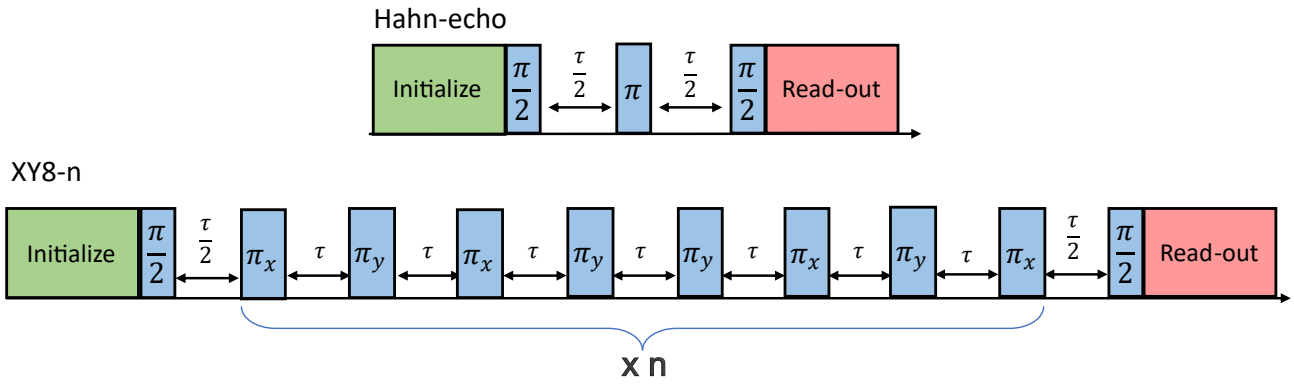

Figure 2.8: (top) A Hahn-echo pulse sequence where a π-pulse is applied after half the interaction time $\tau/2$ and refocuses the spin. (bottom) Dynamical decoupling pulse sequence, XY-8-n, where a sequence of alternating π-pulses is used to detect a specific signal.

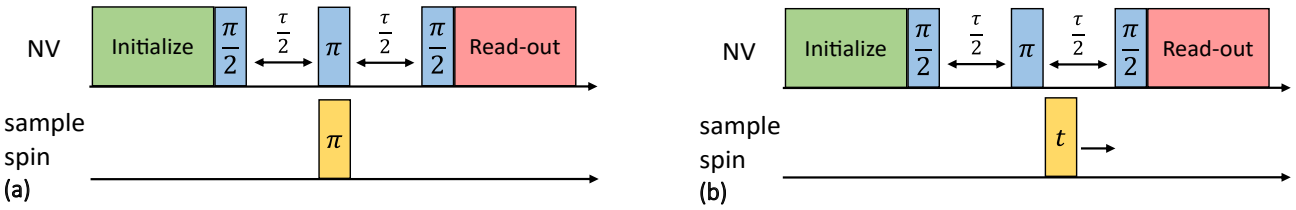

Figure 2.9: Pulse sequence used to probe electron spins by the diamond. (a) DEER sequence where a "Hahn-echo" is applied to the NV and a π-pulse is applied to the sample electron spin with varying frequency. (b) DEER-τ sequence where a "Hahn-echo" is applied to the NV spin and a resonance MW pulse is applied to the sample electron spin with varying length.

phase accumulated by the NV and is detected as a drop in the NV contrast[34], Fig. 2.9(a). This can be thought of as a detection of the electron's magnetic field, the Hahn echo sequence cancels the phase from noise due to AC fields, but due to the π_e-pulse the electron field is not canceled since its direction was flipped as well and so the contrast decreases. Here, the coherence time of the free electron must be longer than the NV coherence time, T_2, or the NV will not have time to accumulate phase from the electron interaction. The π_e-time used for the electron is assumed to be equal to the π_{NV}-time of the NV electron. A "DEER-τ" measurement follows the DEER measurement. Here, an MW pulse at varying lengths is applied to the auxiliary spin at the frequency detected in the DEER sequence, Fig. 2.9(b). This is equivalent to Rabi nutations applied to the electron spin. For this, the relaxation time, T_1 of the electron spin must be longer than the NV interaction time.

Electron spin sensing differs from nuclear spin sensing in its frequency range, which in turn dictates the pulse sequences used to study them. Additionally, the information one can obtain from the electron spins differs from nuclear spins, as demonstrated in the vast literature on electron paramagnetic resonance[97] (EPR) research. The electron interaction with the NV is determined by the dipole-dipole interaction[34,35]

$$\mathcal{H} = -\sum_i \frac{\mu_0 \gamma_{e,i} \gamma_{NV} \hbar^2}{4\pi |r|^3} (3(S_{NV} \cdot \hat{r})(S_{e,i} \cdot \hat{r}) - S_{NV} \cdot S_{e,i}) \tag{2.13}$$

where $\gamma_{e,i}$ (γ_{NV}) is the gyromagnetic ratio for the i-th electron (NV), $S_{i(NV)}$ is the spin of the i-th electron (NV) and r is the vector connecting the sample electron to the NV. For a field aligned with the NV, this term can be written as

$$\mathcal{H} = -\sum_i \frac{\mu_0 \gamma_{e,i} \gamma_{NV} \hbar^2}{4\pi |r|^3} (3\cos^2 \theta_{i-NV} - 1) \tag{2.14}$$

For a single electron, the signal will appear as oscillations at the interaction frequency[34,98,36]. Yet, in the more general case where there are many interacting electrons, the oscillations will sum to an exponential decay. In the midrange case where there is a single electron dominating the interaction, this oscillation may be apparent above the general decay[34].

Noise spectroscopy

Measuring noise spectroscopy gives insight to the random magnetic fluctuations in the NV environment[28]. This is in contrast to coherent detection where a known frequency is probed. The NV is sensitive to magnetic fluctuations in three main frequency ranges - kHz, MHz and GHz, where the response depends on the filter function dictated by the pulse sequence. The phase accumulated by the NV is a convolution between the filter function of the applied pulse sequence, $Y(\omega)$, and the spectral density of noise, $S(\omega)$, as described in Eq. 2.15 [28,77]:

$$\chi(t) = \frac{2}{\pi}\int_0^\infty \gamma^2 S(\omega)|Y(\omega)|^2 d\omega \tag{2.15}$$

In T_2 dephasing spectroscopy, the coherence of the spin state is probed[28], where $|\pm\rangle = \frac{1}{2}(|0\rangle \pm |1\rangle)$. This method is sensitive to fields that are parallel to the NV axis. For a T_2 pulse sequence (Fig. 2.10(a), same as Hahn Echo) the filter function is[93,99]

$$Y(\omega) = \frac{1}{t}\left|\frac{\sin^2\frac{\omega t}{4}}{\frac{\omega}{4}}\right|^2 \tag{2.16}$$

where ω is the frequency in question and t is the evolution time. Thus, T_2 sensing can be tuned by setting the time steps t, and limited by the coherence time of the NV. The noise detected is in the MHz range, as shown in Fig. 2.10(b).

In T_1 relaxometry (Fig. 2.10(a)) the qubit is sensitive to frequency components that are on resonance with the level splitting, i.e., the $|0\rangle$ to $|\pm1\rangle$ transition which is defined by the external magnetic field $f = D \pm \gamma B_\parallel$ and is on the order of GHz. For this pulse sequence, the filter function is[93]:

$$Y(\omega) = \frac{1}{\pi}\frac{\Gamma}{\left|\Gamma^2 + (\omega - \omega_L)^2\right|} \tag{2.17}$$

Here $\Gamma = \frac{1}{T_2^*}$ and $\omega_L = 2\pi f = D \pm \gamma B_\parallel$. Here, the center is defined by the Larmor frequency and is generally in the GHz range while the width is defined by $\Gamma = \frac{1}{T_2^*}$, typically on the order of $T_2^* \approx 1\,\mu s$, shown in Fig. 2.10(b). Several studies have demonstrated these sensing techniques to gain insight at different systems such as noise from ferritin molecules[93,100], ion concentration in cells using Gd ions[101] and properties of 2D materials[102].

2.3 The NV sensing setup

The experimental setup used for NV sensing is described below. The heart of the setup is the diamond itself. The manipulation is achieved with MW pulses and optical excitation and readout which are all synchronized electronically. The full experiment is controlled with an open source software, *QuDi*[103], which was adapted for this work.

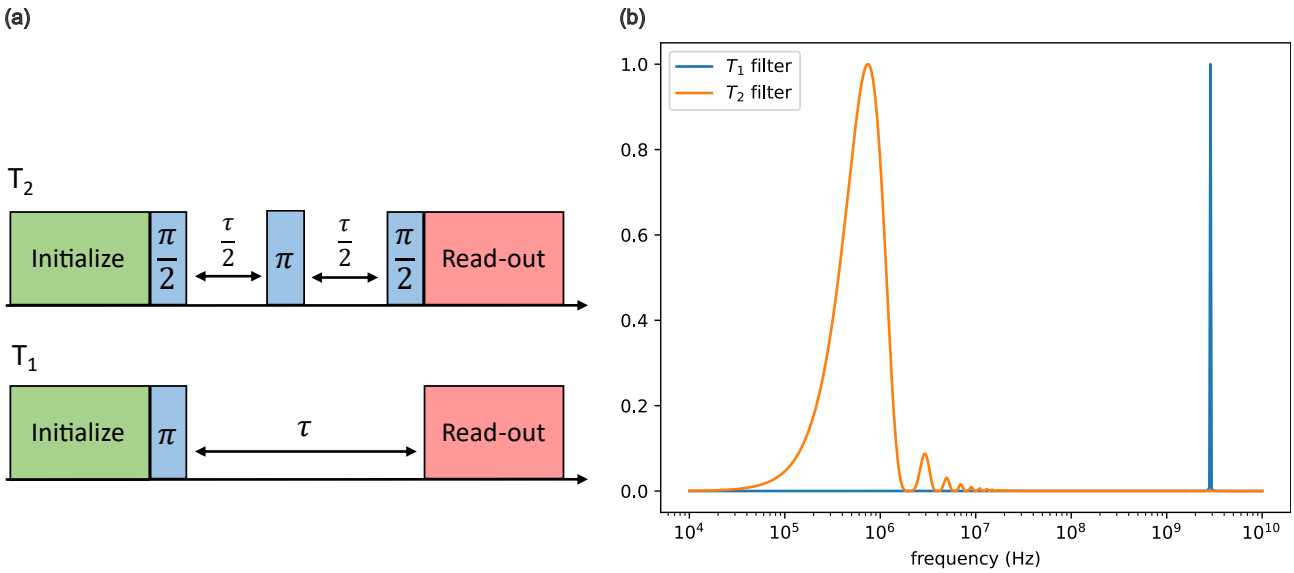

Figure 2.10: (a) Pulse sequences used for noise spectroscopy. (upper) A Hahn echo sequence, or T_2, detects decoherence in the phase. (lower) Relaxometry, or T_1, the sequence is used to measure magnetic fluctuations in the GHz range. (b) The filter function of the noise spectroscopy for the T_1 and T_2 pulse sequences as shown in Eq. 2.17 and Eq. 2.16. Each function is characterized by its center and width, as seen in the figure.

2.3.1 Diamond preparation

Several diamonds are used in this work, all are designed for single NV sensing. As such, the nitrogen implantation is such that the density allows for optically addressing single NVs and the implantation energy is either 5 keV or 10 keV, resulting in shallow NVs (less than 10 nm, from SRIM). The diamond is patterned to have pillars for improved optical collection [104]. The pillars have a circular flat region at the top with a diameter of roughly 500 nm - here samples can be placed in the vicinity of the NV. The pillars are set in a grid formulation with markers between the grids. In this way, a specific NV can be identified, and repeated experiments can be done on the same single NV. An SEM image of a typical diamond is shown in Fig. 2.11 showing the dimension of the grid array and of the pillar.

The surface properties of the diamond are of importance to sensing, as they affect charge state stability and noise in the environment. The diamond surface is cleaned to remove organic residues and remove graphitic carbon and improve the coherence time of the NV [44]. The cleaning is done with tri-acid boiling [105] which combines nitric, perchloric and sulfuric acids, where the diamond is placed in the heated solution for several hours.

2.3.2 Microscope stage

The *Attocube CSFM* (see Fig. 2.12) combines confocal and AFM capabilities by incorporating a sample stage along with optical access from below and tuning-fork AFM control above the sample. It includes four stages - sample (xyz), AFM tip (xyz), magnet (xyz), and objective (z). Each stage is controlled by piezoelectric motors, which have a stick-slip motion for coarse motion and have an encoder to read out the location of the stage. In stick-slip motion a saw-tooth voltage is applied to the stage at a frequency up to 1 kHz. The input voltage must be strong enough to move the stage,

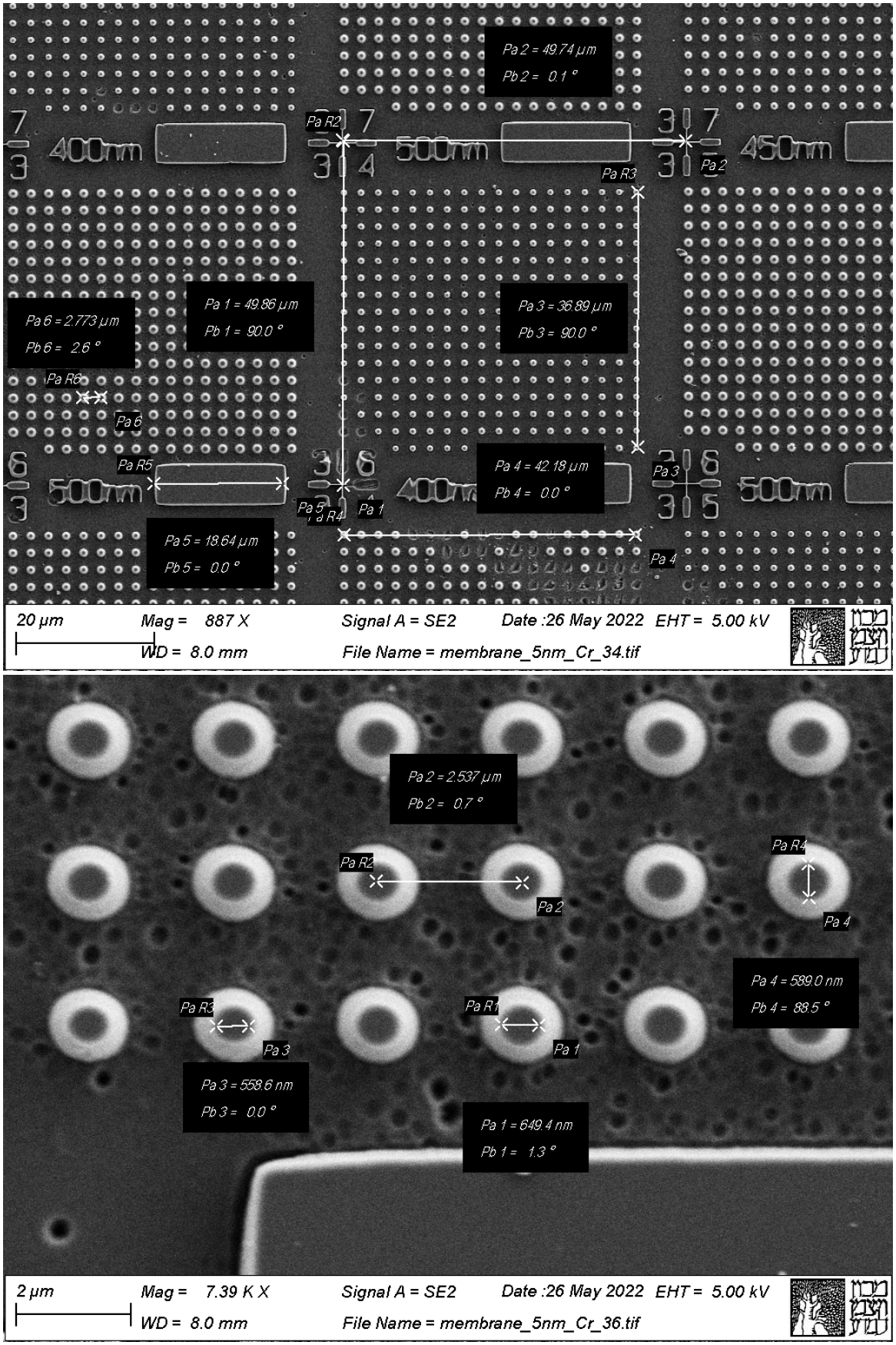

Figure 2.11: SEM image of diamond (top) Large area showing a pillar array and the markers between the arrays. The distance between the markers is measured and is 50 µm. (bottom) High magnification image of pillar array, showing the flat area at the top of each pillar and the diameter of the pillar is 560 nm-650 nm and the distance between pillars is 2.5 µm.

the values applied are between 20 V to 40 V. The range of the scanners along each axis is 15 mm. Fine motion is incorporated only for the AFM tip scanner and it allows the application of a DC voltage which elongates the piezoelectric stage in proportion to the applied voltage. The range enabled is 20 μm in x,y (parallel to the sample plane) and 4 μm in z.

2.3.3 Optical microscope

The NV sensing setup consists of an optical confocal microscope used for imaging the diamond and qubit initialization and readout, see Fig. 2.13. A 520 nm laser is focused to an optical fiber intended to achieve a gaussian beam. The output of the fiber is focused on to an objective which collimates the beam. Two polarizers and a half wave-plate are used to control the polarization and the power of the laser beam where one polarizer is mounted on a motorized stage for electronic control. A 90-10 beam splitter deflects 10% of the beam to a APD which measures the power of the beam, the remaining 90% of the laser beam passes through a dichroic mirror which separates the laser excitation path from the fluorescence emitted from the diamond. A 2D galvanometer scanning mirror is used to scan the beam across the sample. The applied voltage range is -0.45 V to 0.45 V, resulting in a scan range of 164 μm× 164 μm. The voltage is controlled by a DAQ card (National Instruments) which is controlled by the software for confocal scanning. A telescope configuration of two lenses ($f_1 = 75$ mm, $f_2 = 50$ mm) is placed after the galvanometer, and this is followed by an objective lens (Olympus MPLFLN100X air-objective with NA 0.9) that focuses the laser on the sample, with a final power on the order of 0.1 mW. For an ideal telescope[106], the beam should enter the objective at the center, and only the incident angle changes, yet due to space limitations, the telescope is sub-optimal (see Appendix B.1.1). The detection path starts with the red fluorescence emitted from the N-V center, the fluorescence is collected by the objective and follows the optical path to the dichroic mirror where it is deflected to the detection path. A lens ($f = 75$ mm) focuses the beam at the pinhole (75 μm) which acts as a confocal element, a second lens ($f = 75$ mm) collimates the beam. After entering a black box there is a long pass filter (645 nm) preventing residual green light from reaching the APD. Finally, the beam is focused ($f = 25$ mm), split at a 50:50 beam splitter and detected by two APDs.

A CCD camera is incorporated to image the diamond; it cannot be used simultaneously with the confocal microscope as the optical paths conflict. White LEDs are on a PCB which illuminates the sample from above, this light is collected by the objective and a motorized flip mirror deflects this light to the CCD, a lens is placed before the CCD which focuses the light. The resulting image is seen in Fig. B.3; the image shows the diamond membrane, yet it suffers from poor focus, presumably due to chromatic aberration from the white light, which requires a proper lens. The deflection mirror is placed along the confocal path described above, and the two detection methods do not work at the same time.

The electronic control of the system and synchronization is done with an arbitrary waveform generator (AWG). Two analog channels are used for IQ mixing which are fed into an MW generator to achieve the required pulsed MW signal. The IQ mixing allows fast sweeping of the MW signal and is limited by the AWG sampling rate 1.25 GS/sec. The AWG sample rate liimts the band-

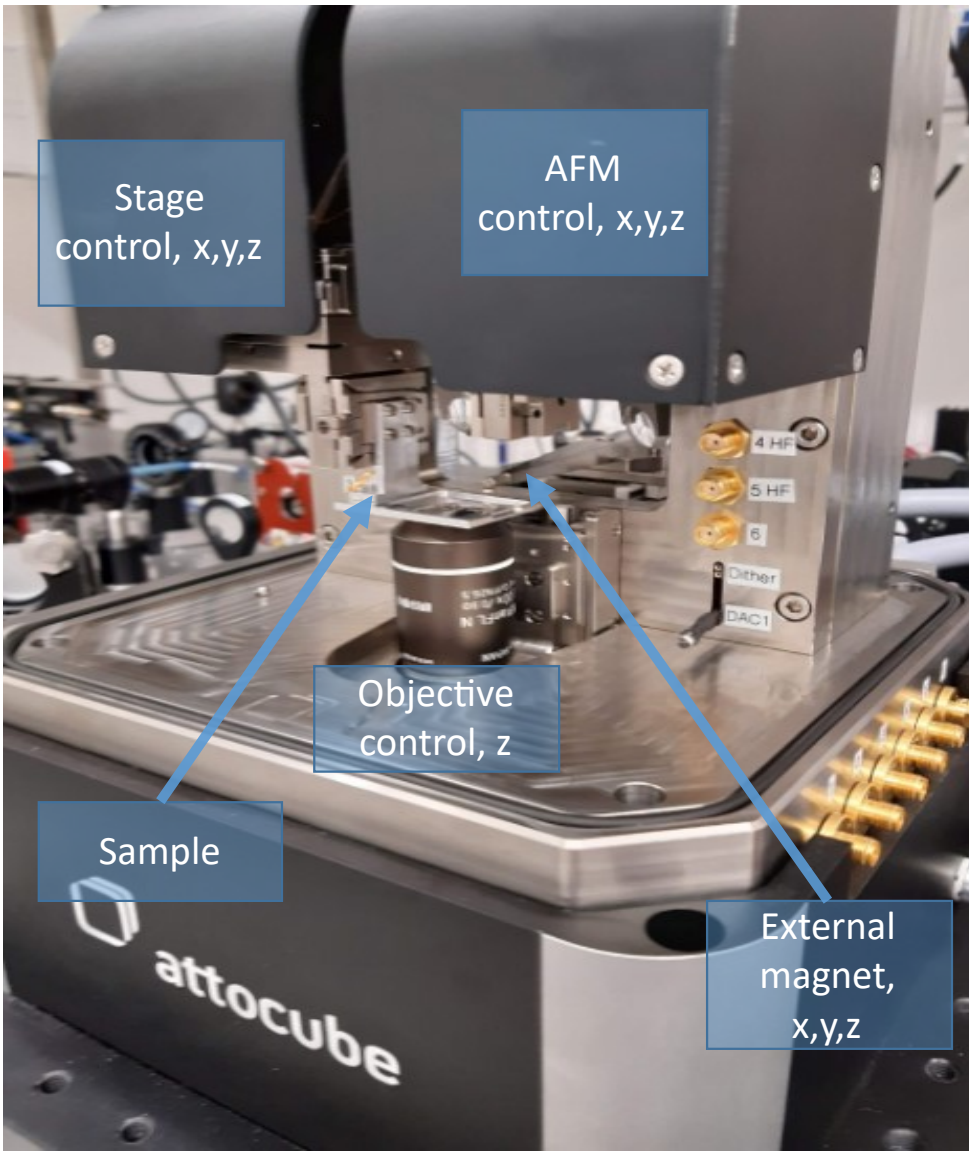

Figure 2.12: Image of the *Attocube CSFM* microscope setup, showing the integration of confocal optical and atomic force microscopy (AFM) capabilities. The system includes independent control of the objective position in the z-direction, AFM tip positioning in x, y, and z, and a sample stage with similar x,y, and z positioning. An external magnet, also mounted on a three-axis stage, allows spatial alignment of the magnetic field with respect to the NV center. This configuration enables precise alignment of all components for combined optical, magnetic, and scanning probe experiments.

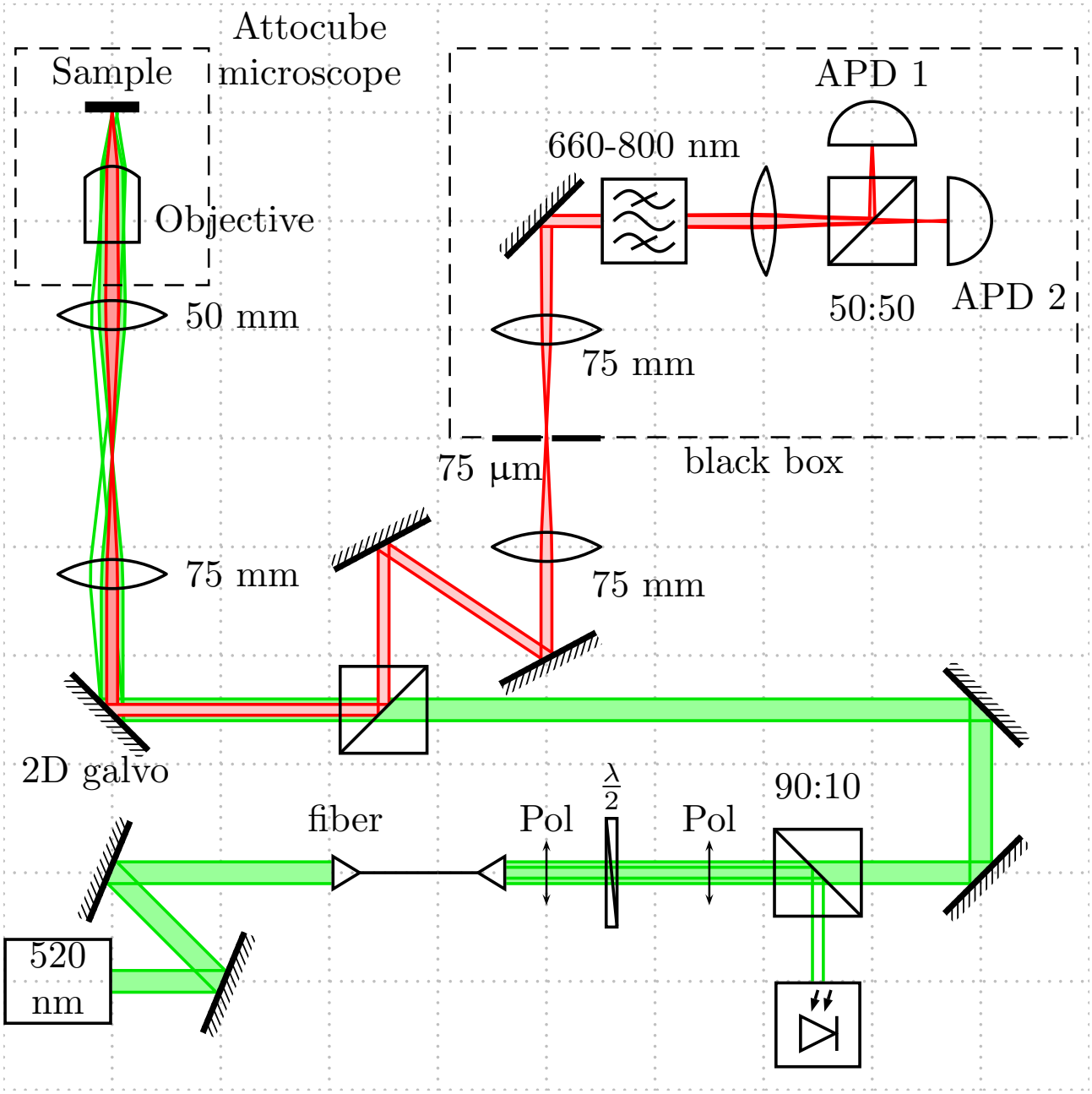

Figure 2.13: Confocal microscope setup includes an excitation path (green) starting at the green laser denoted 520 nm and focused at the sample, and a detection path (red), where red light emitted from the sample is deflected to the APD's at the dichroic mirror, focused at a pinhole for confocal resolution and split with a 50:50 beam splitter to two APD detectors. Full details in the text.

Device type	model	comments
Laser	Swabian Instruments, DLnsec	520 nm, 40 mW
Arbitrary waveform generator	Spectrum Instrumentation DN2.663-04	
Microwave generator	SGT100A	
Amplifier	ZHL-16W-43-S+	range 1.8 to 4 GHz
Amplifier	Elite-RF M.02006G414550	20 MHz - 6 GHz
Time tagger	SI TimeTagger20	fast photon counter
APD	SPCM-ARQH-12	500 dark counts
DAQ card	National Instruments 6363	slow photon counter
Power supply for APD	BiLT BE582	
Linear power supply for galvo	Thorlabs GPS011	
Power supply for amplifier	HMP4040	

Table 2.1: List of electronic components used in the setup

width of the MW modulation to $\Delta f = \pm 625\,\text{MHz} = \frac{1}{2\cdot\Delta t} = \frac{1}{2\cdot 1.25e-9}$, in practice the bandwidth is limited at 400 MHz and depends on the output amplitude as described in the manual. The MW signal is then amplified and inserted into a PCB using a high-frequency coaxial cable. The PCB feeds the signal to a copper co-planar waveguide that is fabricated in-house (see Appendix B.2. The optical signal is collected by two APD's which tranlate the photon detection to an elecric signal which is sent to a time tagger for photon counting. The time tagger is synchronized by the AWG and the data is fed to a PC and processed with the *Qudi* [103] software package. The time tagger records the photon detection with a 1 ns resolution (defined by the user) and accumulates the photon counts in a histogram that describes counts per time bin. The list of electronic components is shown in Table 2.1.

3

CFD development

> It is not your responsibility to finish the work, but neither are you free to desist from it.
>
> *Rabbi Tarfon*
> *Pirkei Avot 2:16*

MRI can be achieved by applying a non-homogeneous magnetic field such that there is a gradient in the resonance frequency over a sample. An implementation of nanoMRI is done here by depositing a wire on a tip to create a current-focusing device (CFD). From Biot-Savart law it is known that a current along a wire induces a magnetic field in the vicinity of the wire. Here, the wire conforms to the geometry of the tip and has a sharp turn at the apex - this change in direction of the current causes a gradient in the magnetic field near the apex of the tip, Fig. 3.1. Ideally, an infinitely strong current would give an infinitely strong gradient, but in practice this is limited by the heating that the device can sustain. Working with a tip controlled by AFM feedback allows the wire to be placed near the diamond surface, increasing the gradient field. The tip geometry is practical for sensing applications where a sample is placed on an array of single NVs. The statistical manner of such samples may require sampling several NVs to find a "good" sample, and using a tip allows one to align the gradient near a desired NV and does not limit the user to a specific location.

Research and development were carried out to design and implement the CFD for use in nanoMRI. The method for preparing a wire along a tip was inspired from the SQUID-on-a-tip[107,108] where a superconducting wire is deposited along such a tip. Here, I follow similar principles for fabrication and adapt the CFD for the room-temperature setup which carries an ohmic current. This

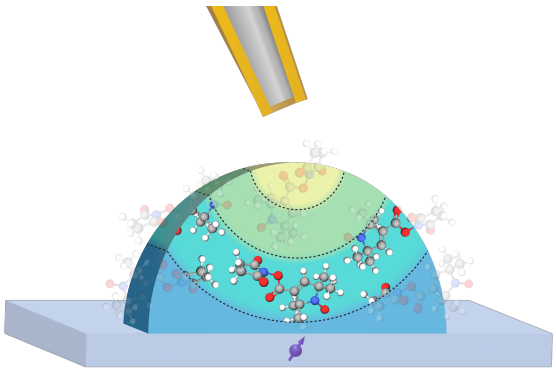

Figure 3.1: Schematic of the CFD applying a local gradient on sample placed on a diamond with an NV sensor.

work progressed through three key stages: simulation, fabrication, and integration into the NV confocal microscope. The following sections provide a detailed description of each stage of the development. The development presented here was published in Communications Physics and was titled "Pulsed magnetic field gradient on a tip for nanoscale imaging of spins."[109].

3.1 Simulating the CFD

The magnetic field of the tip is the most basic requirement of the tip, yet I found that current-induced heating was the limiting factor in tip design, and this dictates the tip geometry.

3.1.1 Simulating the heating of the tip

The Joule heating induced by the current running through the tip was simulated using COMSOL. The heat transfer equations are

$$\begin{aligned} \rho C_p \mathbf{u} \cdot \nabla T + \nabla \cdot \mathbf{q} &= Q + Q_{\text{ted}} \\ \mathbf{q} &= -k \nabla T \end{aligned} \tag{3.1}$$

where ρ is the density, C_p is the heat capacity at constant pressure, $\mathbf{q}$ is the heat flux, Q are additional heat sources, including thermoelastic damping (TED), and $\mathbf{u}$ is the velocity vector of translational motion. The heating is concentrated at the apex due to the narrowing geometry towards the apex of the tip. The geometry chosen to simulate the heating is that of a flat wire with a narrow band at the center, this reflects the heat concentration at the apex. The geometry included a thin layer of Au on top of a base of quartz and surrounded by air to account for the heat transfer accurately. The geometry is shown in Fig. 3.2. We first examine the steady state temperature the device reaches while varying both apex size and the applied current and extract the maximum temperature of the device. I assume that the tip will fail when the metal reaches its melting point, for Au this is 1337 K and so the device heating is compared to Au melting point, see Fig. 3.3. It is noted that the device may fail before this point such as if heating changes the resistance of the wire, the actual current will change and the device will not function correctly. From the simulation, it is shown

that for a 10 mA current, a 100 nm apex is expected to fail, yet an apex of 1 µm can sustain the heating. During the experiment, the current is pulsed and does not reach a steady state; for this reason, I also simulated the temporal change in the temperature for a 15 mA current on a device with a 1 µm apex. Although at steady state such a device is expected to fail (Fig. 3.3a) the temporal simulation shows it will take more than 1 second to reach this temperature (see Fig. 3.3b). During a typical experiment the applied currents are on the order of µs, and thus also higher currents can potentially be applied.

Balancing the need to avoid overheating while achieving a significant gradient for sensing dictated the final dimensions of the device. I chose a cross-section large enough to sustain a current on the order of 10 mA. Following the simulation, the apex was designed to be on the order of 1 µm, and the deposition thickness was set to be 200 nm, resulting in a cross-section that is large enough to sustain a current without damaging the device due to heating.

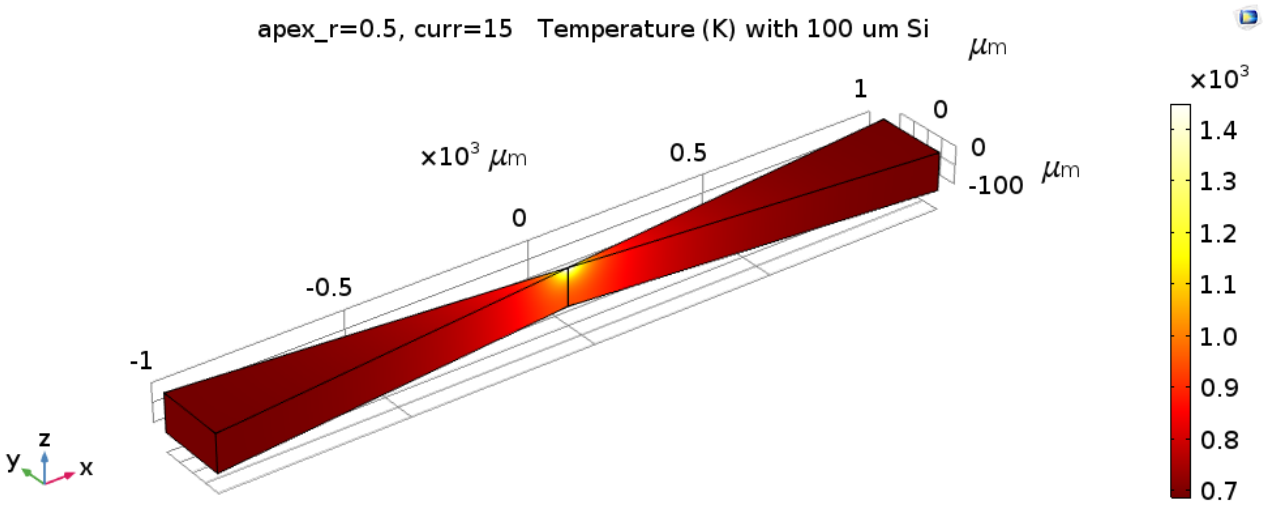

Figure 3.2: Geometry for COMSOL simulation of the device heating, the size of the apex was varied. The heat map shown is the result of a simulation of a current set to 15 mA and apex size is 0.5 µm. The maximal heating is shown at the narrowing which represents the apex of the tip.

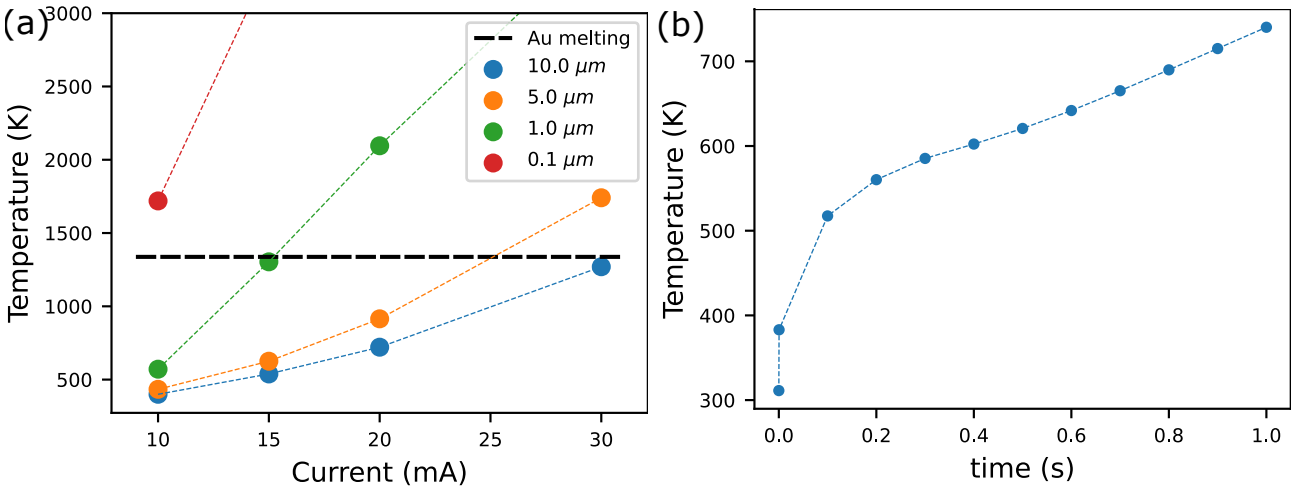

Figure 3.3: (a) The temperature of Au as a function of the current applied to the device for varying tip size. The temperature is compared to the Au melting point. (b) Change in temperature over time for an apex diameter of 1 µm and a current of 15 mA.

3.1.2 Simulating the magnetic field

The fundamental feature of the current focusing device is the magnetic field induced by the tip. The geometry of the tip dictates the field and can be simulated by numerically solving the Biot-Savart equation (Eq. 3.2) for the wire geometry. The numerical calculation used was an open-source code developed by L. Queval[110]. Essentially, a geometry is defined for the current focusing device and split into segments for which Eq. 3.2 is computed and summed over all the segments at each required point in space.

$$\mathbf{B}(\mathbf{r},t) = \frac{\mu_0}{4\pi}\int \frac{I(t)dl \times \mathbf{r}'}{|\mathbf{r}'|^3}. \tag{3.2}$$

Here $\mathbf{B}(\mathbf{r})$ is the magnetic field at $\mathbf{r}$, Idl is the current source with infinitesimal length dl at a distance $\mathbf{r}' = \mathbf{r} - dl$ to the computed point, $\mathbf{r}$, $\mu_0 = 4\pi \cdot 10^{-7}$ T · m/A is the vacuum permeability.

The wire can be described in three portions consisting of two leads that are connected at the apex and is shown in Fig. 3.4 The angle between the lead to the apex was set according to measurements from tips fabricated in this work and set to be $\alpha = \arctan(r/H) = 7.7°$, where the value $r = 1.97$ µm is the cross-section of the tip at the distance $H = 7.29$ µm to the apex. To describe the device in 3D, N wires are combined in parallel and set the current on each wire to be $\frac{I_0}{N}$, where I_0 is the total current. In each calculation the specific geometry is controlled including the size of the apex and the length of the leads included in the calculation.

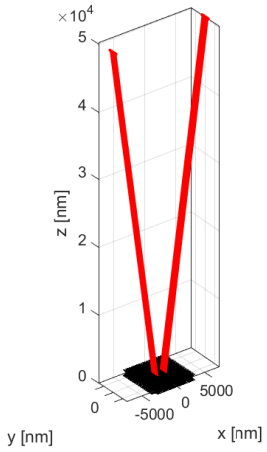

Figure 3.4: The geometry used for numerically calculating the field of the tip. The wire is shown in red and the field points are marked in black. Here the apex size is set to 1 µm and the field is measured 200 nm below the wire. The wire extends to a distance of 50 µm from the apex.

This configuration attempts to accurately describe the current focusing device yet it inherently has deviations from the true device and as such the magnet field measured may deviate from the simulation. The calculation does not account for the deposition thickness and for the distribution of the current within the gold layer. It also does not include the shape of the quartz tip which is rounded. In the fabricated device the two leads are separated only be a narrow space (less than 200 nm) and so the leads are closer to each other than in the simulation. Despite these deviations, the simulation achieves an estimate for the field.

Simulating a tip with 1.3 µm apex

In this work I used a tip apex size of 1.3 µm. The expected magnetic field for these dimensions was simulated and is shown in Fig. 3.5 showing the cross section in plane to the tip and parallel to the tip apex. The strength of the magnetic field is weak - not more than 5 G at a distance of 200 nm between the tip to the NV. Hence, it is not expected to interfere with the NV contrast[32] as shown in Fig. 2.5.

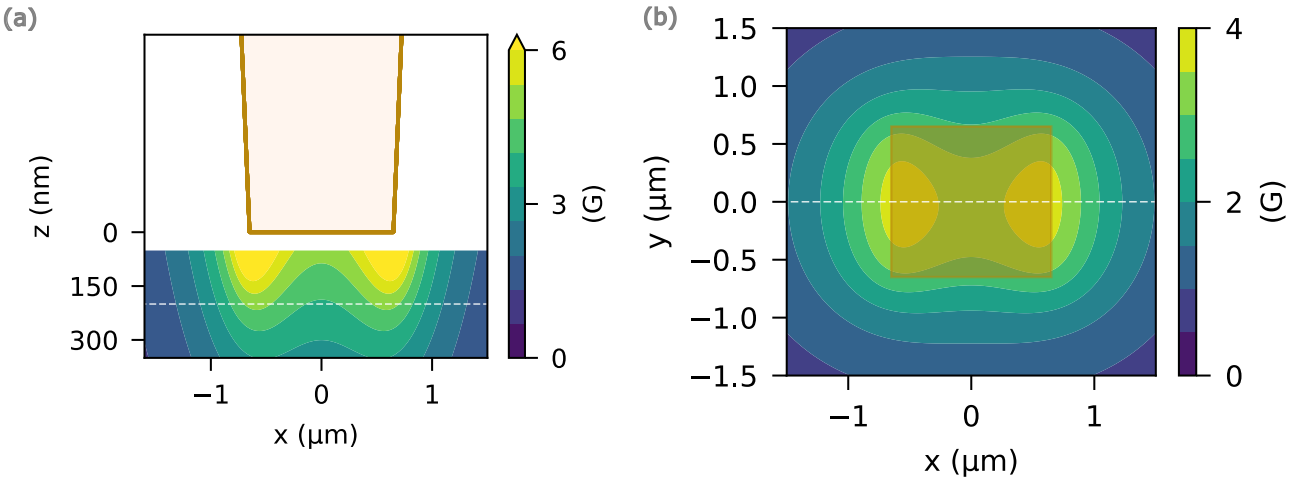

Figure 3.5: Simulation of the magnetic field of the wire. (a) The tip is shown in the colored region above the $z = 0$ level, the cross section is in plane of the tip at the center of the tip the diamond surface is 50 nm below the tip. (b) cross section parallel to the tip apex, the colored square is the location of the tip above the surface. The simulation shows the field 200 nm below the tip apex. The white dashed line in each image is the location of the cross-section of the other image.

To estimate the expected gradient of the CFD magnetic field we calculate the 2D numerical gradient of the simulated field (apex size 1300 nm, current 2 mA, distance from apex 300 nm), Fig. 3.6. This gradient is calculated from the magnitude of the field, $|\nabla|B|| = \sqrt{(\frac{\partial|B|}{\partial x})^2 + (\frac{\partial|B|}{\partial y})^2}$, where the gradient along x and y are calculated using Python *numpy* gradient implemented for second-order accurate central differences. Two peak regions are visible where the maximum is found near the edge of the tip and the value calculated is 0.35 µT/nm. This may deviate from the actual measurement. First, the magnetic field measured is projected along the NV axis thus the actual values measured will differ from the simulation. For the purpose of nanoMRI it is the full vector field that will be applied to a sample and as such the gradient is calculated for this field. Additionaly, this is the maximal gradient and is found at a specific point, the 2D measurements are done at a lower resolution than the simulation and will likely not probe the specific maximal point of the highest resolution.

Simulating a tip with 100 nm apex

Initial attempts to create a current focusing device used a tip with an apex on the order of 100 nm. This was chosen in order to achieve a significant gradient and was later found to fail due to heating. The expected field of such a wire was simulated and is shown at a distance of 200 nm in a range of 200 nm around the tip, see Fig.3.7. At this distance, for a current of 2 mA, the maximum gradient is 0.89 µT/nm, see Fig. 3.16 in discussion Sec 3.5 below.

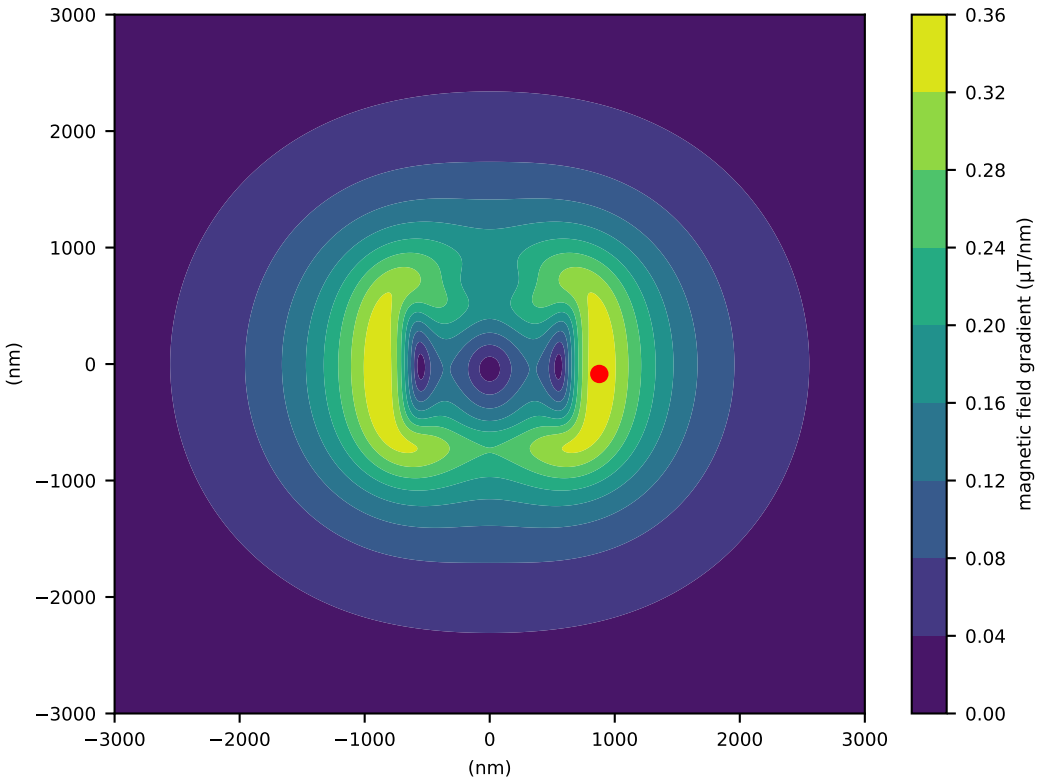

Figure 3.6: Gradient of the simulated magnetic field of the tip at a distance of 300 nm below the apex. The red dot is the point with the maximum gradient.

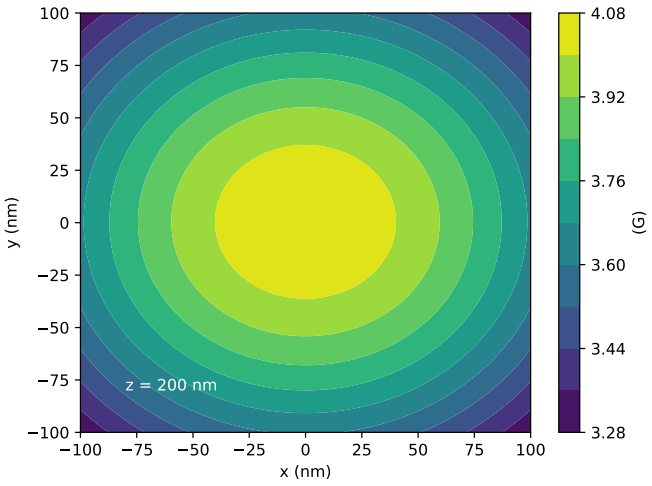

Figure 3.7: Magnetic field simulated for an apex diameter of 100 nm apex at a distance of 200 nm from the tip.

The fabrication of the CFD includes several stages in order to achieve a device with the required dimensions and avoid shorting the two leads. It was found that the deposition at the apex can cause a short-circuit due to material deposited in the region separating the two leads. This results in the current flowing around the side of the tip instead of through the apex and the gradient is not achieved. The protocol described here is intended to achieve a tip with the required dimensions for a practical gradient, mitigate the short-circuit and raise the fidelity of the tip fabrication. The process consists of three main steps - pull a quartz rod to a tip with 100 nm apex, use FIB to cut the apex to the desired dimension, deposit metal along three sides, as shown in Fig. 3.8. In each batch process four tips are prepared yet only in one to two of the tips does the current flow across the apex. The full details are described in the following section.

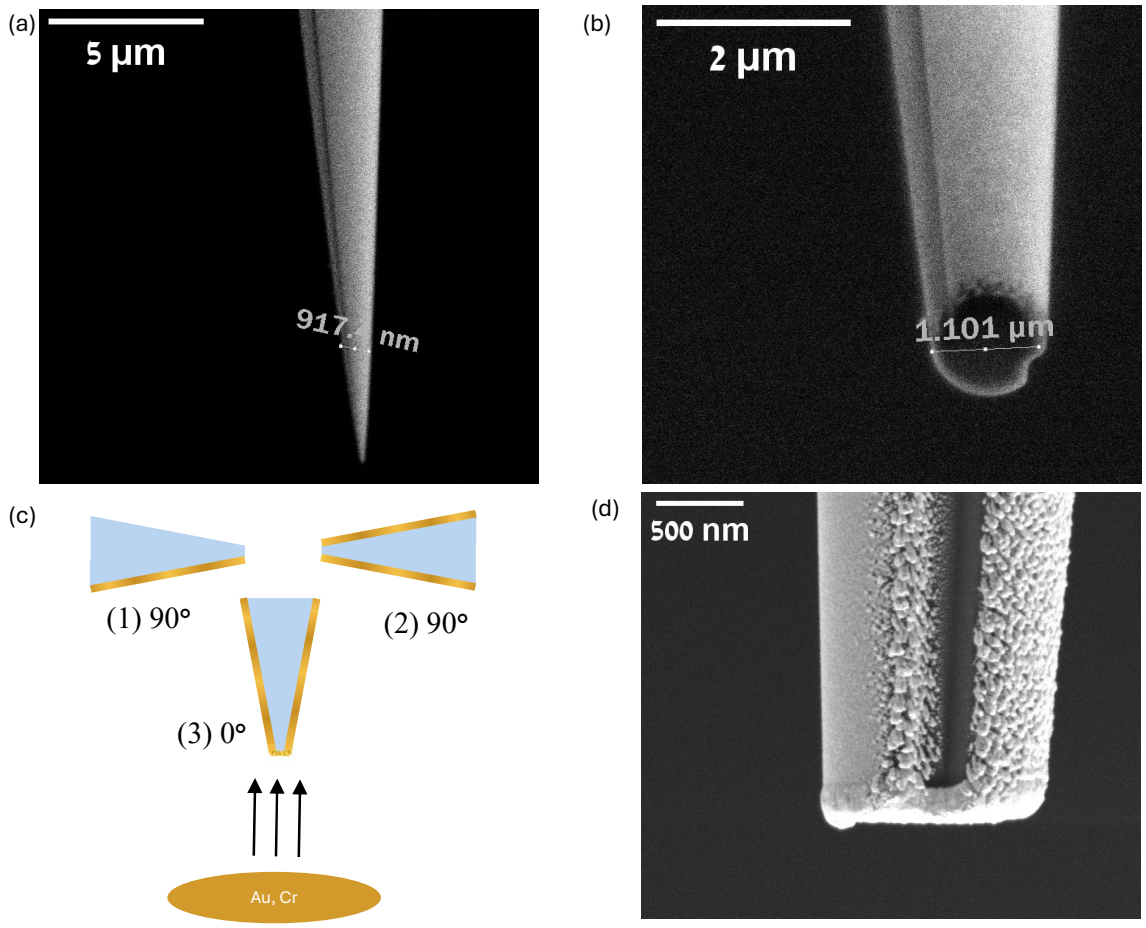

Figure 3.8: Process of tip fabrication. (a) Tip is pulled from quartz rod to have a narrow taper and an apex on the order of 100 nm. (b) The tip is cut using an FIB to obtain an apex on the order of 1000 nm. (c) Schematic showing the deposition on the tip from three angles, first the two leads are deposited at the angles $\pm 90°$ followed by the apex deposition at $0°$. (d) An SEM image of the fabricated tip showing the metal deposition on the leads and at the apex and the gap between the leads.

The process starts with a bare solid quartz rod with a diameter of 1 mm and length 75 mm and includes two grooves on opposite ends (purchased from *Friedrich & Dimmock Inc.*) - see Fig. B.5. To form micro-pipettes the quartz rod is heated at the center with a laser and pulled on the two

sides, this results in two micro-pipettes with similar properties (taper length and apex size). This is achieved using a laser-based micro-pipette puller *P-2000, Sutter Instrument Company* which effectively melts the glass at the center of the rod and when cooled the glass hardens to the tapered shape. The micro-pipette properties are controlled by the recipe used and include the following parameters[111] -

- **Heat** - specifies the output power of the laser.
- **Filament** - specifies the laser scanning pattern.
- **Velocity** - specifies the glass temperature at which the pulling begins.
- **Delay** - controls the wait time between the final pull to the time when the laser is shut off (128 is zero delay).
- **Pull** - dictates the strength of the pull.

In this work the recipe used is shown in Table 3.1 and is intended for working with solid quartz rods resulting in a diameter on the order of 100 nm and a taper length of roughly 5 mm - an SEM image of the tip is shown in Fig. 3.8(a).

	Heat	Filament	Velocity	Delay	Pull
step 1	850	5	20	128	118
step 2	600	4	65	128	120

Table 3.1: Tip pulling recipe used in this work results in an apex on the order of 100 nm and taper size 5 mm. The recipe is cycled until the quartz rod is separated into two tips. The number of cycles and the time that the heat was applied during the last line are constant if the recipe is reproducible.

After pulling, the tip tail is cut with a diamond scriber to the desired length such that the tip, from base to apex, fits within the metal grid holder intended for deposition (Fig. B.6). Using a soldering iron, the leads far from the tapered region are coated with a thin layer of indium. This layer improves the mechanical and electric contact to the holder for the AFM microscope. The tips are placed in the grid such that the indium is exposed for the deposition and the grooves face the metal within the holder to avoid deposition in this region. The bases of the tips are covered using *Kapton* tape. This holds the tips within the grid and prevents deposition at the tip base which can create a short.

In preparation for the FIB a thin deposition of 7 nm Cr and 10 nm Au is performed on the leads. This is intended so that the tips are conductive and as such will improve the image of the electron beam. Next, the tip is cut using FIB so that the diameter of the apex is on the order of 1 µm. The FIB working current was 48 pA - this controls the force removing the material. When etching the tip with the FIB, material is removed from the apex gradually until cutting the tip to the desired size. The tip after cutting with the FIB is shown in Fig. 3.8(b), showing a flat apex with a diameter of 1300 nm.

The final step for fabrication is the deposition of the leads and apex. For the apex deposition a metal mask was placed on the two sides of the grid holder (see Fig. B.7). This is intended to

prevent deposition in the grooves and avoid shorting the tip. The thermal deposition is done in a home built deposition chamber[112] in the lab of Prof. Eli Zeldov, and allows the tips to be rotated within the deposition chamber. For the apex deposition, the tips face the boat with the material (see Fig. 3.8(c)), and 7.5 nm Cr is deposited, followed by 125 nm Au. For the lead deposition, the metal mask is removed, and then the two leads are deposited (see Fig. 3.8(c) with 7.5 nm Cr followed by 50 nm Au. The final tip with deposition is shown in Fig. 3.8(d).

For characterization, all tips are imaged by SEM. The quality of the deposition and the groove are examined, Fig. 3.9 shows examples of such tips. In Fig. 3.9(a),(b) there are two examples of poor deposition, in (a) the metal did not form a uniform layer on the quartz and in (b) the apex deposition is thin and patchy, both result in tips with resistance on the order of MΩ and are not useful. An example of a tip with deposition in the groove that will lead to current flowing around the side of the tip is shown in Fig. 3.9(c),(d) showing two sides of the same tip. In Fig. 3.9(c) the groove is clear while on the opposite side in Fig. 3.9(d) there is material in the groove. The last pair, Fig. 3.9(e),(f) shows the two sides of a good deposition where both grooves are clear and the current is expected to flow across the apex. The resistance is also an indication of the tip quality and was measured for each tip using a multimeter. Low resistance, up to 100 Ω, points to a short, while high resistance, over 1 kΩ, indicates the tip cannot sustain enough current. The proper range is 150-400 Ω resistance.

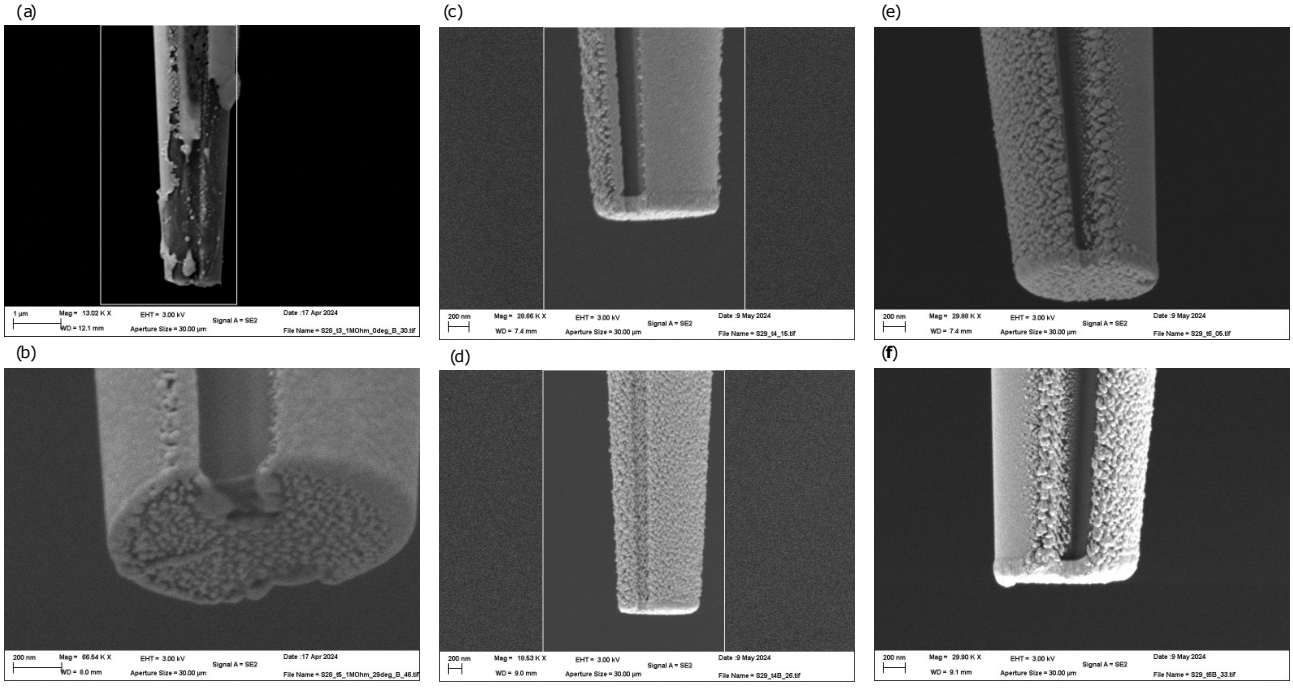

Figure 3.9: SEM images comparing tips with failed and successful deposition. (a) Metal deposition is non uniform. (b) Thin deposition at the apex. (c),(d) Two sides of the same tip, where (d) has deposition within the groove and results in a short circuit. (e),(f) Two sides of a proper deposition on a tip, the gold deposition is uniform and the grooves on both sides are bare.

3.3 Incorporating the CFD in the NV microscope

As described in Ch. 2.3 the NV setup consists of an optical excitation and detection, a microwave antenna needed for interacting with the NV and a permanent magnet which is aligned to the NV

axis. To achieve a local gradient magnetic field the CFD must be incorporated in the vicinity of the NV along with these elements. The system used for combining these elements is the *Attocube attoCSFM*, which combines optical access below a sample stage for the diamond along with a piezoelectric stage intended for AFM feedback for the tip. The system incorporates AFM feedback using frequency modulation AFM with the attocube ASC500 controller. The attocube microscope consists of four stages each with piezoelectric coarse motion - objective stage (z motion), sample stage (x,y,z motion), tip stage (x,y,z motion) and a permanent magnet stage (x,y,z motion). It additionally includes a temperature stability system using a *Lakeshore 335* controller. Tip scanning with respect to the diamond was done using attocube piezo scanners (3×ANSx301). The setup combining the diamond placed on the waveguide and showing the permanent magnet along side the tip in the holder is shown in Fig. 3.10. The tip holder apparatus limits the scan range of the magnet which in turn prevents access to some of the four NV orientations, see Fig. 3.10. The

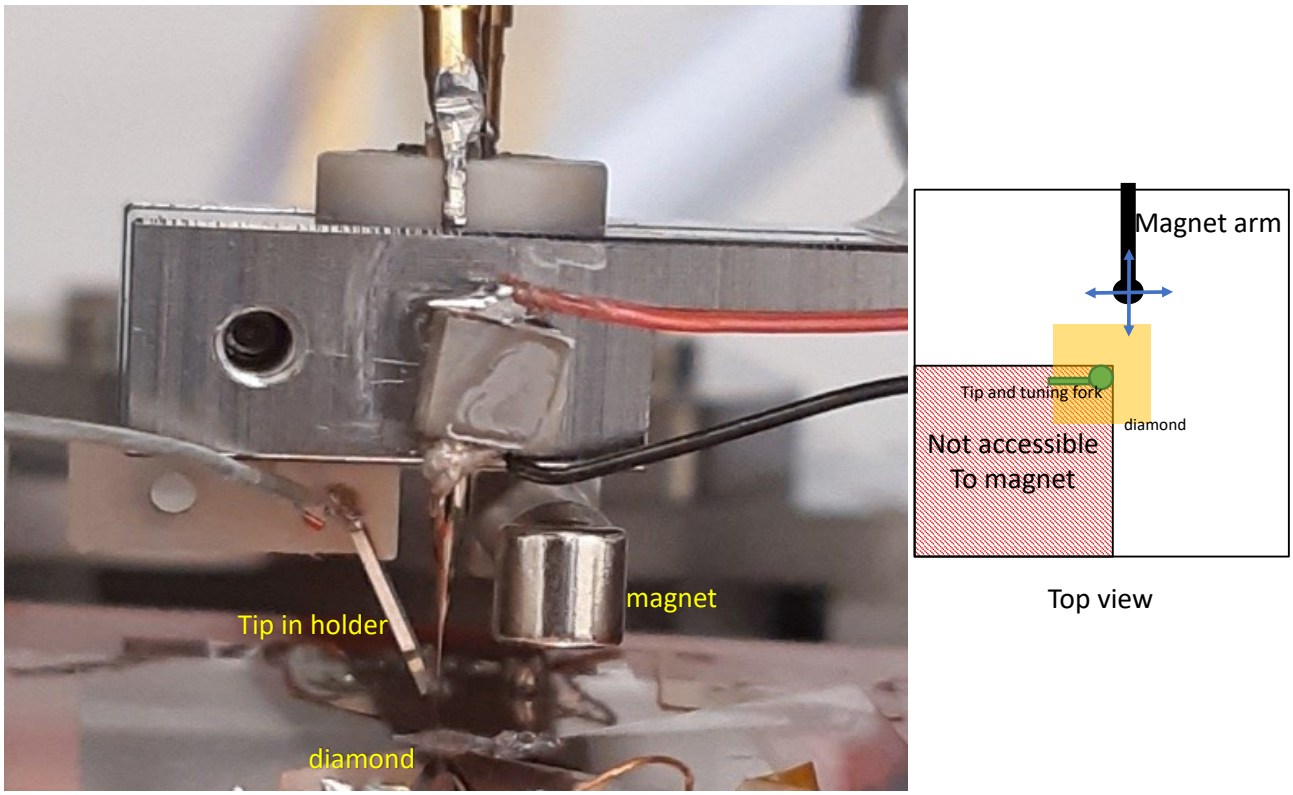

Figure 3.10: (left)Photo of the setup combining the diamond membrane, the tip in the holder and the permanent magnet. Below the tip is the diamond membrane placed on a copper waveguide which was deposited on a glass slide. The waveguide sits on a PCB providing input and output connections to the microwave signal. The tip is pressed against the tuning fork and held in the PEEK holder which is placed within a metal holder. Two electric pins appear on the top and provide the electric connection to the tip. The permanent magnet is shown to the right of the tip. (right) A top-view schematic of the setup illustrates how the placement of the magnet is constrained by the presence of the tip and tuning fork. The magnet is aligned along the NV axis; however, spatial limitations prevent access to certain NV orientations. In particular, the magnet cannot be positioned directly above the diamond, which restricts the maximum magnetic field that can be applied.

working region of the tip relative to the diamond and the waveguide is shown in the schematic cross-section in Fig. 3.11. To provide maximal MW power along with optical access, the working region in the diamond is next to the center line. The tip is positioned near the surface of the diamond within the working region.

The process of incorporating the tip in the NV setup and locating the tip is described below and summarized in Fig. 3.12.

3.3.1 Tip holder

The tip is placed on a piezoelectric stage which controls its location in x, y and z relative to the diamond sample. A cylindrical PEEK tip holder was designed to hold the tip at the center (design in Fig. B.8) with two metal springs that provide electric contact to each lead. Each spring is connected to a coaxial cable to connect to the electric current circuit. A quartz tuning fork ($f_0 = 32.768\,\mathrm{kHz}$, *HM International BVBA*, model TB-38-20-12.5-32.768) is used for feedback to control the dis-

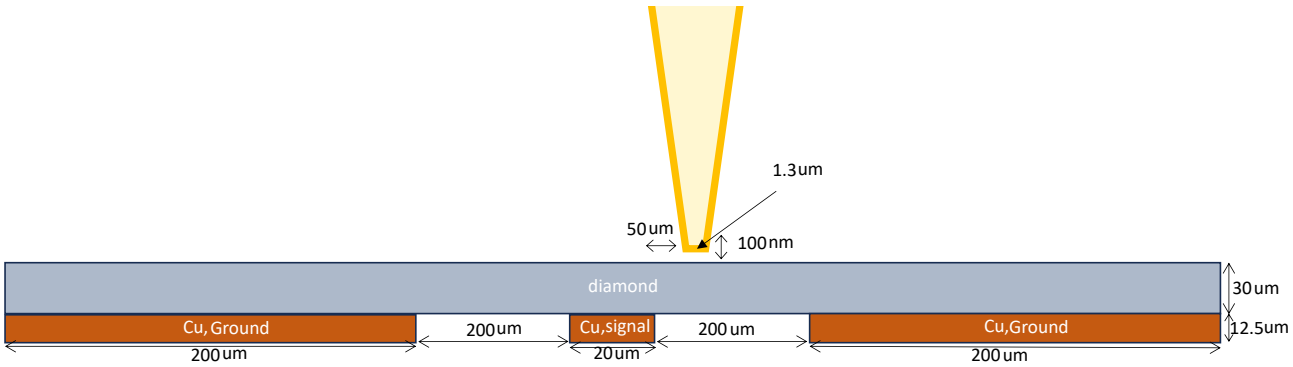

Figure 3.11: Cross-section of the tip above the diamond (not to scale). The schematic shows the dimension of the wave-guide with the diamond placed above and the relative position of the tip.

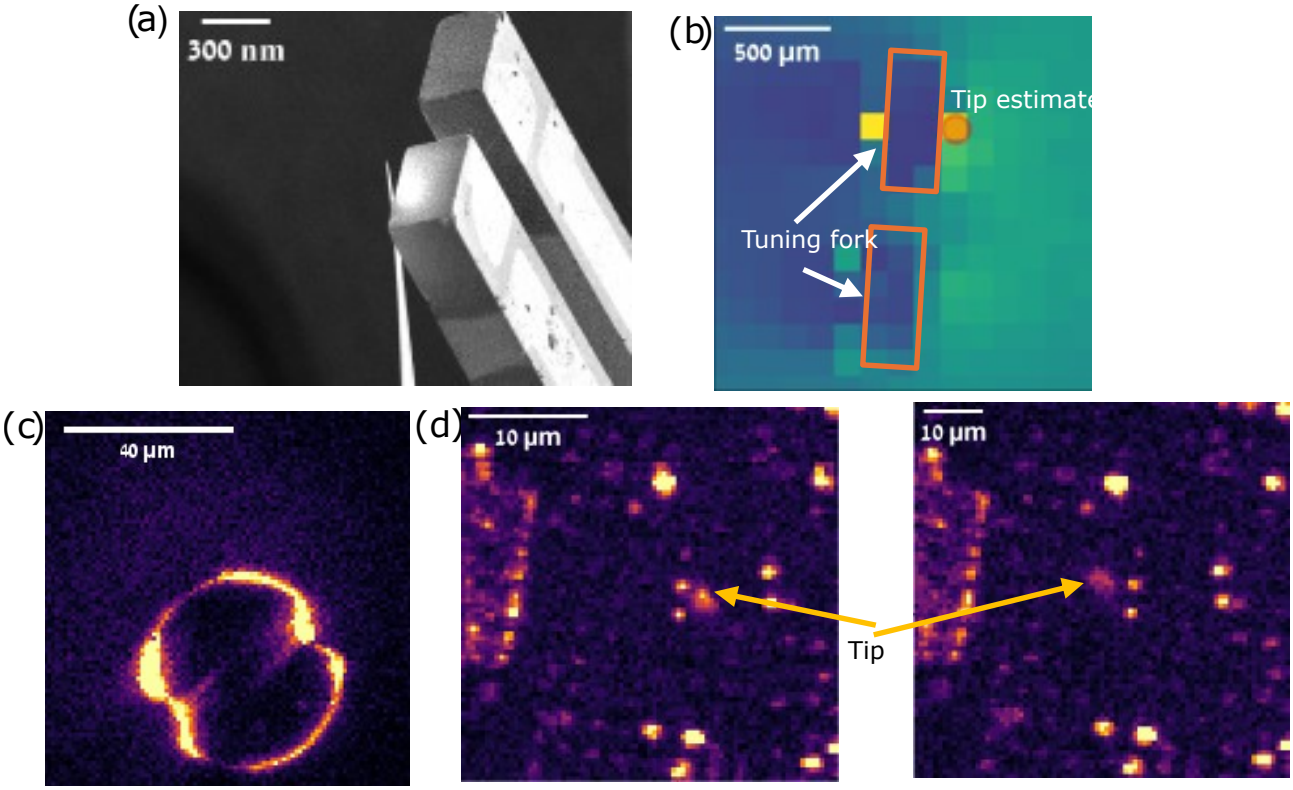

Figure 3.12: The process of incorporating the tip in the NV setup and locating it. (a) The tip is pressed against the tuning fork to provide AFM feedback for surface contact. (b) The tip is scanned with the laser to obtain a coarse location of the tip. (c) A cross section of the tip is scanned. (d) The tip is in contact with the diamond and located by moving the tip.

tance between the tip to the surface. The electronic connection to the tuning fork is done by soldering a delicate coaxial cable to the two electrodes, the wire used is MK5005-SMA11-offen-0200 purchased from *elspec group*. The tuning fork is then glued to a PEEK holder (Fig. B.9). Finally, the tuning fork is pressed against the tip using a micro-positioner and a live camera, ensuring tip to tuning fork contact and preventing the tuning fork from damaging the tip, Fig. 3.13. The tuning fork holder is connected to the tip holder with superglue and is cured overnight - this can later be removed with acetone as needed.

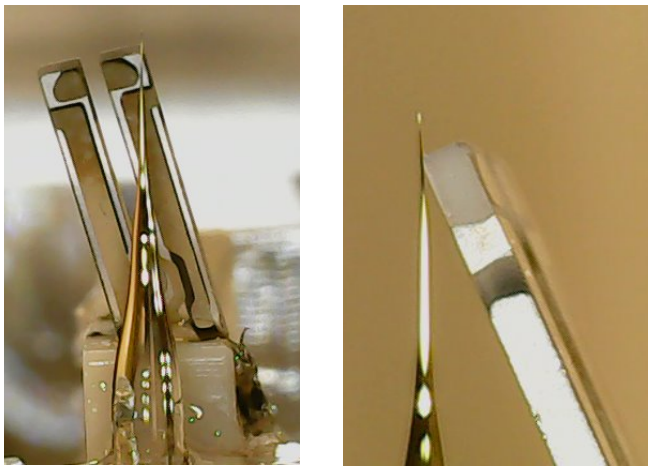

Figure 3.13: The tip is pressed against the tuning fork to allow feedback for the AFM contact to bring the tip to the diamond surface without damaging the tip. Two live cameras are used to view the contact from different angles.

3.3.2 Co-alignment of the tip with the confocal microscope

The CFD apex is on the order of 1 µm and must be aligned to the working NV to apply a magnetic field that can be detected by the NV. The optical focal point defines the working NV and is within the optical fiel of view (FOV). A series of scans is performed in order to align the tip within the FOV and adjacent to the NV. First, the sample is removed and the tip is scanned above the objective over a range of roughly 1500 µm × 1500 µm, while monitoring fluorescence in each scanned position, the resulting image is shown in Fig. 3.12(b). This leverages the large dimensions of the tuning fork which is detected in the scan. The tip location is estimated from its relative position to the tuning fork which is shown in the image in Fig. 3.13, this image is captured for every new tip and is different in every iteration. The tip is set to the estimated location, and a confocal scan is done to confirm the tip is within the FOV by imaging a cross-section of the tip as shown in Fig. 3.12(c). Finally, the tip is raised far from contact and the sample is placed in the setup. At this point the AFM is used to detect the contact point of the tip with the surface. After this, confocal scans confirm the detection of the tip by moving the tip and comparing the confocal scans, see Fig. 3.12(d). Noticeably, the tip apex does not always appear at the center of the larger cross-section, and the last step is critical for detecting the tip. The apex dimension, being larger than the diffraction limit, gives the tip the advantage of being visible in the confocal image. Working with a tip smaller than the diffraction limit would hinder visibility.

$$d = \frac{\lambda}{2NA} = \frac{520\,\text{nm}}{2 \cdot 0.9} \approx 300\,\text{nm} \tag{3.3}$$

Eq. 3.3 shows a calculation for the diffraction limit d, where λ is the wavelength and NA is the numerical aperture.

3.3.3 AFM feedback

AFM feedback is used to control the working distance of the tip to the diamond surface. During experiments, the tip is set to a specific retracted distance from the surface and is not in contact with the surface. The height of the surface is found from a contact scan and the tip is set to a specific distance from the contact point. In this manner the tip is safe from crashing and is held at a constant height and does not fluctuate as would be if the tip were in feedback mode. It is noted that during measurements the phase locked loop (PLL) is active, thus if there are drifts in the system the tip will retract and not crash. The excitation is done with a dither piezoelectric glued to the tip holder adapter. The PLL feedback[113] controls two loops, a frequency control loop and a distance control loop, see Fig. 3.14(a). First a frequency control keeps the excitation frequency locked to the resonance by locking the phase between the excitation to the resonance to $\pi/2$ (an example of the resonance curve is shown in Fig. 3.14(b)). Typical parameters for the frequency loop are $P = 500 \cdot 10^{-6}$(kHz/deg) and $I = 5 \cdot 10^{-3}$(kHz/deg/s). The second loop controls the tip to surface distance, z, this is achieved by controlling the shift in resonance frequency to be a set shift defined by the user. Here, typical parameters used are $P = 1 \cdot 10^{-3}$ µm/Hz and $I = 350 \cdot 10^{-3}$ µm/Hz/s and the set-point used was 600 Hz (a higher set point of 1 Hz resulted in the tip crashing).

3.4 Electric control of the CFD

The current through the tip is created by a voltage applied by the AWG and then amplified by a Stanford Research Systems amplifier with a ×10 gain. The amplified signal is transmitted to the tip through a thin coaxial cable connected to an input pin, while another coaxial cable connects an output pin to an oscilloscope with a 50-Ohm termination for readout. The AWG is used to synchronize the signal to the NV. The MW signal to the NV is created by Rohde & Schwarz synthesizer, which is modulated by an arbitrary waveform generator (AWG). It is then amplified by a Minicircuits ZHL-43-16W and fed into the co-planar waveguide via SMA ports. The transmitted signal is connected to a 4 GHz, 20 GS/s oscilloscope with a 50 Ohm termination.

3.5 Discussion

In this chapter, we presented a current-flowing device (CFD) integrated within an NV-based confocal microscope. The design of the device balances two key requirements: effective heat management and the generation of a high magnetic field gradient. Particular attention was given to guiding the current flow through the apex of the tip, avoiding short-circuit current paths along the tip side. This involved not only the fabrication of the tip but also its integration into the NV

microscope, precise positioning near the NV center, alignment with a permanent magnet, and the development of electronic control for current delivery.

Although a tip with a 1300 nm apex was successfully fabricated, exploring the benefits of a smaller apex remains of interest. As mentioned, from an optical perspective, the minimal apex size that is recommended is on the order of the optical diffraction limit since this is advantageous when locating the tip nearby a single NV. From a thermal perspective, there is room for optimizing the apex dimension in order to find the smallest possible tip that can sustain a current. A large cross-section can be achieved by increasing the deposition thickness so that for a given apex radius, the overall cross-section area is increased in order to support larger currents. More detailed simulations and experiments can be done to find the optimal apex size and deposition thickness.

Simulations of the gradient of the magnetic field comparing the large apex to a fine apex are shown in Fig. 3.16. In both the fine and large dimensions the gradient is maximal near the edge of the tip where the current changes direction. At a distance of 200 nm from the tip the gradient

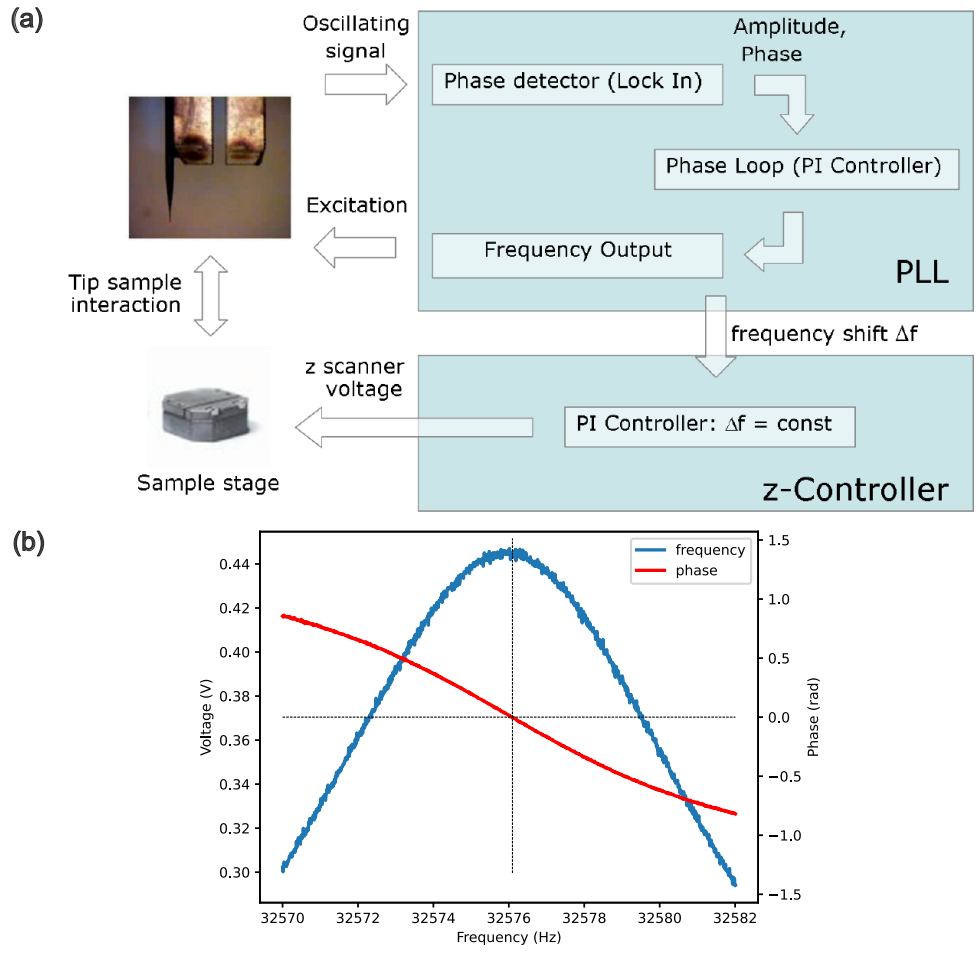

Figure 3.14: (a) Schematic of PLL loop which controls the tip distance to the surface. The control is done with two loops, a phase control and a distance control. The phase loop is used to control the oscillation frequency of the tuning fork and is set such that the phase between the excitation and the oscillation of the tuning fork is $\frac{\pi}{2}$. The second loop controls the distance to the surface, the distance is set such that the the frequency shift is controlled and held at a given value. Image from the *attocube* ASC500 manual. (b) (blue) The resonance curve of the tuning fork showing the response of the tuning fork to varying excitation frequency. (red) The equivalent phase curve. The working point is set such that the phase is zero and is marked with the dashed black lines.

simulated for the large and fine tip are a similar order of magnitude and it does not appear that there is an advantage for working with a fine apex. Yet, at a distance of 50 nm to the surface, the difference between the two apex sizes becomes significant, and the maximal gradient is an order of magnitude better with a fine tip, meaning there is an advantage to working with the fine apex. The range of the magnetic field is local and is on the order of the tip diameter. Working with a large tip may make it easier to find the working region and can hold an advantage. The device was designed to apply local electromagnetic fields in the vicinity of an atomic defect. The main goal presented here is to achieve nanoMRI by inducing a local gradient in the magnetic field. Indeed, magnetic field measurements of the tip that support this aim are presented in the following chapter. Yet, beyond nanoMRI, the device can be employed for broader applications in nanoscale magnetometry. Questions regarding the response of materials to an external magnetic field can be studied by applying a field that is controlled during the experiment. It can be used to study magnetic materials, 2D materials, monolayers or current and spin transport in nanoscale devices.

Here, a room-temperature setup is demonstrated yet working at cryogenic temperatures will likely have advantages as well. The choice of working temperature depends on the sample at hand; while some phenomena are of interest at room temperature, such as biological interactions in a natural environment, other samples will gain from low temperature, particularly when the sample suffers from thermal drift. Additionally, studying low-temperature physics is of interest to explore phenomena that uniquely arise there. Developing a low-temperature device would require examining the limitations of such a setup, including optics, spatial constraints, and heating. The possibility for a superconducting current would be available at low temperatures, which will remove the need for a large device discussed above and will allow one to reach stronger gradients.

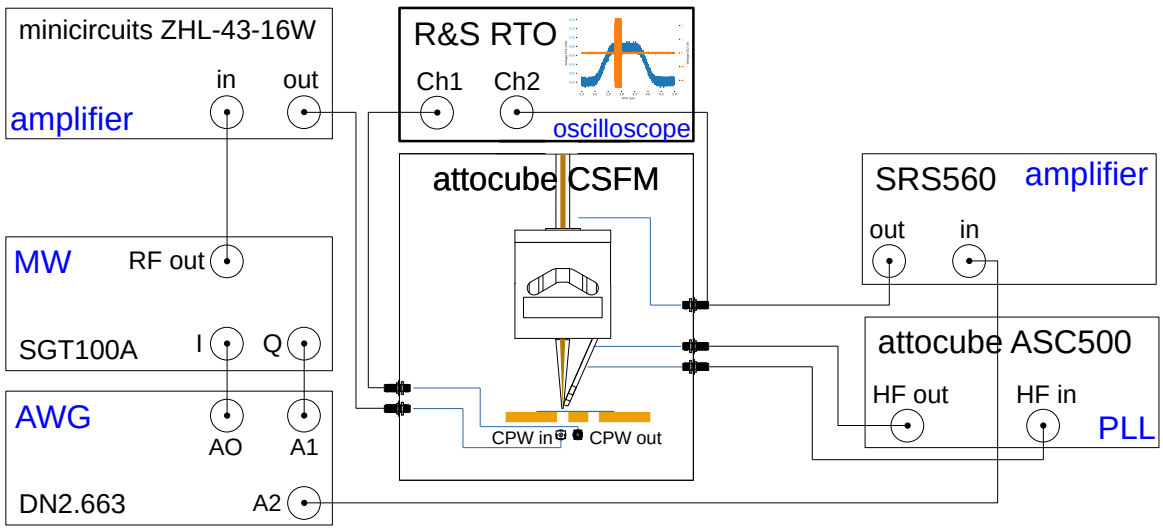

Figure 3.15: MW/RF circuit schematic. The microwave (MW) vector generator's I and Q ports are modulated by an arbitrary waveform generator (AWG), and the RF signal is then amplified and sent to a co-planar waveguide (CPW), on which the diamond membrane is positioned. The current to the tip is fed by a separate signal from the AWG, amplified and monitored by an oscilloscope. The tip is glued to a tuning fork resonating at 2^{15} Hz, whose amplitude and frequency are controlled by a phase-locked loop (PLL), which in turn serves as the feedback parameter for the AFM's z-stage (controlled by the ASC500).

The implementation shown here is not necessarily the only solution, and other technologies may be attempted, each given different constraints. One such option is to use cantilever AFM instead of tuning fork AFM. A cantilever can be designed to have a current along the tip and can possibly be used to achieve a similar electromagnet. This technique is in use for SQUID magnetometry [114] and can also be considered for incorporation with NVs. A significant difference is the NV sensor, which requires an optical confocal microscope; the cantilever control would need to be incorporated in the setup including optical access to the NV and aligning the cantilever to the NV, yet in principle, this configuration is possible. The cantilever stability is also a consideration. In this work, the tip is held static at a set distance, yet if the cantilever spring constant is "soft". it may fluctuate and introduce magnetic noise.

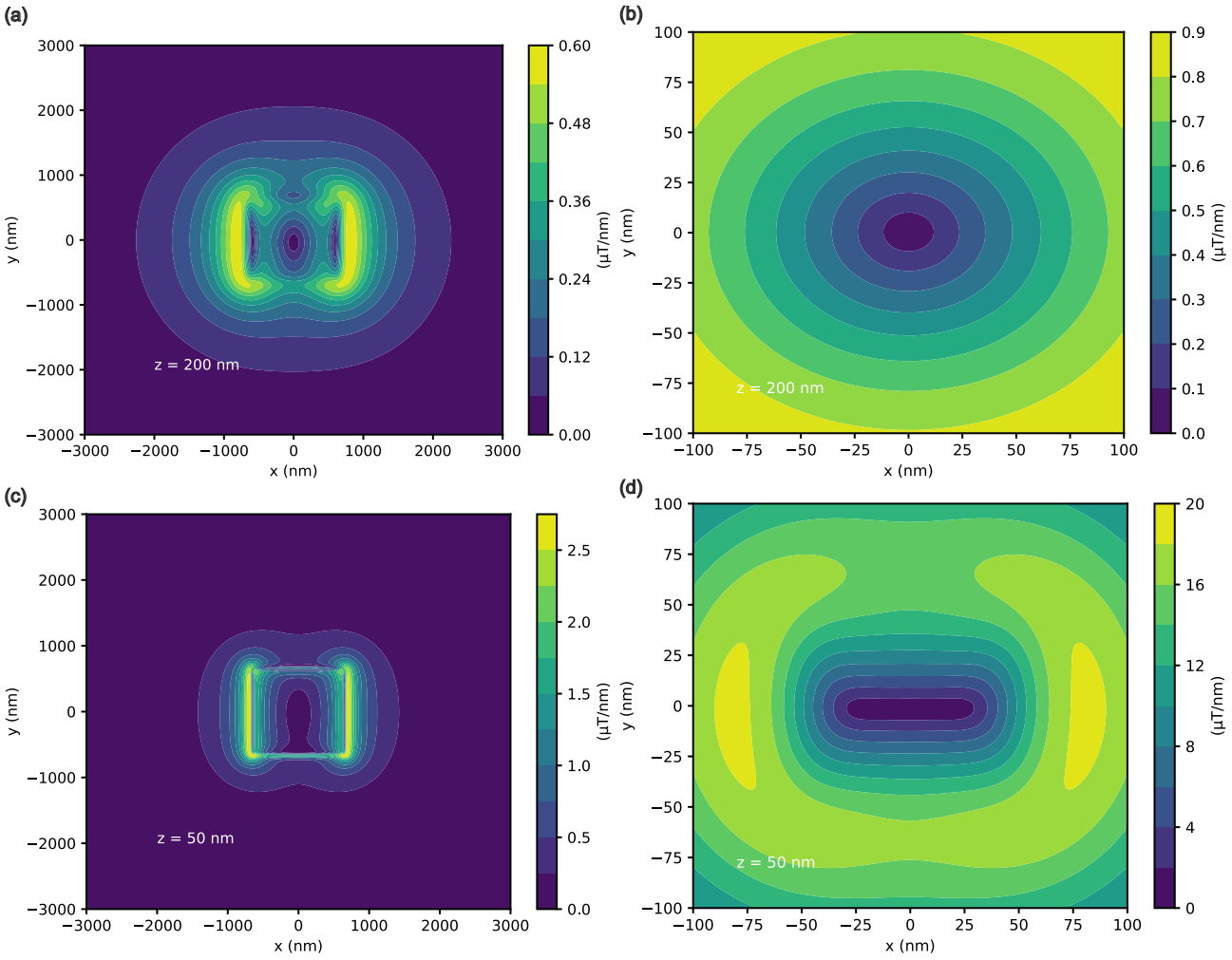

Figure 3.16: Simulation of the gradient of the magnetic field for a current of 2 mA for a large and fine apex. (a),(b) The gradient simulated at a distance of 200 nm for (a) a large apex with 1300 nm diameter and (b) for a fine tip with 100 nm apex. (c),(d) The gradient simulated at a distance of 50 nm for (c) a large apex with 1300 nm diameter and (d) for a fine tip with 100 nm apex. Notice the simulation range is different for the two diameters as the effect of the field is local and on the order of the tip diameter.

4

Pulsed magnetic field gradient

> I propose that image formation by this technique be known as zeugmatography, from the Greek Ceuyiia, "that which is used for joining"
>
> *Paul C. Lauterbur*
>
> *1973*

4.1 Background

Magnetic Resonance Imaging (MRI) operates on the principle of spatially encoding spin resonance using magnetic field gradients superimposed on a uniform background magnetic field (see Ch. 1.1). In its foundational form, as proposed and demonstrated by Paul Lauterbur [16,14], the technique relies on two distinct magnetic fields: a homogeneous static magnetic field to polarize and excite nuclear spins, and a spatially varying gradient field to differentiate spatial locations within the sample. When exposed to the static magnetic field, each spin experiences a Larmor precession frequency proportional to the local field strength. By introducing a gradient field, this frequency becomes position-dependent, enabling spatial encoding of spin signals. Conventionally, detection is carried out in the frequency domain, where the gradient along different axes is swept, and each applied gradient gives information for a different k-vector. This allows the reconstruction of the spatial distribution of spins, as each frequency component corresponds to a unique location in the sample. The contrast within an image slice, which differentiates between tissues most often, is due

to T_1 or T_2 weighing, which is controlled by the parameter swept in the pulse sequence.

Methods demonstrating nanoMRI using gradient magnetic fields rely on the same principle as conventional MRI by coupling frequencies to location. However, the detection method can vary and is achieved by selective sensing of specific spins. Bodenstedt et al. demonstrate[115] such a detection of two NVs within a single confocal spot by applying a gradient induced by a hard drive write device. When measuring ODMR, the two NVs show two distinct dips separated by 28 MHz. To determine the distance the researchers used an optical super-resolution method[116] (Deterministic Emitter Switch Microscopy) where a microwave pulse flips the spins to the dark state, using this technique they determine the two NVs are at a distance of 44.5 ± 13.2 nm apart.

Mapping of electron spins using a permanent magnetic tip was achieved by Grinolds et al.[31]. First they use Ramsey interferometry (see Sec. 2.2.1 and Fig. 2.7) to characterize the gradient of the system and achieve 3.3 Å resolution. The detection of the spins is performed using a DEER sequence (Fig. 2.9), where a resonance π-pulse is applied to the measured electron. The resonance frequency is determined by the gradient, thus different locations have different resonance frequencies. These techniques include a permanent magnet, which hinders contrast as discussed in Sec 2.1.4. Our method aims to overcome this gap and allow magnetic resonance imaging.

NanoMRI was also demonstrated using ensembles of NV and performing Fourier magnetic imaging[117,118], a technique analogous to conventional MRI. In this approach, the amplitude of the magnetic gradient field is scanned, and a modified dynamical decoupling (see Sec. 2.2.1) is applied to the NV ensemble. The resulting NV phase is a Fourier transform of the real space information in contrast to methods directly scanning real space pixels. This method requires a pulsed magnetic gradient that can be controlled within the pulse sequence. In these works, micro-coils are deposited in a set position on the diamond, producing a gradient[117] of $\nabla B = 0.7\,\mathrm{G}\,\mu\mathrm{m}^{-1}$ in the center of the coil, resulting in 3.5 nm resolution measured in the NV ensemble. Here, the position of the gradient source is permanent relative to the NV, limiting flexibility which is particularly useful for single NVs for imaging applications.

The goal of the CFD is to achieve a high magnetic field gradient in the vicinity of the NV sensor. To this end I measured the magnetic field of the tip using the NV. A series of measurements demonstrate the capabilities of the tip and the potential it holds for nanoMRI, are presented in the following sections. It was published in Communications Physics and was titled "Pulsed magnetic field gradient on a tip for nanoscale imaging of spins"[109].

4.2 Measurement setup

Measuring a DC magnetic field with the NV is performed using either an ODMR pulse sequence or a Ramsey sequence (see Sec. 2.2.1). Here, I chose to work with ODMR; it is appropriate for sensing large shifts, is simple to implement, and the results are straightforward to interpret. In order to measure the effect of the current, a modified ODMR pulse sequence is introduced, incorporating a pulse to the tip, which applies a current along the tip and induces the magnetic gradient, see Fig. 4.1. As discussed, the pulse sequence has three components - initialization, manipulation, and readout. To measure the effect of the current, the current is applied only during the phase

of spin manipulation and the current is off during spin initialization and read-out. The ODMR pulse sequence is performed in an alternative manner with current and without. In this way, each measurement of the current-induced magnetic field can be compared to a baseline without current and drifts over time are not a concern as both measurements with and without current undergo similar drift (see Fig. C.2).

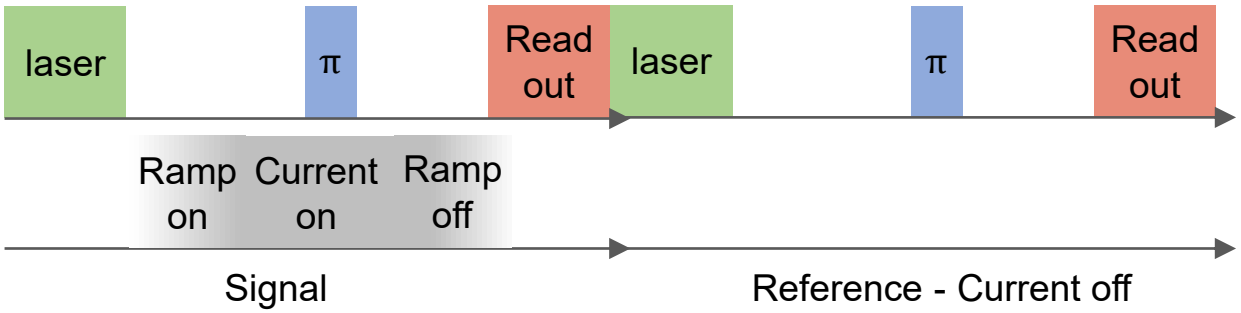

Figure 4.1: ODMR current pulse sequence. The pulse consists of a basic ODMR which is synchronized with a pulse applied to the tip to induce a current. The current is applied during the spin manipulation phase and is off during the spin initialization and read-out phases. The ODMR measurement is performed sequentially with and without current. The laser initialization and read-out are achieved with a 3 µs laser pulse at 520 nm. The pulse used to apply the current, showing the rise time, on time and fall time, is shown in Fig 4.2.

The current pulse applied to the tip was measured on an oscilloscope, see Fig. 4.2. The measurement shows the rise and fall time to be 600 ns; this was measured without the tip in the circuit and is limited by the circuit's electric components. A typical NV pulse sequence consists of initialization to $m_s = |0\rangle$, this state is stable for a time T_1 after which the state relaxes to the thermal ground state. T_1 is typically on the order of a few ms [119,120] and this is the time frame for spin manipulation; thus, a rise and fall time of 600 ns is not significant compared to the spin state stability. The amplitude of the current was 1.54 mA, which was chosen to avoid damage to the tip while achieving a measurable magnetic field.

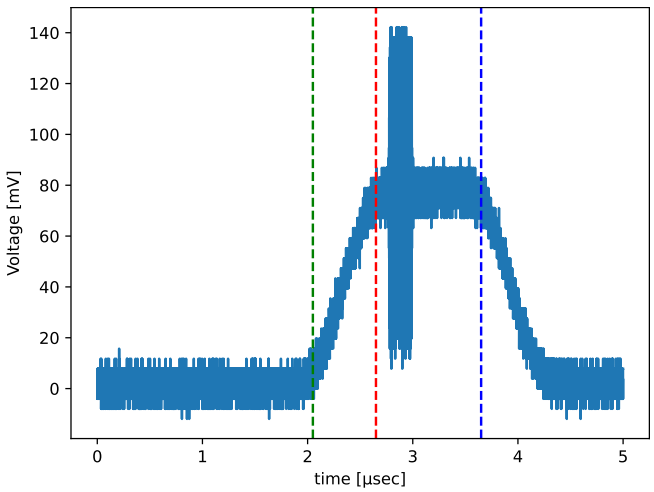

Figure 4.2: Measurement of the current on the tip during ODMR, the current shows a rise time of 600 ns followed by a 1 µs pulse where the current is on and finally a fall time. The fast oscillations shown are induced by the MW π-pulse applied during the ODMR.

For the CFD magnetic field measurement, the diamond used is an e6 [100] electronic-grade CVD diamond, overgrown with a solid state boron rod doping[119], followed by $^{15}N^{+}$ implantation at an energy of 5 keV and subsequent vacuum annealing at 950°C. The boron-doped layer was then etched with oxygen inductively coupled plasma (ICP). The diamond was thinned down to a membrane (30 µm). Patterns of arrays of nanopillars were etched into the diamond by a combination of electron beam lithography and ICP[121].

4.3 Magnetic field measurement

A single measurement of ODMR under the effect of the current on a tip is shown in Fig. 4.3(b). Each measurement consists of roughly 350,000 repetitions, which are measured over roughly 5 minutes. The π time used for the ODMR is determined from a Rabi measurement performed before the ODMR measurement (Fig. 4.3)(a). Each curve is fit to a gaussian which determines the resonance frequency. The shift in the magnetic field due to the tip is calculated as the difference between the frequency measured with and without the current. The measurement shows a shift of 9.0±0.2 MHz in the resonance frequency. From the gyromagnetic ratio $\gamma_e = 2.8{\cdot}10^4$ MHz·T^{-1} the shift in the magnetic field is calculated and is 322 ± 8 µT. This demonstrates the first requirement, which is that the tip can sustain a current that is large enough to induce a magnetic field that is sensed by the NV.

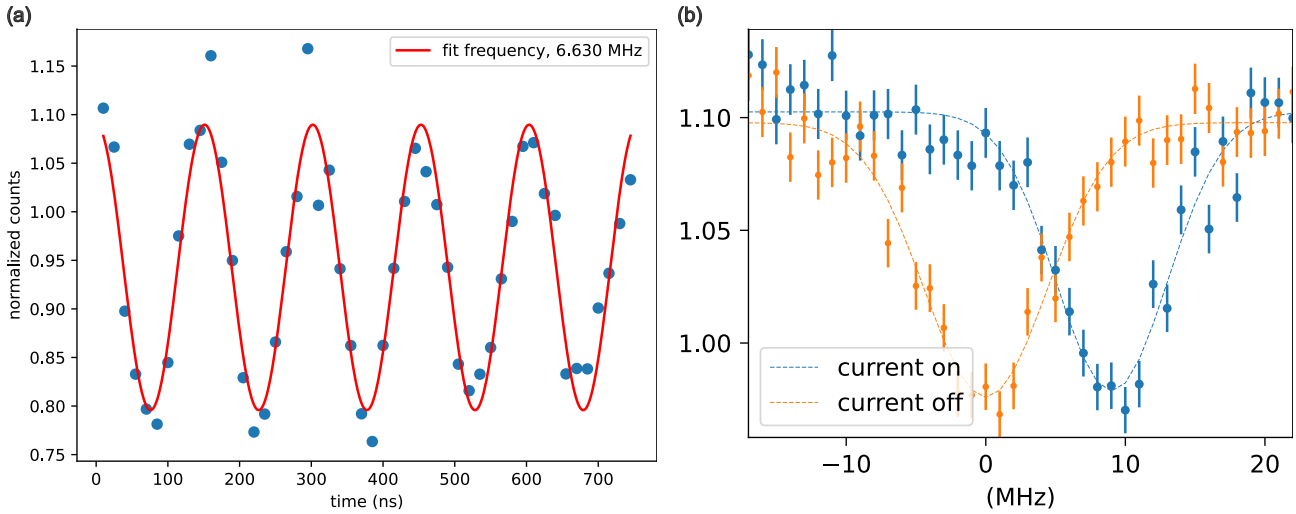

Figure 4.3: (a) Rabi measurement performed before the ODMR is used to determine the Rabi time for each ODMR measurement.(b) An ODMR measurement demonstrating the effect of the magnetic field induced by the tip. The ODMR measured with (blue) and without (orange) the current through the tip is shown.

To further demonstrate the capabilities of the tip, a series of ODMR measurements were conducted at progressively closer distances to the diamond surface. With the tip fixed at a specific lateral position, the distance to the diamond surface ("z") was systematically varied, and ODMR was measured at each z-position (Fig. 4.4b). Comparing to simulations of the magnetic field below the tip at different locations shows that the measured curve is similar to the simulation of the field beyond the edge of the tip at x=2000 nm shown in Fig. 4.4c. The value of the measured field is within range to the simulation and the curve has a similar shape and does not appear quadratic

as it would be if the NV were directly below the center of the tip (x=0). The lateral location of the tip was not determined in this measurement and so discrepancy from the simulation is expected as the measured field depends on the location relative to the tip.

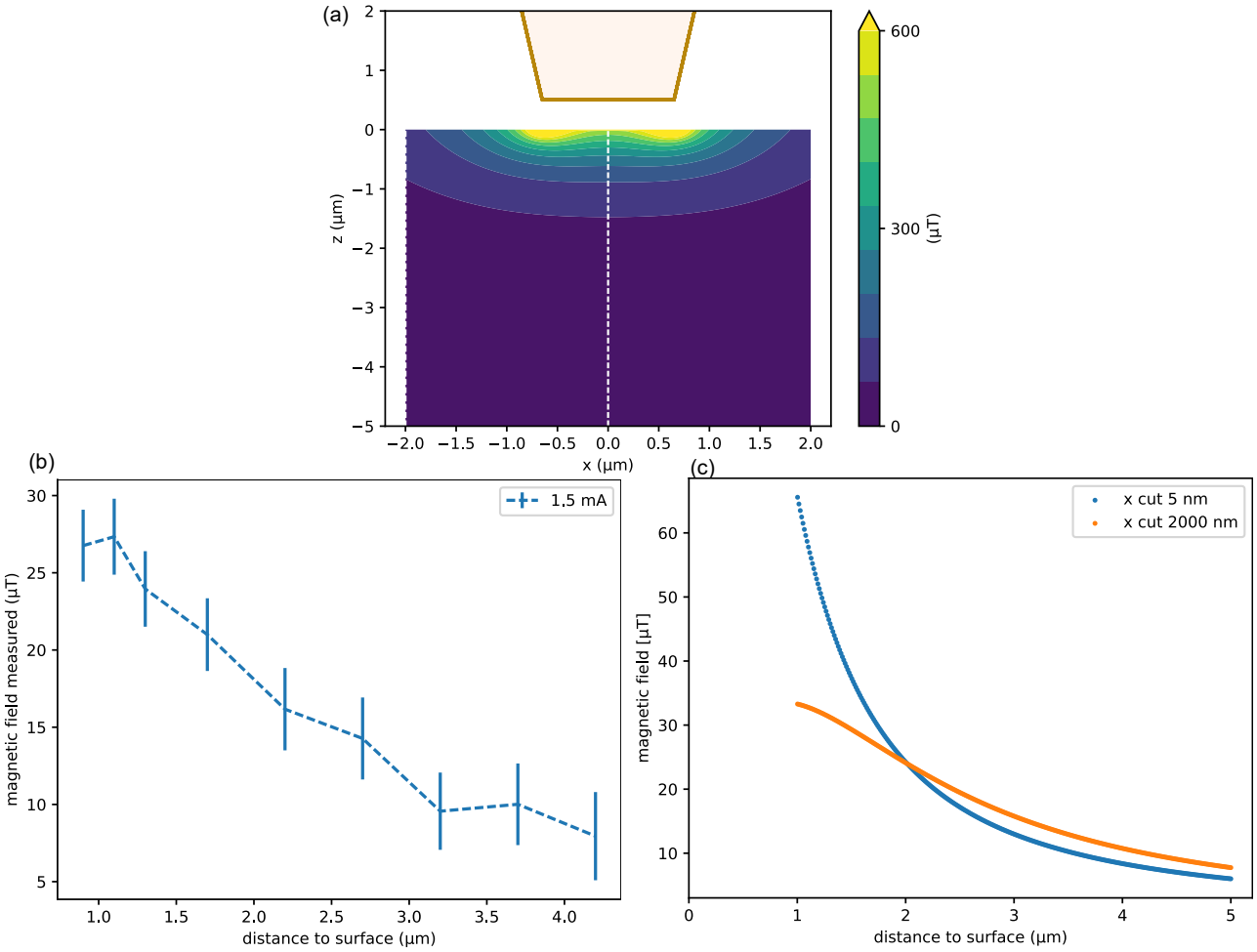

Figure 4.4: Measuring magnetic field vs. distance to surface. (a) simulation of the field induced by the CFD. The range simulated below the tip if from 500 nm to 5500 nm below the tip. The white dashed lines are plotted in (c). (b) The magnetic field measured as a function of distance to the surface. (c) line cuts from the simulation in (a) at two different lateral locations relative to the tip, $x = 0$ is directly below the tip and $x = 2$ µm is beyond the edge of the tip. The magnetic field shown in the line cuts are projected on the NV axis while the full simulation shows the absolute value of the field.

4.4 2D MAGNETIC FIELD MEASUREMENT

The CFD is intended to apply a non-uniform field in the vicinity of the NV. To demonstrate this feature a spatial measurement of the magnetic field was performed in the vicinity of the NV. For this, the tip was set to a given tip extension which sets the distance between the tip to the diamond surface. At this height, the region around the NV was scanned, and at each point, the field induced by the CFD was measured with ODMR. Each pixel included first a Rabi measurement to determine the π time, followed by the ODMR measurement. Additionally, a contact measurement was done with the AFM in order to deduce the accurate distance to the surface resulting in a measurement of the surface topography (Fig. 4.9(c)). This measurement was performed at two

heights and the results are shown in Fig. 4.5. The maximum measured field is 259 μT, which does not hinder the NV contrast[32].

To compare to the simulation of the expected field (as shown in Fig. 3.5), we account for the degrees of freedom in the measurement. The first is the relative angle between the NV axis to the direction of the current, and the other being the lab coordinates along which the tip is scanned. The magnitude and range of the measured field are affected by the angle between the current to the NV, since the ODMR measurement is most sensitive to fields parallel to the NV axis. While the scanning axis defines the axis connecting the maxima and minima, it does not affect the field strength. The simulation, as shown in Fig. 4.5, projected along the NV axis $[\bar{1}11]$ and rotated by 45°, is qualitatively similar to the measurement. Several features are visible in both - a sharp peak in the field along with a broad yet shallow dip. As expected, the field strength increases with the distance to the surface. Quantitatively, the range and values of the field in the experiment and the simulation are in good agreement. The discrepancies can be associated with several uncertainties - the discreteness of the measurement, the error in the distance to the surface and simulation assumptions regarding the current flow along the wire. From the comparison, we can then calculate the magnetic field induced by the tip at the sample's position. This is important when considering the effect of the magnetic field on spins external to the diamond, such as unpaired electrons on the surface and more broadly a sample placed on the diamond, since by knowing the field generated by the gradient at each point, we can deduce what the Larmor frequency of the target spin would be.

4.5 Spin imaging resolution

To measure the magnetic gradient at higher resolution, we measure ODMR along a line connecting the minima to maxima regions, see Figs. 4.5c and 4.6(a). The magnetic field along the line scan is shown overlaid on the topography of the diamond pillar, showing the maximum gradient is near the center of the pillar, Fig.4.6(a). A line cut from the simulation is shown in Fig. 4.6(b) and depicts a similar trend and values to the measurement. This scan was repeated as a function of distance to the diamond surface, Fig 4.6(c). From each line scan the gradient is calculated as the slope of a linear fit between the two circular points marked for each line. As expected, the gradient increases as the tip is closer to the diamond surface, see Fig. 4.6(d). Following the law of Biot-Savart (see Eq. 3.2), we fit the increasing gradient to an inverse quadratic function. To obtain the maximal gradient the scan should be performed along the optimal x,y curve, where deviations from this curve will result in a sub-optimal gradient as seen in the point closest to the surface (Fig. 4.6(d)). For a current of 1.54 mA through the tip, the maximum measured gradient is 0.95 μT/nm, measured when scanning the tip along the axis connecting the minima to maxima regions.

The CFD is intended for nanoMRI and as such the imaging resolution achievable with the device is examined. The limit on resolution is a combination of the spectral resolution of the setup and the gradient achieved by the tip. With the single NV's dephasing time (T_2^*) of ~ 3 μs, we were able to measure ODMR within an error of 100 kHz. The signal from an electron is detected by the NV at the electron resonance frequency at $\gamma_e B$, where $\gamma_e = 28$ MHz/mT and B is the magnetic field

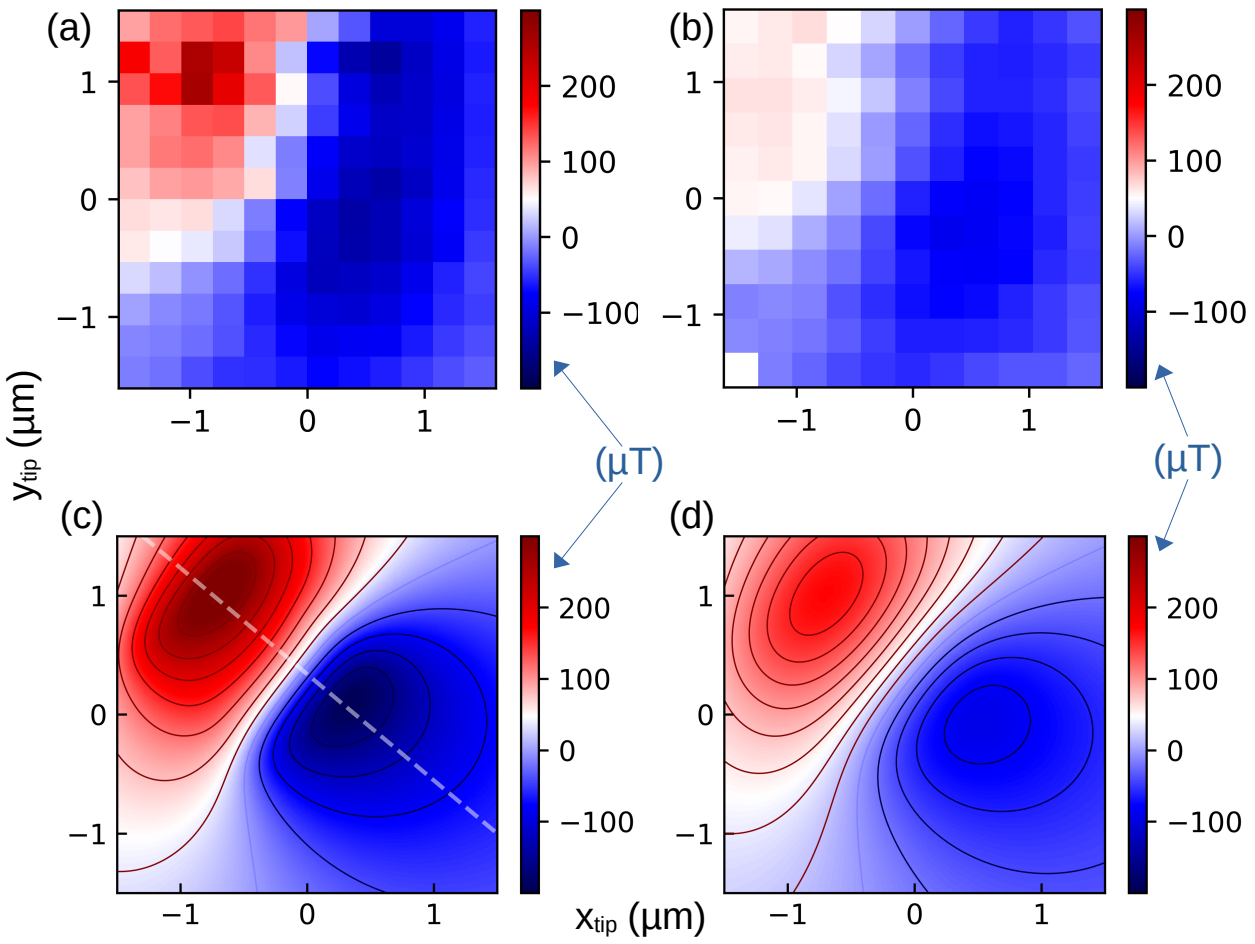

Figure 4.5: 2D Magnetic field generated by the tip. (a-b) A map of the magnetic field (in μT) of the tip measured by the pulsed tip ODMR sequence from Fig. 4.1c at varying distances (300 nm, 600 nm) from the diamond surface. (c-d) Numerical calculation of the expected magnetic field (in μT) projected on the NV $[\bar{1}11]$ axis for the conditions measured in (a-b), respectively. The white dashed line in (c) goes along a cross-section of the maximal gradient.

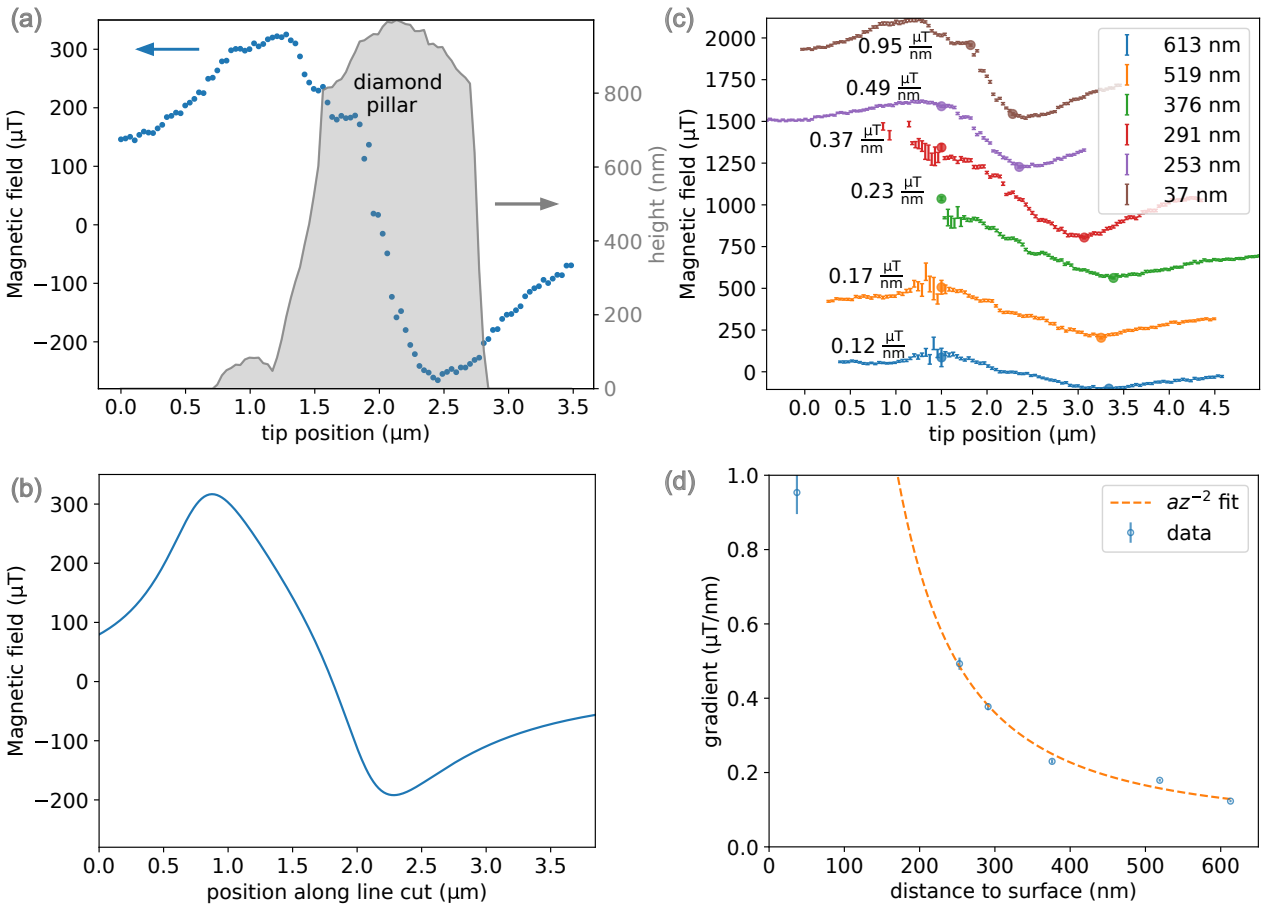

Figure 4.6: Magnetic field gradient. (a) A line scan across the magnetic field map over the region with the highest expected gradient (0.95 μT/nm) from (c). The gray region shows the diamond nanopillar topography measurement to show the location of the steepest slope with respect to the nanopillar position. (b) A plot of the line-cut from the simulation in Fig. 4.5c, in agreement with (a). (c) Line scans measured at varying distances from the diamond surface. For each line scan, the gradient is calculated along the two circular points. (d) The extracted gradient from (c) as a function of the distance from the surface with a linear fit.

applied to the electron. Thus, to distinguish electrons in our system the magnetic field separation is $\Delta B = 3.6\,\mu\text{T}$. With the gradient measured with a current of 1.54 mA this results in a 3.6 nm resolution for imaging electrons.

4.6 Increasing current

The measurements were performed at a relatively low current of 1.54 mA in order to minimize over heating of the device. A destructive measurement was performed where ODMR was measured at increasing current, Fig 4.7. When working with higher currents a longer wait time was set between consecutive ODMR repetitions and was set to 80 μs with the current on time set to 1 μs. This was added due to apparent shifts in the measurements when working with higher currents, and was noticeable when measuring the AFM extension at contact (equivalent to the distance between the tip to the surface) that detected a shift in the location of the tip, presumably due to heating. First, ODMR at a single point was measured for increasing currents under 10 mA, since according to the heating simulation (Sec. 3.1.1) such currents are safe. The measurement shows a linear increase in the magnetic field, this is expected from the linear dependence on current in Biot Savart (Eq. 3.2).

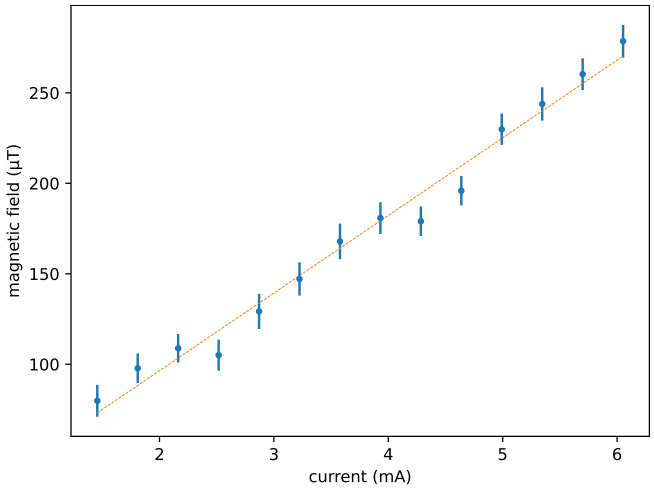

Figure 4.7: Measurement of magnetic field done at a single point as a function of increased current.

In order to measure the magnetic field gradient, line scans were performed also at increased current, and are shown in Fig. 4.8(left). The line scans show a similar trace with gradually increasing slope. The gradient was calculated from the slope of each curve. A second series of line scans was performed at currents up to 15 mA (see Appendix C.3) that showed the tip failed at a current of 14.2 mA after two ODMR measurements. The gradient at higher currents was also calculated and the combined measurements are shown in Fig. 4.8(right). The figure shows a change in the trend of the gradient that is associated with the two different batches of line scans, indicating there was a shift in the points scanned along the line between the two series. Using the highest current a gradient of 3.7 μT/nm was achieved. Although this is the highest gradient measured it is not the highest gradient that can be achieved with the CFD. Both the simulations and the measurements demonstrate that the maximal gradient must be measured at the optimal lateral location. Additionally there is a linear dependence between the current and the gradient. Thus the maximum current that can be achieved is calculated from the gradient measured at 1.54 mA scaled to the maximum current measured, i.e 13.4 mA, $(\partial B/\partial x)_{max} = \frac{I_{max}}{I_{low}} \cdot (\partial B/\partial x)_{I_{low}} = \frac{13.4}{1.54} \cdot 0.95 \frac{\mu T}{nm} = 8.27 \frac{\mu T}{nm}$. This gradient is above the required $3.6 \frac{\mu T}{nm}$ required for electron imaging and making it practical for nanometer resolution imaging.

In fact, the low-current $\sim$ 1 μT/nm gradient can already distinguish between spin labels, for example, spaced 4.8 nm in a molecular ruler[122], with a Larmor precession frequency difference between them of 134 kHz, as mentioned above, our gradients can be as high as 8.3 μT/nm. Additional improvement can be achieved by combining the gradient field with protocols that have demonstrated resolution as good as $\sim$ 1 Å[123,35]. Alternatively, the tip itself can be optimized further to improve both geometry and heat load, which may provide a better magnetic gradient.

4.7 Tip-induced Rabi power modulation

The geometry used here, i.e., where a metallic tip is placed above the diamond while a metallic microwave waveguide is placed below it, is shown to affect the NV Rabi period dramatically. We

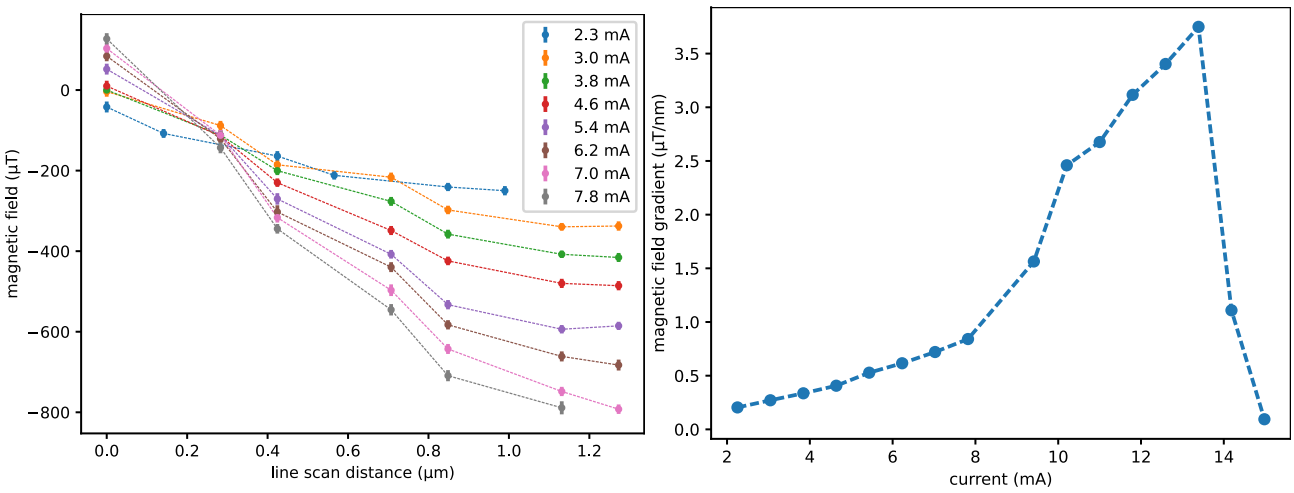

Figure 4.8: Magnetic field and gradient as a function of current (left) Magnetic field along a line scan where the maximum current is expected, scans are performed at increasing current. (right) The magnetic field gradient measured as a function of increasing current. The gradient was calculated from the line scan.

observe that by a proper positioning of the metallic tip, the Rabi oscillations' frequency (Ω, the Rabi driving power) can be increased for a set MW power applied to the waveguide. Fig. 4.9 shows two sets of measurements demonstrating this effect. First, we scan the distance to the diamond surface for a set lateral position and show a relative, $\sim$3.5-fold increase in Rabi power (Fig. 4.9a). Next, Fig. 4.9(b) shows a lateral scan where the tip is set to a distance of 156 nm from the surface, and we plot the ratio between the measured Rabi power, Ω, and the Rabi power when the tip is far-away from the NV, Ω_0. Here, there are three noticeable regions - (1) the far-field where the Rabi power is unaffected and equal to the baseline Rabi power as measured without a tip; (2) an enhanced region where the Rabi power increases relative to the baseline, and; (3) a third region where the Rabi power is significantly weaker relative to the baseline.

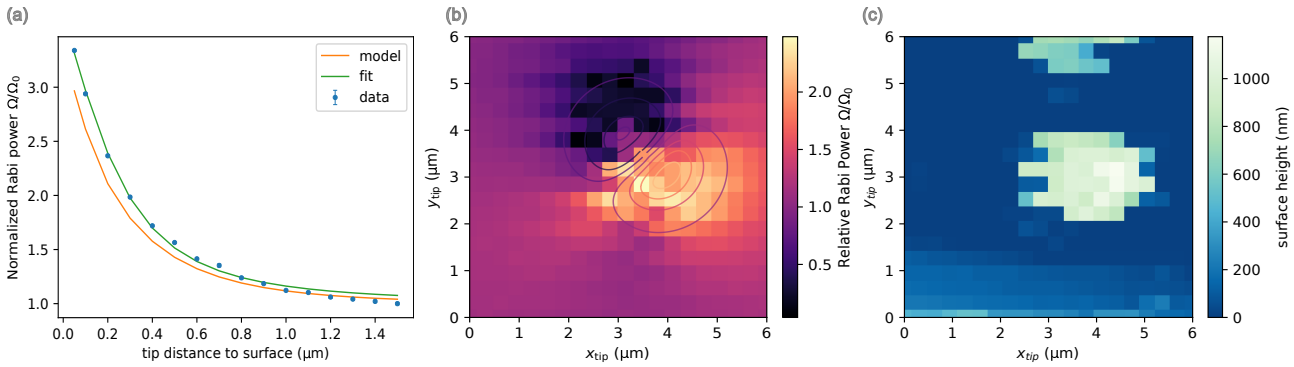

Figure 4.9: Tip-induced Rabi power modulation. (a) Normalized Rabi power (Ω/Ω_0) measured for a specific lateral tip position while varying the vertical distance to the surface. Each Rabi measurement is fit to $Ae^{-\beta t}\cos(2\pi\nu t)$ which gives the Rabi period and errors in the plot. Our model (orange curve) shows a similar behavior, with a slight deviation for the closest points. (b) Rabi power as a function of the tip's position relative to the position of the NV, divided by the Rabi power when the tip is far-away from the NV (Ω/Ω_0), while the distance to the diamond is set to be 156 nm. (c) A simultaneous AFM scan of the diamond surface where Rabi oscillations were measured. The two raised regions are the nanopillar shape etched in the diamond. The NV used for the measurements is in the lower pillar.

The observed modulation of the Rabi power is due to the metallic tip modulating the magne-

tostatic near-fields that interact with the NV center. Since these are near-field interactions, the modulation's strength is very sensitive to the tip's position. A detailed analytical model, representing the tip geometry using oblate ellipsoids is given in Appendix D. The contours in Fig. 4.9(b) are iso-power lines calculated according to the model, and are in agreement with the experimental data. Our model also qualitatively captures the vertical distance dependence (orange line in Fig. 4.9(a)). When simplifying each ellipsoid to a single point dipole, the data can be fit by a $z/(z^2+d^2)^{1/2}$ behavior (green curve in Fig. 4.9(a)), where z is the tip's vertical distance from the NV and d is the lateral one.

The Rabi power modulation is important in several aspects, as working with a larger Rabi frequency provides shorter pulses necessary for more accurate dynamical decoupling sequences[73]. Using the tip as a method of increasing the Rabi power, one does not need to "pay the price" of thermal management due to increased MW power. When working with the tip, this is particularly valuable since the MW heating can shift the sample when working with strong power.

These measurements were performed without running current through the tip and are independent of the induced magnetic field. The Rabi power gradient itself, without a current through the tip, can serve as a tool to image spins, since such a large difference in Rabi powers will make it possible to address spins only in a specific region (of the same Rabi power).

4.8 Discussion

We introduced a magnetic-field gradient on an AFM tip, which can be pulsed with rise/fall times shorter than 600 ns. This is achieved using a three-step self-aligning deposition process, effectively creating a focused current at the apex of the tip. Using an NV center as a local magnetic sensor, we demonstrated gradients as strong as $1\,\mu\mathrm{T\,nm^{-1}}$, which can be even further increased eight-fold with a stronger current. Our proof-of-principle of the gradient enables, already now, nanoscale magnetic resonance imaging of proximate unpaired electrons spins in, e.g., a molecular ruler. Moreover, this metallic tip can also serve as a means to locally modulate the driving field around both the target and sensor (NV) spin, yielding an enhancement of $\times 3.5$ in the spin's Rabi driving power. The spatial variability of the Rabi power is and of itself a gradient source for future magnetic resonance imaging in nanometer length scales. The geometry of the tip (apex shape and diameter), as well as a choice of deposited metal and the substrate material itself, can all be further optimized for an overall higher gradient. Specifically, when working at cryogenic temperatures, a superconducting material can support larger current densities[124] (and no Joule heating), the tip's quartz substrate can be replaced with sapphire or diamond for better heat dissipation[125], and optimization of the apex geometry while taking into account Joule heating can yield higher magnetic field gradients in proximity to the tip.

The current focusing device offers several advantages, overcoming the limitations of existing nanoMRI techniques. First, the ability to pulse the current allows for different magnetic fields during spin manipulation, readout, and initialization, providing optimal NV contrast as defined by the diamond lattice eigenstates. Second, the magnetic field induced by the tip is small relative to the external field and the zero-field splitting, meaning only minor shifts are expected, and so

the effective Zeeman energy remains largely unchanged when switching between measurements with and without the field from the tip. The possibility to co-align the tip with an arbitrary NV also holds advantages to sensing when working with single NVs. With the geometry presented here, a sample can be placed on the diamond surface in a statistical manner, and once an optimal NV is identified, the gradient can be applied locally around the specific NV, targeting spins and creating a spectral separation between them in Larmor frequency, in the NV's immediate vicinity. Additionally, the current source can also reverse the direction of the magnetic field, enabling the application of gradient pulse sequences similar to those used in conventional NMR [126,127].

The tip combines two critical features for immediate application in nanoMRI, namely control over the temporal and spatial magnetic field. By working at the upper current limit, we can achieve the gradient necessary for nanoscale imaging. The device thus overcomes the limitations of alternative methods, enabling high-contrast spin read-out with an arbitrary choice of the working NV and of sample placement. Going beyond nanoMRI, we envision our scannable tip with a switchable local magnetic field gradient as a useful tool in active and passive characterization of materials, e.g., (anti)ferromagnets, superconductors and more exotic magnetic phases of matter.

5

Surface magnetic spectroscopy

All knowledge of reality starts from
experience and ends with it

Albert Einstein
On the method of theoretical physics

The ability to use magnetic resonance detection to surfaces at the nanoscale offers new opportunities in surface science such as self-assembled monolayers (SAMs) which play a central role across a wide range of fields, from energy storage[128] to medical devices[129,130]. NV-based magnetometry provides a unique tool for probing magnetic properties, both coherent and fluctuating fields, at the molecular level with high spatial resolution and sensitivity, as discussed in Sec. 1. Conventional magnetic resonance does not detect at nanoscale layer resolution, and alternative surface techniques[131] do not detect the magnetic signal of the sample. However, realizing this potential requires addressing two fundamental challenges: (1) forming the monolayer sufficiently close to the NV center, as magnetic signals decay with distance (Eq. 3.2) as does the dipole-dipole interaction (Eq. 2.13), and (2) identifying and interpreting the magnetic signals originating from the sample.

In this chapter, I investigate several chemical approaches for forming well-ordered SAMs in the vicinity of the diamond surface. These methods aim to produce a uniform monolayer with a stable chemical attachment to the substrate. Following this, two experimental studies are presented. The first aims to detect electron spins bound to the monolayer, with the long term goal of characterizing local surface properties such as spin density, layer thickness, and molecular uniformity. The second study investigates the CISS effect, introduced in Sec. 1.3, by forming a chiral monolayer on the

diamond and attempting to detect magnetic fluctuations associated with the molecular adsorption on the surface. This phenomenon arises in SAMs of chiral molecules that consist of a monolayer of molecules adsorbed onto a surface, with uniform orientation. Detecting CISS using NV centers offers a unique approach to probing surface interactions at the nanoscale.

Together, these efforts contribute to the advancement of surface-sensitive magnetic resonance at the nanoscale, while also highlighting the experimental challenges that remain in bringing such techniques to maturity.

This chapter has three parts. First, in Sec.5.1, I will present the different techniques attempted for SAM preparation, and then, I will discuss the measurements done on two samples, a spin radical SAM in Sec. 5.2 and a SAM of chiral molecules in Sec. 5.3.

5.1 Surface methods

To study magnetic resonance of surface samples one needs to create the SAM in the vicinity of the diamond, as mentioned, the signal decays with distance. This can be done either directly on the diamond or using a scanning tip configuration. It is possible to adhere the molecules directly to the diamond surface yet it is chemically challenging (see Sec. 1.2), and so there is motivation to explore alternative methods. In the following section several methods for surface sample preparation on diamond are presented. The focus on the CISS effect motivated the choice for the peptides used to form the monolayer in most of the methods.

5.1.1 Adhering to a metallic surface

A common method[132] to create a SAM uses a gold surface which creates a bond with the thiol (sulfur group) at the end of the molecule that forms the monolayer surface. I attempted this on the diamond by depositing a thin layer of gold on the diamond and preparing the SAM on this layer. A recent study[133] examined the effect of copper deposition on the properties of the NV centers and showed that for deep NVs (>10 nm) in an ensemble the properties are good for sensing and that adding a buffer layer of Al_2O_3 improves stability.

To create the metal layer E-beam deposition was used to deposit 2 nm Ti followed by 6 nm Au on the diamond. The surface was then cleaned with ethanol, acetone and UV-ozone cleaning prior to incubating the sample overnight in a solution with chiral peptides containing a thiol tail, ((Ala-Aib)$_7$-MPA), to create the SAM[52]. XPS measurements confirmed the formation of the peptide layer on the diamond and measured the thickness of the organic layer to be 2.9-3.3 nm.

Two challenges were met when attempting to detect the NVs with the gold-coated diamond in the confocal microscope. First, the gold created very high background fluorescence, such that it was challenging to see the NVs above the background. Second, and more importantly, the NVs were quenched (i.e., transitioned from NV^- to NV^0), and could not be detected in the confocal microscope or in correlation measurements and the NV can no longer be used as a quantum sensor. This is possibly due to the broadband structure of gold's optical spectrum[134,135]. An attempt to mitigate this effect was done by adding an insulating buffer layer of SiO2 with ALD. This was tested with different thicknesses - 2 nm, 5 nm and 8 nm followed by 2 nm Ti and 6 nm Au. In

these samples NVs were detected yet there were fewer NVs than in the bare sample. I hypothesize that the NVs that were found to exist were relatively deep in the lattice, and so the metal layer less affected them. Thus, there is a catch-22: NVs must be a few nanometers below the surface to sense molecules, yet the NVs that are close to the surface are quenched. For this reason, other methods were attempted.

5.1.2 SAM on oxide

Here, I demonstrate the formation of a monolayer bonded to a thin layer of SiO_2 oxide on the diamond. This method opens the door to well-established chemical processes for monolayer formation [136] on glass-like surfaces. Unlike direct bonding to the diamond, silane chemistry [137,138,139,140] is robust and used across biology and chemistry for vast research questions [141,128,136]. As a proof of concept for single NV sensing, we attempt to detect the free electron from a spin label attached to a monolayer on the SiO_2 layer on the diamond.

To this end, we prepared a SAM with a spin label on a 2 nm SiO_2 layer deposited on the diamond surface. First, atomic layer deposition (ALD) is used to create a 2 nm SiO_2 layer. Silane chemistry is well established for creating a monolayer on this surface, using APTES ((3-Aminopropyl)triethoxysilane) where $SiOCH_3$ bonds to the surface [136] and, under correct conditions, forms a monolayer. This creates an amine (NH_2) tail which is available to react with the sample molecule. The free radical is introduced in the form of a spin label which has an NHS ester on one side. The NHS ester interacts with the amine on the surface, leaves the molecule, and allows the radical portion to bond to the surface, see Fig. 5.1. Measurements on this sample and the full details of the process are presented below in Sec. 5.2. During the process of this study a similar work [142] was published which examines

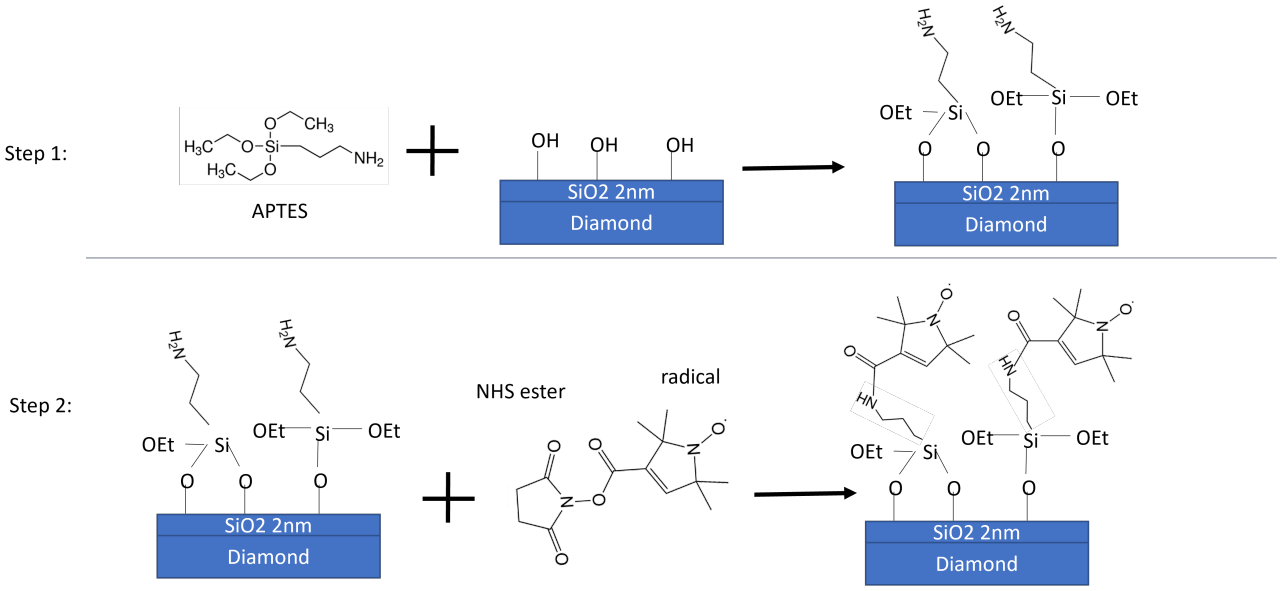

Figure 5.1: Chemical process for attaching the spin label radical to the diamond surface. First, ALD is used to apply a 2 nm layer of SiO_2 on the diamond. Then, in step one a monolayer is created on the surface using APTES. This creates an amine layer on the surface which is available for molecular bonding. The radical is then attached via NHS-ester amine chemistry, leaving the radical attached to the diamond surface.

the NV coherence under the effect of immobilization of biomolecules on Al_2O_3 on diamond and similarly using APTES to link a desired molecule.

5.1.3 Bonding the phosphorus tail to Al_2O_3

In order to study chiral molecules, one can use an alternative method instead of thiol bonding to gold, namely, a phosphorus tail that bonds to Al_2O_3; this similarly forms a monolayer. This method was similarly used by Liu et al.[45] where an ensemble of NVs are used to detect the NMR signal from a monolayer. The main caveat in this route is the need to specifically synthesize the desired molecule thus the technique may be less robust. With this method ALD is used to create a thin alumina oxide layer on the surface and the molecule is bonded covalently to this layer[143]. This technique was implemented using chiral molecules that form a SAM and the measurements done with the NV are presented in the section that follows (Ch. 5.3). The effect of alumina on the diamond surface was studied by Henshaw et al.[133] and Kumar et al.[144]. The first work showed that relaxation time T_1 and coherence time T_2 are mostly unchanged due to alumina deposition. The second examined the charge state stability under alumina deposition and concluded that the deposition improved the stability and reduced degradation that is associated with laser illumination.

5.1.4 Molecules on the tip

An alternative to placing molecules on the surface is to leverage the gold-coated tip and the AFM, which is incorporated in the NV setup. This has the advantage that it is simple to conduct an experiment along with a control experiment. When placing a sample directly on the diamond, one needs to consider the noise from the diamond surface itself. The surface of the diamond is a source of noise[44], and it is modified during surface treatments, which are employed when placing and removing a sample from the diamond. Change in the noise can mask a measured effect and care is taken to avoid artifacts. Placing a sample on a tip overcomes this challenge as one can measure with the tip in the vicinity of the NV and then repeat the measurement[120] with the tip retracted from the surface without modifying the diamond. The tip developed in this work is coated with a gold layer that can be used to create a SAM leveraging the thiol bond as mentioned above (Sec. 5.1.1). A process for creating a SAM on the tip was attempted and studied with AFM but was not utilized for sensing. A gold-coated tip was incubated in a peptide solution ($(Ala\text{-}Aib)_7$-MPA in tri-F-OH, 1 mg/ml) overnight. After removing the tip from the peptide solution, it was washed in solvents to remove residues. The surface of the tip was examined with AFM and a scratch test was done to test the layer thickness. The measurements showed a molecular layer was formed on the tip with a thickness of $\sim$ 5 nm. At this time, an attempt to measure the sample on a tip with the NV has not been done yet. Nevertheless, given the success of incorporating the tip in the NV setup and, specifically, the ability to align the tip to a working NV makes this technique possible for future research.

5.1.5 Discussion

Here I presented several methods to bond molecules to the diamond surface. The two methods using a thin intermediate oxide layer deposited on the diamond stand out as being practical and robust. Both are conceptually similar in that they avoid direct formation of the monolayer on the diamond and leverage existing methods for SAM formation. Using Al_2O_3 utilizes a phosphorus tail in the bonded molecule and may require specific synthesis yet the monolayer process is straight forward and robust. Using SiO_2 as the oxide layer required an additional surface process, the APTES layer which acts as an adapter the desired molecule which has a tail which can bond to amine. Once the SAM formation is established the second challenge remaining is the detection by the NV and specifically by a single NV giving local nanoscale sensing capabilities.

5.2 Measurements on electron radicals

Measuring magnetic resonance signals from a monolayer with nanoscale resolution can provide a useful tool for fundamental research. However, as discussed in Sec. 1.2, combining monolayer formation with single-NV measurements presents unique challenges. First, the monolayer must be formed robustly—with high surface coverage and covalent bonding to the surface, resulting in a monolayer where the molecules are aligned. This is accomplished here by following the silane method discussed above (Sec. 5.1.2) and introducing a SiO_2 bonding layer. The second stage is detecting the magnetic resonance signal from the sample to demonstrate the validity of the detection. This requires overcoming obstacles such as the added distance between the NV and the monolayer and detecting the signal above the background magnetic noise that is native to the diamond.

As a proof of concept towards sensing the magnetic signal from a monolayer using a single NV, we demonstrate the formation of a monolayer on SiO_2, to which a free radical is covalently attached. This radical is a free electron which is expected to couple to the NV with the dipole-dipole interaction, Eq. 2.13. Such free radicals can be used as spin labels in future work to mark specific molecular sites and study molecular dimensions and configuration. Studying this spin-labeled monolayer with ESR techniques will allow us to probe the structure and configuration of molecular surfaces. The method and results are presented in the following sections.

5.2.1 Background

Measuring the signal of the spin-labeled SAM is done by detecting the signal from the free electron, i.e. the radical, in the molecule. The pulse sequences used are DEER and DEER-τ where an MW pulse is applied to the auxiliary electron spin, see Sec. 2.2.1. In the DEER signal, the frequency of the pulse to the electron is swept, and a dip in the NV contrast is expected if there is an electron in the NV environment. This measurement confirms the existence of an electron spin that is within the detection volume of the NV. In a DEER-τ measurement the frequency of the MW pulse to the auxiliary spin is constant and the pulse length is swept, driving the auxiliary spin. For the DEER-τ signal, a stretched exponential decay $f(t) = Ae^{-(t/\tau)^\beta}$ is expected on top of the decay of the Hahn echo (as discussed in Ch. 2.2.1). Several works[34,36] pointed to the importance of the exponent

of the decay highlighting that spin populations with different statistical properties are expected to have a different power law[90]. For a normally distributed 2D density of spins, the exponent is expected[36] to be $\beta = 2$. For these statistics, the density of the detected spins can be deduced from the decay rate.

$$\tau^{-1} = \left(\frac{\mu_0}{4\pi}\right) \frac{\sqrt{3\pi\sigma}\gamma_e^2\hbar}{8d_{NV}^2} \tag{5.1}$$

Here σ is the density of the probed spins, γ_e is the gyromagnetic ratio, d_V^2 is the NV depth. To calculate the density the NV depth is needed, this can be experimentally measured by probing a material with a defined proton density. The evolution time in a Hahn echo or DEER-τ pulse sequence is equivalent also to the sensing radius, at longer times, larger radius is integrated and further spins are detected[36]. The spin radical layer is evidently placed further from the surface and this may affect its signal. In addition, it may have different statistical properties. I expect it to be bound to the APTES, yet it may have some motional freedom along the bonds. In contrast, the free electrons have been shown to have statistical properties that implies hopping from one site to the next[36]. These differences may be revealed in the decay rate (Eq. 5.1).

5.2.2 Sample preparation

A diamond membrane, from Element Six, with 5 keV implantation, polished and cut to the dimensions 2 mm × 2 mm × 30 µm is used for the experiments. First, the diamond is cleaned by boiling in a tri-acid solution (sulfuric acid, nitric acid and perchloric acid at a ratio of 1:1:1 heated to 150°C) overnight. This removes most residues from the diamond surface[36,34,105] and changes the chemical bonds at the surface[40,44]. For some samples, this was followed by oxygen annealing at 450°C for 4.5 hours, aimed to increase the oxygen surface termination and reduce trapped electronic states[44]. Next, atomic layer deposition (ALD) is used to prepare a 2 nm layer of SiO_2 on the diamond surface. The ALD is performed at 200°C, with 30 cycles. To create the silane layer, the sample is then placed in piranha solution (2:1 sulfuric acid and hydrogen peroxide) for 30 minutes for cleaning to achieve a hydroxyl saturated surface for better silane attachment[145]. The sample is then placed in a solution of APTES ((3-Aminopropyl)triethoxysilane) in anhydrous toluene (1:100), and left in a gentle shaker for one hour. Finally, the spin label is attached by placing the sample in a solution with 1-Oxyl-2,2,5,5-tetramethylpyrroline-3-carboxylate NHS ester (see Fig. 5.1) which bonds to the amine on the SiO_2 surface. To remove the radical, the sample was placed in HF for 10 minutes. This is intended to remove the SiO_2 layer along with the molecules. For final cleaning, the tri-acid boiling is repeated.

5.2.3 Confirming chemical process

The chemical process itself was developed as part of this work and as such we first confirmed the attachment of the spin label to the surface and the formation of the mono-layer. XPS measurements were performed on a diamond with the sample and on a diamond after cleaning to ensure the material was removed. XPS was performed twice with two different molecular samples attached to

	round 1	round 2
molecule attached	NHS ester radical	sulfo-SMCC
SiO_2 thickness (nm)	4.5	1.75
APTES plus molecule thickness (nm)	2.2	1.2

Table 5.1: XPS results confirming the chemical process to create the monolayer on the diamond surface. The process was performed twice with two different molecules attached to the APTES as noted in the table.

Sample	Average counts
Control	270
Test 1	1177
Test 2	1253

Table 5.2: Comparison of the fluorescence signal when chemically bonding the fluorescent molecule to the diamond vs. a sample without chemical bonding. The test sample is a diamond with SiO_2 deposition, followed by functionalization with APTES then incubated with the fluorescent molecules, giving the following layers Cy3B-PA63101/APTES/SiO_2/diamond. Two samples were prepared in a similar manner for statistical control. The control sample is a diamond with SiO_2 that was incubated with the fluorescent molecule, giving the layers Cy3B-PA63101/SiO_2/diamond.

the APTES layer. The thickness results vary between the two repetitions yet both confirm that the APTES layer was formed and that the molecule was attached to the APTES, see Table 5.1.

Additionally, confocal measurements were performed to test that the chemical process done resulted in the molecule bonding to the surface. A fluorescent molecule with an NHS tail (Cy3B - PA63101) was attached to a diamond with an APTES layer following a similar process to that described above. A control sample without APTES was prepared, where the sample was incubated with the fluorescent molecule and washed to test for physical adhesion. The photon counts were measured in a confocal microscope and were averaged in several areas in the sample and control, the sample showed ~4 times the number of counts relative to the control (see Table 5.2) indicating the fluorescent molecule attachment to the diamond with the APTES.

5.2.4 Electron radical sensing - results

After sample preparation, measurements are done to detect the spin radical, i.e., the free electron that is attached to the surface using the NV center. The measurements were repeated on the diamond also after it was cleaned. The signal from the spin label SAM is compared to a background signal from the bare diamond to test if the electron signal originates from electron spins native to the diamond or from the SAM.

The magnetic field is aligned to the NV and chosen such that the expected signal of a free electron, $f = \gamma_e B$, and the NV $f = D - \gamma_e B$ are well separated such that a pulse at the free electron peak is off-resonance for the NV spin. The frequencies are also chosen to be separated by less than 400 MHz such that the bandwidth of the AWG will include both signals. First, we examine a reference sample of a bare diamond, see Fig. 5.2. Ideally, this sample will not exhibit a dip at the free electron frequency in the DEER signal. However, the signal from the bare diamond showed two dips in the DEER signal, the free electron and the NV. This indicates that there is a free electron in the NV environment also without any sample on the diamond. The signal dip that is associated

with the electron frequency was also apparent after oxygen annealing, indicating that there are surface electrons on the bare diamond. These electrons must be considered when understanding the signal from the diamond with the radical attached to the surface. For this reason, we examine the DEER-τ signal from the sample with the radical and see if there is a difference in the decay rate with and without the added radical sample.

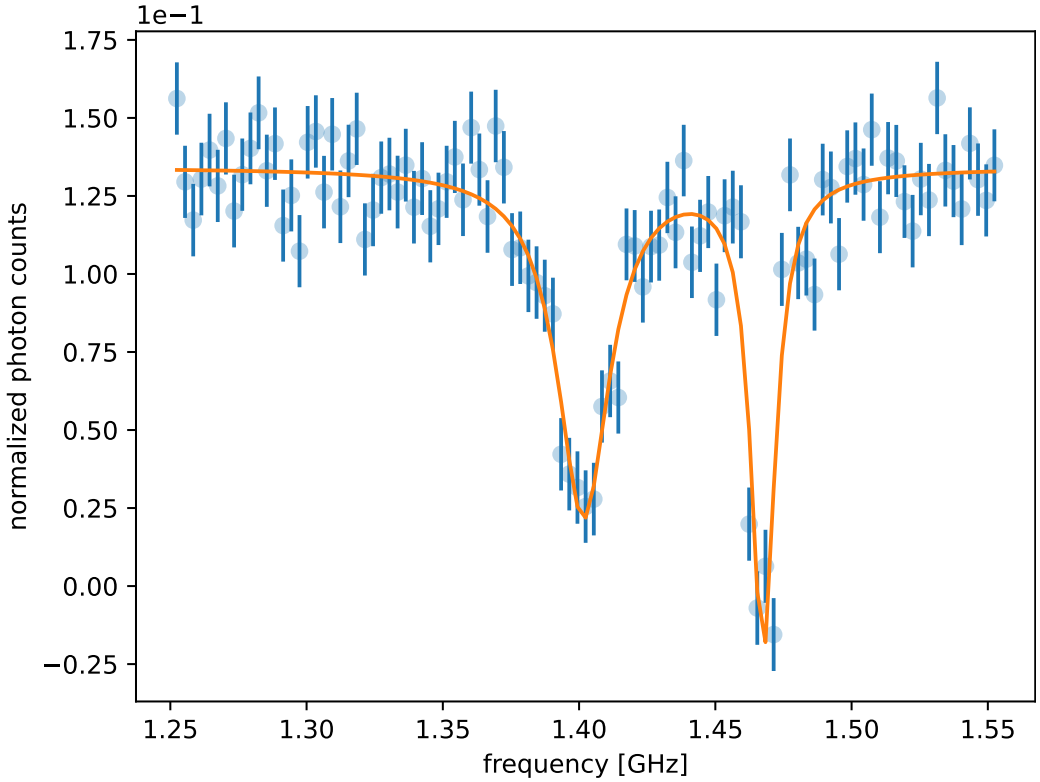

Figure 5.2: Signal from a bare diamond after tri-acid boiling and oxygen annealing when applying a DEER pulse sequence that sweeps the frequency of a pulse applied to the electron that is sensed. Two peaks are seen - one is associated with free electrons and the other with the NV.

The background decay of the DEER-τ is a hahn echo decoherence of the NV, this was measured for the sample with and without the spin labeled SAM. The results of one such NV are shown in Fig. 5.3(a) where it is seen that the decoherence is faster under the effect of the added SAM (orange curve). This is associated with magnetic noise from the added organic SAM and is not specific to the free electron in the SAM. The signal that is specific to the free electron is measured with the DEER-τ sequence which drives the electron with a resonance pulse. The effect of the electron decay is expected to add an additional decay or oscillation on top of the general Hahn echo decay[34]. The results for such a DEER-τ pulse measured at one NV are shown in Fig. 5.3(b). The measurement shown a change in the decay rate yet oscillations are not observed. Moreover the change seen in the Hahn-echo can explain the change in decay time seen in the DEER-τ measurement meaning the change is not necessarily due to the electron in the SAM. This was repeated for ten NVs that were sampled, the results showing the decay time for each NV for both the Hahn echo and the DEER-τ sequence are summarized in Fig. 5.4. Each curve is fit to a decay $y(t) = Ae^{-(t/\tau)^{\beta}}$, where τ is the decay rate and β is the stretched exponent factor. Examining the decay rates, there are some NVs with no change, while others show a decreased decay rate.

5.2.5 Discussion

In this study, we anticipated that the NV signal would be influenced by the presence of free electrons associated with the spin labels in the SAM, ideally manifesting in the DEER-τ measurement as a characteristic oscillation superimposed on the general decay curve, as previously reported in similar contexts[34]. However, a complicating factor emerged: a background signal from surface-associated free electrons was observed even in the absence of the spin-labeled material. This background complicates the interpretation of the DEER-τ data.

In addition to this, the molecular layer itself appears to reduce the NV coherence time (T_2), making it difficult to attribute changes in the decay profile specifically to the electron spins of the spin label. It remains necessary to disentangle the various contributions to the DEER-τ signal—namely, those arising from surface-bound free electrons, the targeted radical spins, and nuclear spins associated with the molecular monolayer.

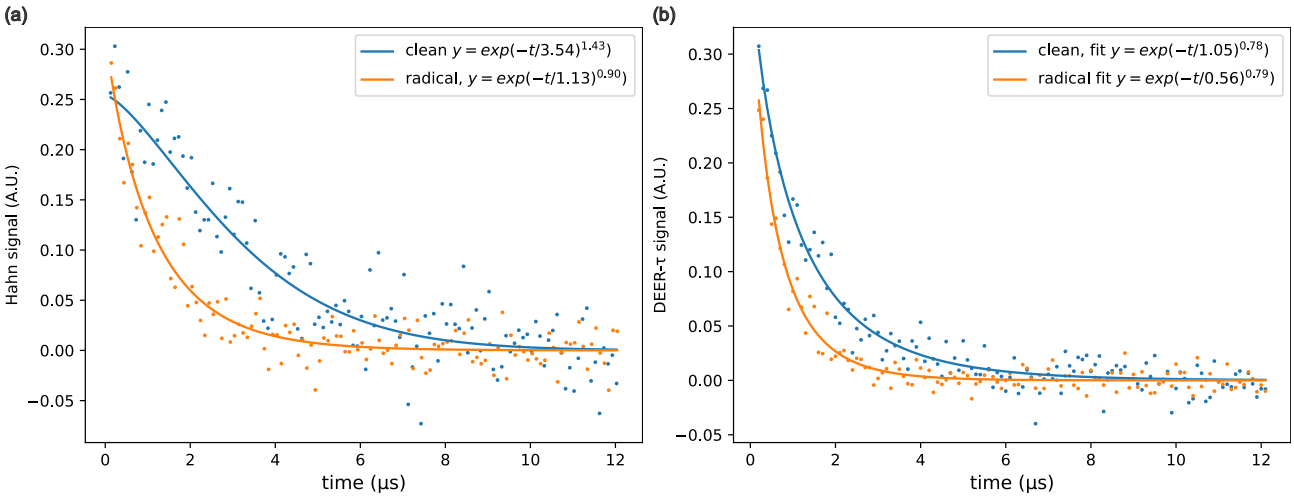

Figure 5.3: Comparing the signal from a single NV from the diamond without (labeled clean) and with the spin radical SAM sample. Two pulse sequences were applied: first (a) Hahn echo pulse sequence, followed by (b) "DEER-τ" pulse sequence.

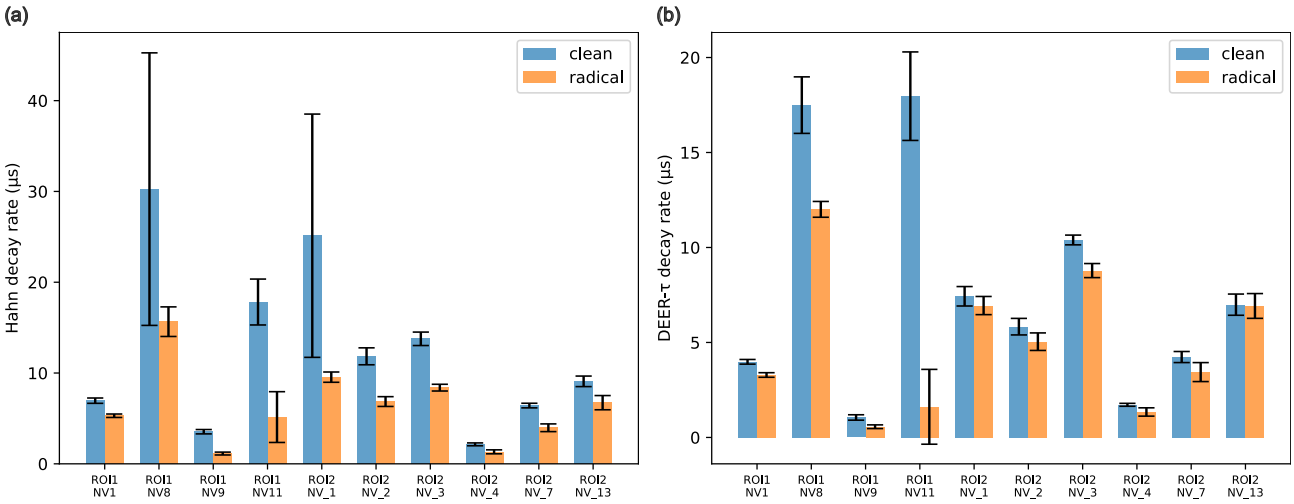

Figure 5.4: Hahn echo and DEER-τ pulse sequences were measured for a series of 10 NVs. Each curve was fit to an stretched decaying exponent and the decay rate was extracted from the fit. Comparing the decay rate of the NV with (labeled clean) and without the spin radical sample (labeled radical). (a) Hahn echo pulse sequence (b) DEER-τ pulse sequence.

While complementary techniques such as XPS and confocal imaging confirm that the surface functionalization was successful and that spin-labeled molecules were deposited on the diamond, the specific magnetic resonance signal from the radical spin label remains unresolved. The DEER measurements did not reveal a clear difference between the bare diamond surface and the functionalized surface, leaving the initial challenge of measuring surface-bound electron spins unresolved.

We believe that isolating and removing the contribution of surface charges is critical to enabling the detection of spin labels via NV sensing. One potential approach involves improving the oxygen annealing, which has been shown to reduce surface charge densities. Preliminary results in this direction are encouraging, though further work is required to confirm their effectiveness and reliability.

5.3 Measurements on chiral SAM

Investigating the magnetic signature of the Chiral-Induced Spin Selectivity (CISS) effect using NV-based sensing is of interest in the effort to understand the nature of CISS[47,55,146]. The CISS effect, which links molecular chirality with spin-dependent transport and magnetic behavior, has been extensively studied in systems involving current flow (photoemission[49] and molecular junctions[50]) and magnetic substrates[51] (see Ch. 1.3). However, the possibility of detecting CISS-related magnetic fluctuations in the absence of these external stimuli remains less studied. NV centers, particularly near-surface single NVs, offer excellent sensitivity to local magnetic fields and are well-suited for probing surface-level interactions at the nanoscale. Here, I aim to measure the magnetic fluctuations that arise due to the adsorption of chiral molecules directly on the oxide surface above the diamond. This is done without an intermediate magnetic material and without applying current to the molecules, thereby enabling a minimally invasive and purely passive sensing approach. The detected signal, i.e., magnetic noise fluctuations, also differs from the standard CISS detection and as such can lead to new insight regarding the effect. The measurements done on chiral molecules that form an SAM, along with the method details, are presented below.

5.3.1 Sample preparation

The diamond sample used was purchased from *QZabre AG*, with single NVs randomly distributed in a pillar array, the implantation energy is 5 keV, resulting in an implantation depth of 8 ± 3 nm. The diamond was purchased after it is etched to have a pillar array to enhance photon collection[147]. A 2 nm layer of Al_2O_3 is deposited on the diamond using ALD, 20 cycles at 180° C with trimethylaluminium (TMA) used as the precursor. The chiral molecule used to form a SAM is $(Ala)_4$-(Lys-$(Ala)_4)_4$-Lys-Ala-(Mini-peg)-Ser(OPO_3H) at a concentration of 1 mM in a 1:1 solution of acetonitrile and water. The diamond was incubated in the solution for 60 hours and finally washed in acetonitrile and water 1:1 solution. It was then placed in the NV confocal setup in a helium exchange gas environment. After measuring, the sample was cleaned to remove the alumina along with the molecular layer. For cleaning the sample was placed in 5% NaOH solution in methanol for 60 hours, and finally washed in methanol. XPS measurements, see Table 5.3, confirmed the for-

Layer	region 1	region 2
Al_2O_3 thickness (nm)	1.46	2.3
Organic monolayer thickness (nm)	2.1	2.45

Table 5.3: XPS measurement done on a sample consisting of a silicon wafer base with 2 nm ALD deposition of Al_2O_3 with chiral monolayer ($(Ala)_4$-(Lys-$(Ala)_4)_4$-Lys-Ala-(Mini-peg)-Ser(OPO_3H)). The thickness of the alumina and the organic monolayer were calculated using the XPS data. This confirms the formation of the monolayer and is a measure for the layer thickness.

mation of the SAM on the diamond, the XPS was performed on a sample prepared on a diamond without implantation and etching.

5.3.2 Noise spectroscopy measurement on chiral SAM

Noise spectroscopy was performed using the T_1 and T_2 pulse sequences (Ch. 2.2.1), each was measured at three different magnetic fields (roughly 120 G, 290 G, 475 G, slightly differs for different NVs) that were aligned to the NV axis. At each field the measurement was done for both transition frequencies, $|0\rangle$ to $|-1\rangle$ and $|0\rangle$ to $|1\rangle$. For T_1 relaxation, the filter function depends on the transition resonance frequency (see Ch. 2.2.1), as such the two transitions may give different results. For T_2, the signal filter function is independent of the Larmor frequency (see Ch. 2.2.1) and is expected to be similar for both transitions. To observe the effect of the chiral sample a reference measurement was done on the sample before forming the SAM. First, the diamond with Al_2O_3 was measured, then the SAM was bonded to the surface and NV measurements were repeated with the chiral SAM. The signal was measured for several NVs since it is expected that the results will differ from one to the other depending on the depth of the NV, the noise around the specific NV and possibly the uniformity of the molecular layer.

The measurement shown in Fig. 5.5 shows a consistent decrease in T_1 under the effect of the SAM. This decrease was seen for several NVs, yet not for all (Fig. C.5). The NV used in Fig. 5.5 showed a decrease in T_2 at 500 G yet this was not observed broadly and so is inconclusive. The consistent difference in relaxation time, T_1, indicates that there are fluctuations in the magnetic field in the frequency range of the Larmor frequency ($\sim 1 - 4$ GHz), and these fluctuations are related to the chiral sample on the surface. Interestingly, the chiral molecules are not magnetic [148], although they display magnetic like properties [47], and there is no additional magnetic material on the sample [53]. Albeit this, the molecules at the surface cause magnetic fluctuations detected by the NV. This measurement is a different way to observe CISS compared to standard transport measurements and as such can give new insight as to the CISS phenomena.

5.3.3 Discussion

The interaction can be described within two conceptual frameworks: direct and indirect interactions. A direct interaction requires the presence of a term in the NV center's Hamiltonian that is influenced by the chiral molecule. This can occur if the molecule exhibits magnetic properties, either static or fluctuating, that directly couple to the NV. Alternatively, an indirect interaction may arise if the chiral molecule affects nearby spins, which in turn interact with the NV center.

As discussed in Chapter 5.2, the NV is known to couple to proximal surface electron spins, which may themselves be influenced by the chiral molecule. This mechanism is expected to occur due to Chiral-Induced Spin Selectivity (CISS) and may provide insight into the observed effects. The effect of CISS by adsorption of chiral molecules on a ferromagnetic surface has been shown to induce magnetization[51]. Here, it is particularly interesting that the surface interaction is between the chiral molecule and an oxide, as opposed to a ferromagnet or a metal which was suggested to be involved in the CISS interface mechanism[64]. Additionally, there is no current or voltage applied to the molecules which could mediate the molecule to surface interaction. Given the open questions regarding the underlying mechanism of CISS observing the phenomena under different conditions can lead to new theoretical insight. A conceptually similar measurement was done with NV centers where a surface interaction was shown with graphene on the diamond surface[149]. There, it is suggested that the interaction is mediated by surface electrons which interact with the graphene, and it is these electrons that the NVs sense with the coherence measurement.

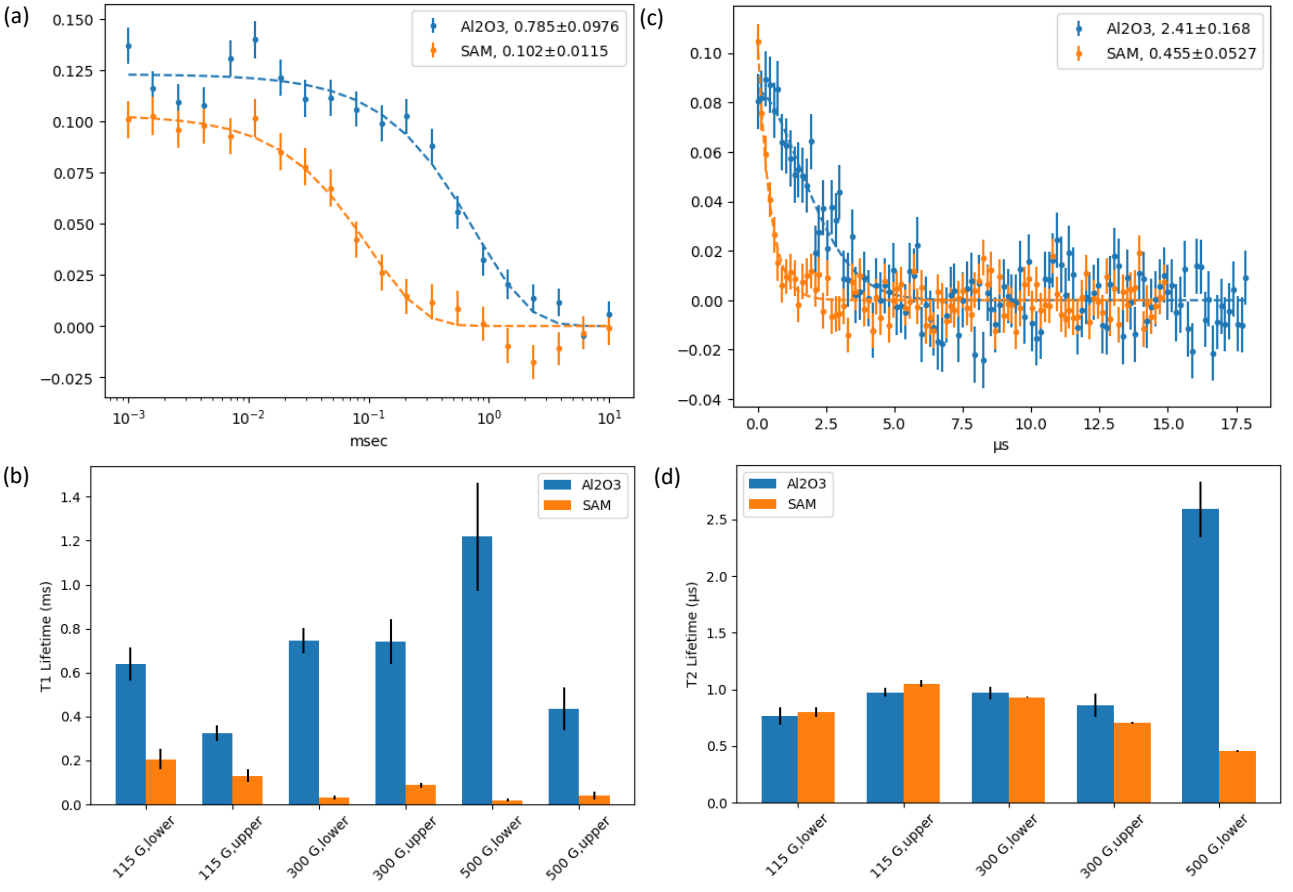

Figure 5.5: Relaxation measurements using the pulse sequence for T_1 and T_2 are shown for an NV where the effect of the SAM is apparent for T_1. (a) An example of a single trace from a T_1 measurement, the decay rate with the SAM is shorter. (b) Combined T_1 data measured on a single NV at different magnetic fields and at both transition frequencies. Data labeled upper was measured at the $|0\rangle \rightarrow |1\rangle$ transition frequency and data labeled lower was measured at the $|0\rangle \rightarrow |-1\rangle$ transition frequency. (c) An example of a single trace from a T_2 measurement at 500 G at the lower transition frequency showing a decrease in T_2. (d) Combined T_2 data measured on a single NV at different magnetic fields and showing both transition frequencies.

5.3.4 Road map

To gain a comprehensive understanding of this effect, a theoretical model is required to provide insight into the underlying phenomena. Additionally, further measurements can assist in order to obtain a complete picture. I propose complementary measurements that can contribute to the development of such a model.

To systematically investigate these possibilities, the following experiments are proposed:

1. **Control experiments on chirality:** Measuring a non-chiral sample will confirm whether the observed effect is indeed due to chirality. It is possible that the noise is due to additional surface spins and this must be ruled out. Measuring on both left- and right-handed chiral samples is also a possible route. Yet, this is not expected to have a different result. The measurement with the NV detects noise fluctuations and is sensitive to the noise squared[93]; for this reason, an interaction with the opposite direction is not expected to have a different result.

2. **Depth dependence:** A possible explanation for the observed variation in relaxation time among different NV centers is their depth within the diamond. To test this hypothesis, it is necessary to measure the depth[96] of both NV centers that exhibited the effect and those that did not, determining whether the phenomenon is more pronounced in shallow NVs. Depth can be determined by placing a calibration sample on the diamond and detecting the NMR signal. This is done using immersion oil as a sample and sensing with a dynamical decoupling sequence XY-8-n (Ch. 2.2).

3. **Magnetic field inversion:** Applying a magnetic field and subsequently inverting its direction could offer additional information. If the interaction reverses upon field inversion, it would be consistent with the Chiral-Induced Spin Selectivity (CISS) effect. Observing such a difference would serve as a key indicator for refining a theoretical model.

4. **Electric field modulation:** Applying an electric field to the chiral molecule polarizes the molecules and is expected to enhance the effect[52]. There are several ways to implement such an electric field. One option is to deposit an insulating layer of MgO above the poly-alanine molecular layer and above the insulator to deposit a metal electrode. This may risk quenching of the NV charge state as shown with gold above. Alternative metals such as a copper electrode are possible, yet copper has been shown to reduce relaxation time T_1[133] which would change the baseline for the measurement. An alternative method is to use a metal sheet, such as a gold-coated glass slide, placed above the diamond as the top electrode. The lower electrode can be the copper waveguide, which sits beneath the diamond. Either method should take the spin-to-charge mechanism into consideration.

5. **Temperate control:** The CISS interaction is expected to be enhanced at low temperatures. As such, measuring the noise fluctuations at low temperature can give more insight to the interaction. However, working with the cryogenic NV setup is technically challenging, particularly when attempting to repeatedly measure a specific NV. It is alternatively possible

to heat the chamber encapsulating the NV and raise the temperature. This is expected to decrease the CISS effect, such a change can also point to the CISS mechanism.

These experiments will provide essential insights into the nature of the NV-chiral molecule interaction, helping to distinguish between direct and indirect mechanisms and contributing to the development of a comprehensive theoretical model.

6
Discussion

To infinity and beyond!

Buzz Lightyear

This thesis presents advancements in two seemingly distinct areas of nanoscale magnetic resonance sensing: nanoMRI and surface sensing techniques. These developments not only push the limits of high-resolution spin imaging but also provide insights into molecular-scale surface interactions.

6.1 Advancements in nanoMRI

The results presented in this thesis demonstrate the successful integration of a current-focusing device (CFD) with an NV sensor for nanoscale MRI applications. Specifically, I have shown that the developed tip can sustain a current sufficiently strong to induce the magnetic field gradients required for high-resolution nanoMRI. The field generated by the tip was localized around an NV center, with a measured spatial gradient on the order of $\sim 1\frac{\mu T}{nm}$. This can be further increased by raising the applied current nearly 10-fold which is expected to induce a gradient of $8.27\frac{\mu T}{nm}$. The achieved gradient is already practical for nanoscale resolution and the expected high current gradient can push the resolution further. Additionally, I demonstrated that the Rabi power is modified in the presence of the tip. An analytical model was developed to account for the currents induced in the tip by the microwave signal and these cause a spatial dependence of the Rabi power. The possibility to enhance the Rabi power without additional heating can be leveraged in experiments where heating is detrimental. In particular, mitigating Rabi-induced heating can help prevent signal drift, which can be controlled by precise tip positioning. Moreover, the Rabi power spatial

dependence is an additional gradient effect that may be leveraged to apply spatially dependent pulse sequences, similar to the gradient in the magnetic field.

These findings suggest immediate steps that can be done to further advance nanoMRI. First, the demonstrated gradient should be used to image electron spins, particularly those native to the diamond surface, following the approach developed by Grinolds et al.[94]. While this work has established the feasibility of such imaging, an experimental demonstration is a clear next objective. Another important step is to extend nanoMRI to molecular samples of interest, such as engineered "molecular rulers"[122] designed with well-defined dimensions to validate the imaging of external spins. This capability would open the door to imaging biologically or chemically relevant molecules with nanoscale resolution.

Beyond resolution improvements, new pulse sequences offer an alternative route for advancing nanoMRI. For instance, flipping the gradient during the spin evolution phase could enable the realization of a Hahn echo pulse within the nanoMRI protocol. Additionally, the CFD functions as a scanning electromagnet, which could extend its utility to other research fields where local current control or nanoscale electric fields are of interest. These aspects suggest broader applications beyond nanoMRI, potentially influencing fields such as quantum sensing, condensed matter physics, and nanoscale electromagnetism.

6.2 Challenges and progress in surface sensing

A key challenge in NV-based surface sensing is the preparation of molecular samples while ensuring the detection of spin signals, for instance from self-assembled monolayers (SAMs). In this work, I explored multiple methods for preparing and characterizing molecular samples optimized for NV sensing. The success of these preparation techniques was confirmed using X-ray photoelectron spectroscopy (XPS) and confocal microscopy, yet direct NV-based detection of the SAM remained unsuccessful. The primary obstacle was the presence of native surface electrons on the diamond, which masked the external spin signal from the SAM. This limitation underscores a fundamental hurdle in using NV centers for molecular-scale surface studies.

Comparing this approach to ensemble NV-based sensing, where surface nuclear magnetic resonance (NMR) has been demonstrated, highlights a critical challenge in bridging the gap between single-NV and ensemble-based measurements. Single NV centers have successfully detected individual spin labels, while ensemble NVs have been able to probe monolayers. However, when working with single NVs, the high density of spins within a SAM, along with the surface election density, makes it difficult to isolate individual spin signatures while still achieving nanoscale resolution. This trade-off presents a key challenge for high-resolution molecular surface imaging.

Additionally, I explored the surface effect of chirality-induced spin selectivity (CISS) by measuring the magnetic noise fluctuations induced by a chiral SAM. A measurable increase in noise was observed upon adsorption of chiral molecules onto an oxide-coated diamond surface, suggesting an interaction mediated by CISS effects. Notably, this effect was detected without an applied current and in the absence of an intermediate magnetic layer, this points to an interaction with the chiral molecules and specifically to the effect of CISS. Although a quantitative model should

be developed to describe the magnetic fluctuations the measurement itself is already novel. The observation can point to direct magnetic noise caused by the molecule or alternatively it can be described by a surface interaction mediated by CISS. It is suggested that further measurements be conducted to give insight to the role of CISS in the interaction. These findings highlight the potential of NV-based surface magnetic resonance to explore physical phenomena that conventional techniques may not fully resolve.

6.3 Future outlook: towards nanoscale surface MRI

Looking forward, a promising future direction is the integration of gradient magnetic resonance imaging with surface sensing, enabling nanoscale surface MRI. One long-term goal in nanoMRI is to achieve single-molecule imaging which requires resolution on the order of the bonds within a molecule. At the same time, a second research avenue is the study of surface science at the nanoscale. Although NV quantum sensing has successfully detected magnetic resonance signals, applying this technique to diverse nanoscale systems—including 2D materials, molecular monolayers, and nano-devices—requires overcoming several key obstacles. Unlike conventional atomic force microscopy (AFM) or optical imaging, where samples are placed on non-interfering substrates, NV sensing inherently requires proximity to a diamond substrate. This constraint complicates sample preparation and introduces unwanted surface interactions. One approach to circumvent this limitation is the use of scanning NV probes, which offer spatial flexibility but remain technically challenging and are incompatible with the focused gradients introduced by the CFD, which is essential for high spatial resolution.

For a static diamond platform incorporating gradient-based nanoMRI, the sample must be adhered directly to the diamond surface. This work has contributed two key advancements toward realizing this future vision:

1. Developing methods to adhere and detect molecular samples on the diamond surface.
2. Applying local magnetic field gradients that enable the transition from an integrated magnetic resonance signal to high-resolution spin imaging.

By integrating the techniques developed in this work, nanoscale surface science can advance toward answering fundamental questions at the molecular level, such as:

1. What is the molecular density of the sample?
2. Are there structural defects or variations in surface composition?
3. Do subdomains exist, and what role do spin or charge interactions play in their formation?
4. What are the magnetic properties of local regions?

While some of these questions can be addressed using XPS, AFM, and FTIR, my research demonstrates that these traditional techniques provide incomplete information, particularly regarding

local heterogeneity and site-specific interactions. Throughout my investigation of molecular surfaces, it became evident that existing techniques often yield only ensemble-averaged data, lacking sensitivity to local perturbations. One challenge met at the nanoscale were the surface electrons which masked the detection of the spin layer SAM. This can be overcome by applying a gradient field which separates the resonance of the different species which are located a few nanometer apart. By combining surface-sensitive NV techniques with nanoMRI, nanoscale surface science can evolve to resolve local magnetic and electronic properties with unprecedented spatial resolution.

6.4 Conclusion

This work contributes significant advancements to both nanoMRI and surface magnetic resonance, demonstrating the feasibility of high-resolution magnetic imaging and molecular surface sensing. The development of the CFD provides an approach to generating strong, localized magnetic field gradients, paving the way for improved nanoMRI techniques. Additionally, the challenges identified in surface sensing highlight the need for continued development in NV-based molecular detection strategies. By merging these techniques, single-molecule MRI and nanoscale surface MRI could become a reality, providing new insights into molecular structure, molecular interfaces and interactions, quantum materials, and biological systems at the atomic scale.

A

Derivation of Ramsey pulse sequence

A.1 Pulse evolution

The following shows the derivation of the read out of a Ramsey pulse sequence described in Ch. 2.2. The state is initiated with a $\frac{\pi}{2}$-pulse, $\mathbf{B} = B_1 \cos(\omega t)$, where $\omega t = \frac{\pi}{2}$. In the rotating frame

$$|\psi\rangle = \frac{1}{\sqrt{2}} \left(|0> + |1>\right) \tag{A.1}$$

The state then evolves for a time t and acquires a phase:

$$\begin{aligned} \Delta\phi &= \int^{t} \Delta\tau d\tau \\ \varphi &= \omega_0 t \end{aligned} \tag{A.2}$$

Resulting in the state:

$$|\psi\rangle = \frac{1}{\sqrt{2}} \left(|0> + e^{-i\varphi}|1>\right) \tag{A.3}$$

A second $\frac{\pi}{2}$ pulse converts back to the state along z, where the Hamiltonian for this operator is

$$\begin{aligned} \mathcal{H} &= -\gamma S \cdot B \\ &= \frac{\gamma\hbar}{2}\sigma \cdot B \\ &= \frac{\hbar}{2}\sigma_y \gamma B_y \end{aligned} \tag{A.4}$$

Applying this operator to the state

$$\begin{aligned} U(t) &= \exp\left(-\frac{i\mathcal{H}t}{\hbar}\right) \\ &= \exp\left(-i\frac{1}{2}\sigma_y\gamma B_y t\right) \end{aligned} \tag{A.5}$$

The propagation in time:

For a $\frac{\pi}{2}$ pulse we set $\gamma Bt = \frac{\pi}{2}$ and $\sigma_y = \begin{pmatrix} 0 & -i \\ i & 0 \end{pmatrix}$:

$$U\left(\frac{\pi}{2}\right) = \exp\left(-i\frac{1}{2}\sigma_y\frac{\pi}{2}\right) = \exp\left(-i\frac{\pi}{4}\sigma_y\right) \tag{A.6}$$

$$\begin{aligned} U\left(\frac{\pi}{2}\right)|\psi> &= e^{i\left(\sigma_y\frac{\pi}{4}\right)}|\psi> \\ &= e^{i\left(\sigma_y\frac{\pi}{4}\right)}\frac{1}{\sqrt{2}}\left(|0> + e^{-i\varphi}|1>\right) \\ &= \frac{1}{\sqrt{2}}\left(1\cdot\cos\left(\frac{\pi}{4}\right) + i\sigma_y\sin\left(\frac{\pi}{4}\right)\right)\left(|0> + e^{i-i\varphi}|1>\right) \\ &= \frac{\sqrt{2}}{2}\frac{1}{\sqrt{2}}\left(|0> + e^{-i\varphi}|1> - |1> + e^{-i\varphi}|0>\right) \\ &= \frac{1}{2}\left[\left(1+e^{-i\varphi}\right)|0> + \left(1-e^{-i\varphi}\right)|1>\right] \end{aligned} \tag{A.7}$$

Finally, we read out the state to give:

$$\begin{aligned} |<0|\alpha>|^2 &= \left|<0|\frac{1}{2}\left(1+e^{-i\varphi}\right)|0>\right|^2 \\ &= \frac{1}{4}\left(1+e^{-i\varphi}\right)\left(1+e^{i\varphi}\right) \\ &= \frac{1}{4}\left(1+e^{i\varphi}+e^{-i\varphi}+1\right) \\ &= \frac{1}{2}\left(1+\cos\theta\right) \end{aligned} \tag{A.8}$$

Where $\theta = \omega t$ and in the rotating frame $\omega = \omega_0 - \omega_L$, and ω_0 is the frequency of the applied microwave field and ω_L is the resonance of the transition. Thus a detuning is detected by measuring the oscillations in the Ramsey decay.

For the NV center with implanted nitrogen ^{15}N there is a hyperfine coupling [150] of the $|\pm1\rangle$ state due to the spin $\frac{1}{2}$ of the ^{15}N where $A_{\parallel} = 3.03\,\text{MHz}$. Thus, the resonance frequency is $D \pm \gamma B \pm \frac{A}{2}$ and we expect to see two oscillating frequencies. Additionally, the signal dephases, and there is an exponential decay. The final signal is expected to be -

$$f(t) = e^{-t/T_2^*}(\cos(2\pi(\omega + A/2)t) + \cos(2\pi(\omega - A/2)t)) \tag{A.9}$$

B

Setup details extended

B.1 Optical setup

B.1.1 Telescope - extended details

In the optical setup described in Ch. 2.3.3 there is a telescope configuration between the galvanometer scanner to the objective. These lenses act as a tube lens and a scan lens and are intended to project the galvanometer plane to the back focal plane of the objective.

Without the two lenses, two beams at different angles will focus to different planes. This is shown in the ray trace of a scanned beam for two distances between the scanner to the objective in Fig. B.1. As the distance increases the error in the focal plane of the two beams increases. To mitigate this effect[151] a tube lens and a scan lens are placed between the scanner to the objective, Fig. B.2. In the setup there are limitations on the placement of the lenses due to the box that confines the microscope this results in a sub-optimal placement of the objective lens as shown in the lower image in Fig. B.2. Even with the error this still provides an improved scan range.

B.1.2 wide field image

The image from the CCD that provides a wide field image of the diamond as described in Sec. 2.3.3 is shown in Fig. B.3.

B.2 Waveguide details

The MW signal is applied using a waveguide which is fabricated in house. Two processes were used for different waveguides used in this work:

1. Option 1

   (a) 5 nm Cr and 300 nm Cu are deposited on a clean glass slide

   (b) Photolithography is used to prepare the waveguide pattern on the metal.

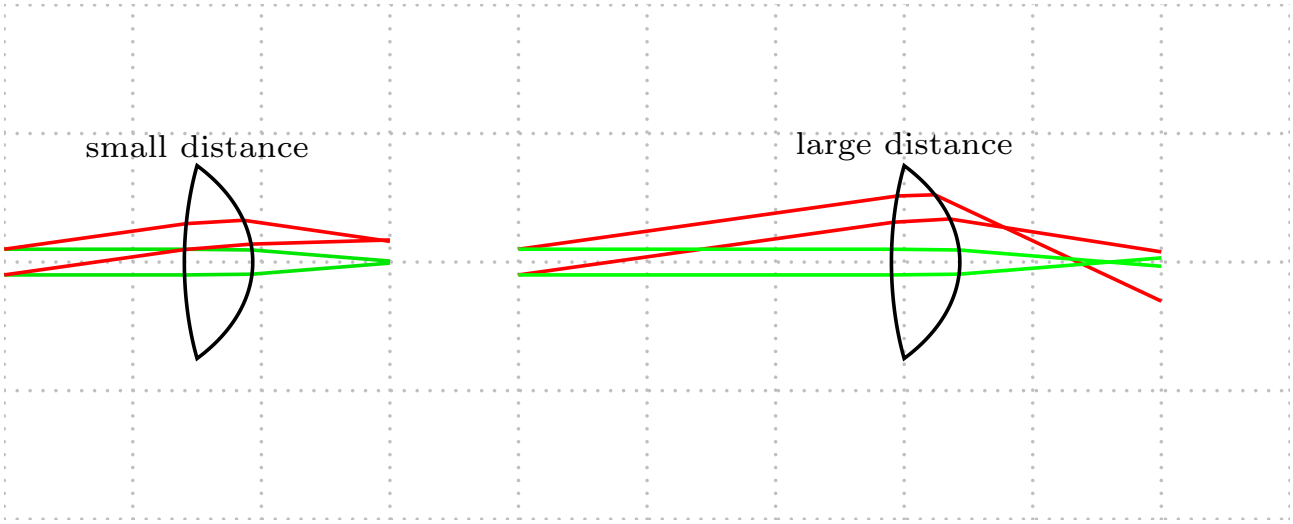

Figure B.1: Effect of the galvanometer scanner on the focal point of the beam entering the objective. The effect is shown for a small and large distance between the two and demonstrates the enhanced error for longer distance. The red and green rays represent different scan deflection.

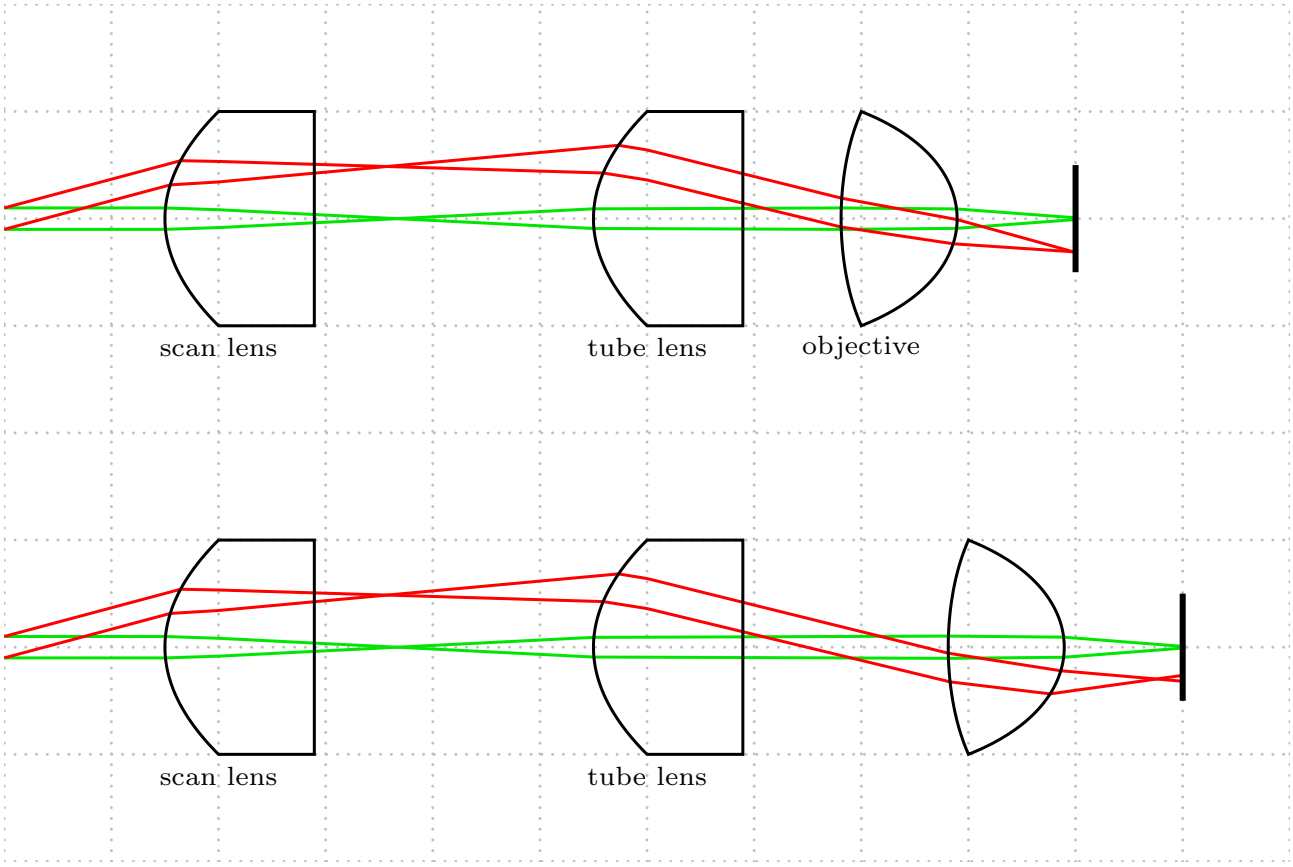

Figure B.2: Showing the ray trace of a scanned beam focused on the objective for illumination of the diamond. The effect of adding a scan lens and tube lens is shown for the objective placed correctly at the focal point of the tube lens and for an objective shifted from the correct placement due to geometric constraints.

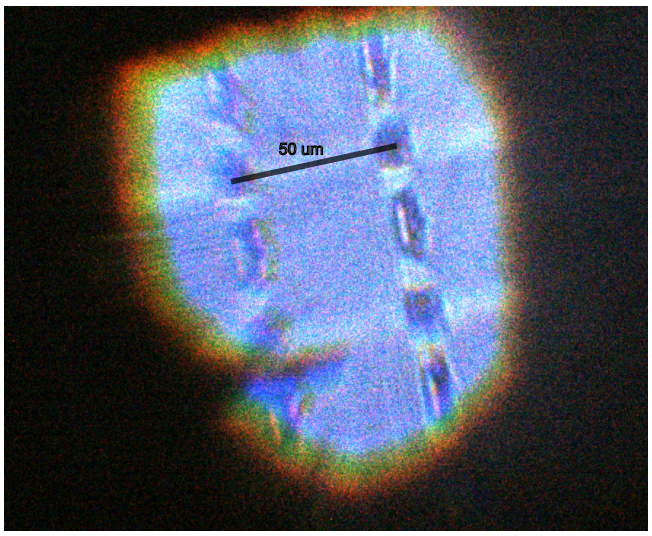

Figure B.3: The wide field image from the CCD imaged using the objective that focuses the laser to the diamond. The image shows the grid layout of the diamond pillar array. The dark region shadow is the tip that is near the diamond surface. The lens does not correct for chromatic aberration and the illumination used is white and so chromatic aberrations are visible.

(c) Electroplating is used to deposit copper according to the waveguide pattern.

(d) The metal seed layer is etched (8% APS for Cu and 30% HCl for Cr) in order to separate the center line from the ground and expose the glass slide below.

This results in a copper center line that has a thickness of roughly 15 µm.

2. Option 2

(a) 5 nm Cr and 2000 nm Cu are deposited on a clean glass slide.

(b) Photolithography is used to prepare the waveguide pattern on the metal.

(c) The metal is etched (8% APS for Cu and 30% HCl for Cr) to remove the base metal and separate the center line from the ground and expose the glass slide below.

This results in a waveguide with a copper center line that has a thickness of roughly 2µm.

The waveguide is soldered to a PCB which is designed with two SMA ports for insertion and output of the MW signal. The waveguide is characterized by the lass as a function of frequency, an example of such a measurement is shown in Fig. B.4. The figure shows several resonances in the waveguide, the Rabi time will change when working at these frequencies as the effective Rabi power at the sample is lower.

B.3 Mechanical parts figures

This section elaborates on the mechanical details regarding the tip apparatus presented in Sec. 3.2 in the main text. The quartz rod is designed to have two indented grooves to prevent a short between the two leads. The design of the quartz rod is shown in Fig. B.5.

A grid was designed to hold the tips during the deposition, as described in Ch. 3.2, it is shown in Fig. B.6.

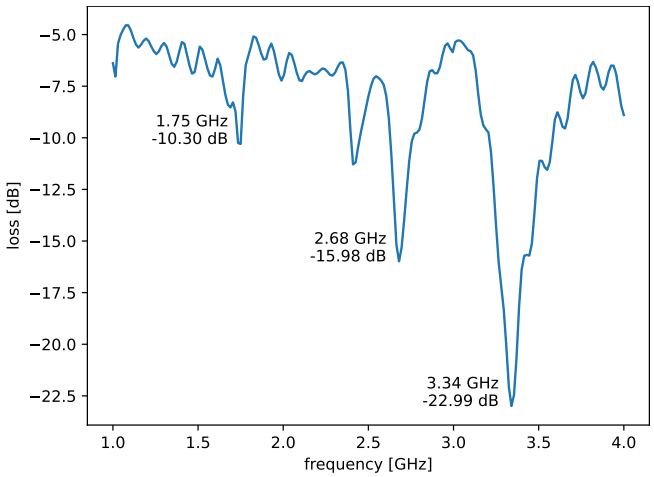

Figure B.4: Waveguide characterization, the loss is measured as a function of frequency.

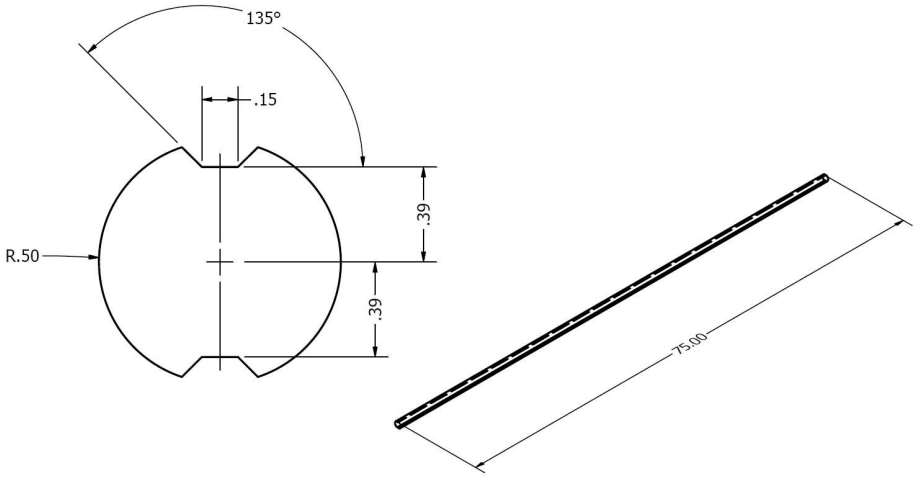

Figure B.5: Design of quartz rod used as the base material for fabricating the CFD.

For the apex deposition, a metal sheet is placed on each side of the grid to prevent a short due to deposition between the leads, shown in Fig. B.7. The metal sheet is flush with the edge of the grid, extending the metal beyond the grid results in thin apex deposition, which is unwanted. The tips are cut such that they are within the holder and mask, this was found to mitigate the effect of shorting the leads. A cylindrical tip holder was designed to hold the tip. Two springs are placed within the holder to provide mechanical and electric contact. The tip holder was fabricated using CNC machining. It is made of PEEK, which is well-suited for CNC machining and provides electric insulation. The cylindrical holder is held by a titanium holder which acts as an adapter to connect to the attocube stage. The design was done by the Instrument Design Unit at the Weizmann Institute of Science. The springs are pushed into the two niches. An electric pin is soldered to each spring and each will then connect to the center line of a coaxial cable for the current in and out of the tip. The coaxial cables used to connect the tip to the attocube are MK5005-SMA11-offen-0200 purchased from *elspec group*. They are ultra-flexible (and delicate) and so they do not strain the device or pull on the microscope's motors. An adapter was designed to hold the tuning fork and to connect the tuning fork to the tip, Fig. B.9. The angle of the adapter is designed

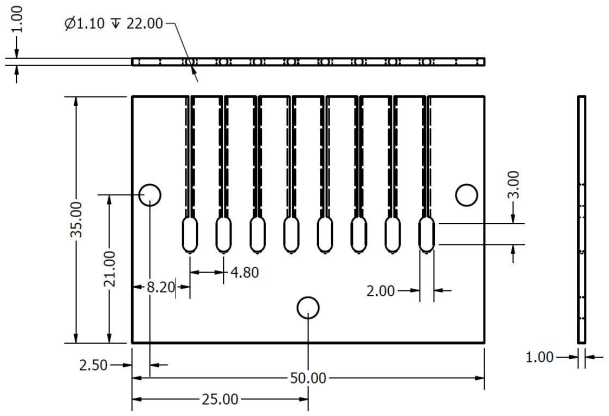

Figure B.6: Design of the holder for the tips that is used for the deposition. The tips are placed in the holder such that the grooves are facing the metal to avoid deposition in the groove. The tip length is cut such that the tip apex is just below the edge of the holder.

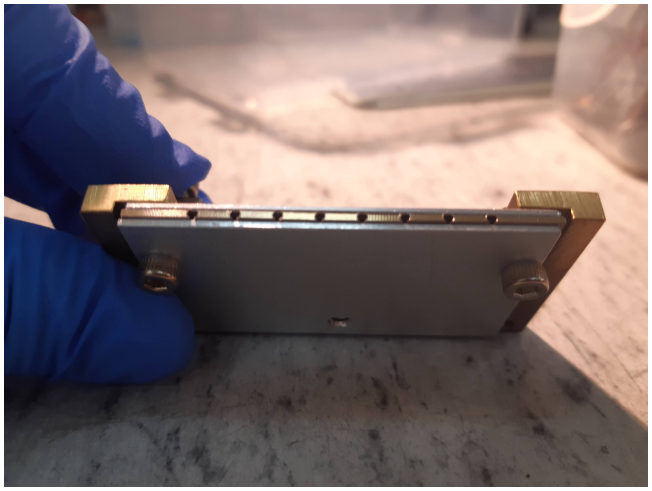

Figure B.7: During the stage of apex deposition, a metal sheet is placed on each side of the grid to prevent deposition within the grooves.

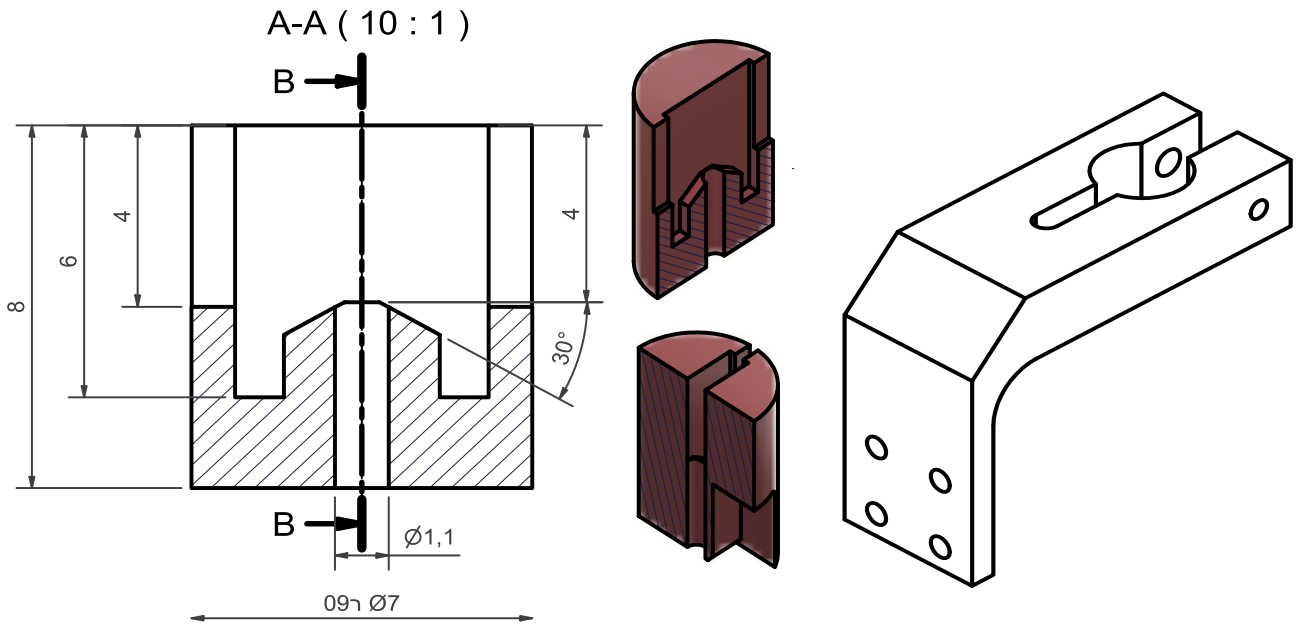

Figure B.8: Mechanical drawing of the tip holder (left) made of PEEK and the titanium stage adapter (right).

Figure B.9: Image of tuning fork in the holder, the tuning fork is first soldered to a wire and then glued to the base with super glue. The angle of the holder is set such that the tuning fork will slightly press the tip when placed in the tip holder.

such that the tuning fork will press against the edge of the tip.

B.4 Details on electronics

Current is applied to the tip by applying a voltage to the tip, the voltage is calculated according to Ohm's law $V = IR_{circuit}$ where $R_{circuit}$ is the resistance measured with a multimeter between the input and output connectors to the tip. The actual current through the tip is measured on the oscilloscope with 50 Ω termination. The current measured is calculated as $I_m = \frac{V_m}{R_{osc}}$, where I_m is the measured current V_m is the average voltage measured in the time the voltage is constant (see Fig. 4.2) and R_{osc} is 50 Ω. I did a series of such measurements to check that current to voltage ratio is linear, indicating that the tip resistance does not change due to heating. This is used as a calibration curve so that I do not need to record the signal on the scope for every current pulse.

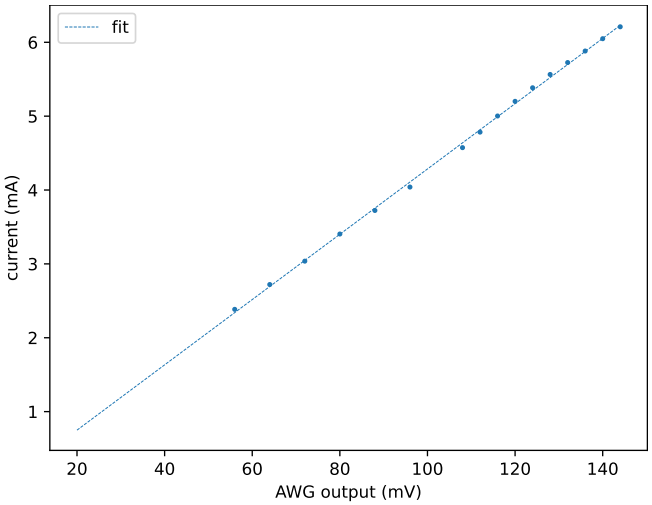

Figure B.10: Current output measurement The current measured on the scope as a function of the voltage applied by the AWG.

C

Additional measurements

C.1 CFD development

As previously discussed, the NV contrast is reduced in the presence of magnetic field components that are perpendicular to the NV axis. The magnetic field generated by a CFD tip with a large apex diameter of 1300 nm and a current of 2 mA was analyzed in Sec. 3.1.2. At this current, the overall magnetic field is relatively weak, and thus no significant reduction in contrast is expected. The contrast is calculated at a distance of 25 nm from the tip apex using the method described in Sec 2.1.4. The field of the CFD is calculated for lab coordinates which are not parallel to the NV axis and so the field is projected the axis parallel and perpendicular to the NV axis. As shown in Fig. C.1(a), the contrast remains nearly uniform across the scan area, indicating minimal impact from off-axis magnetic fields. In contrast, for a CFD tip with a finer apex diameter of 100 nm, the effect of off-axis fields becomes more pronounced. As shown in Fig. C.1(b), the contrast exhibits greater spatial variation. In this case, pulsing the current becomes more critical to preserve NV readout contrast. For stronger magnetic fields—such as those generated by higher currents, the reduction in contrast remains modest but non-negligible, further highlighting the importance of current modulation in future designs.

C.2 CFD measurements

A measurement of fluctuations in the background magnet field is shown in Fig. C.2. As mentioned in Ch. 4, Sec. 4.2, the ODMR measurement includes a measurement with current and a reference without. The figure shows the shift in frequency relative to the mean measured during the reference phase in the ODMR measurement for each pixel measured. The data shows a max-

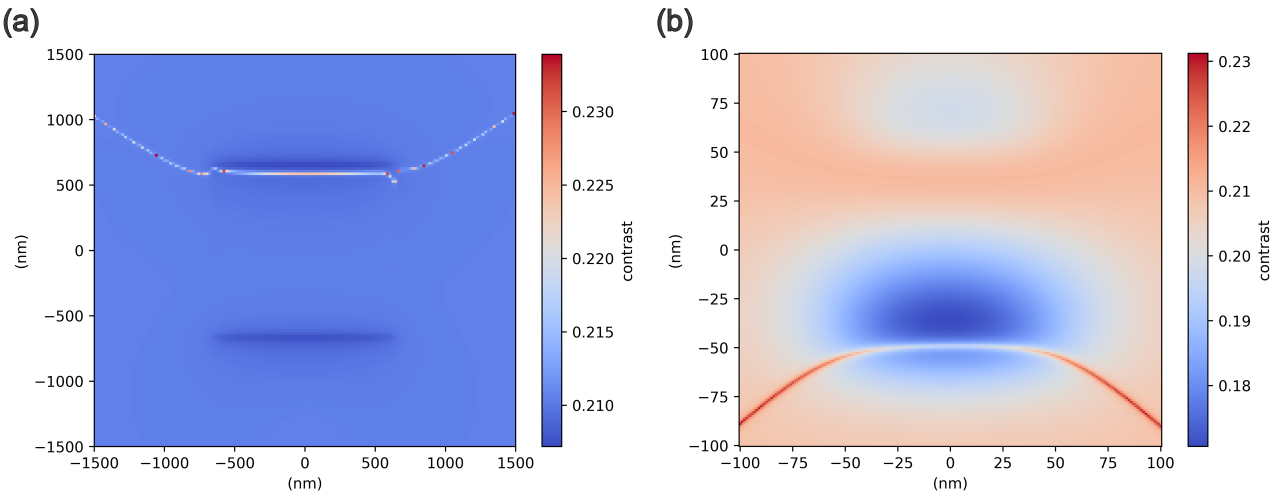

Figure C.1: The contrast of the NV under the effect of the simulated magnetic field from the CFD with a current of 2 mA and at a distance of 25 nm. (a) The contrast for a CFD with an apex diameter of 1300 nm. (b) The contrast for a CFD with an apex diameter of 100 nm.

imum fluctuations of 1 MHz and a region where the field is shifted from the mean by 500 kHz. This is on the order of the system sensitivity highlighting the need to cancel small drifts in order to sense small changes in the magnet field of the tip.

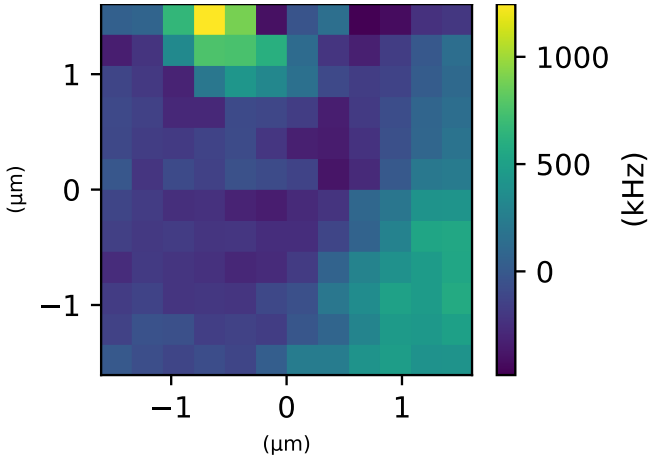

Figure C.2: Measurement of fluctuations in the background magnetic field, without a current in the tip. A 2D scan of the frequency measured from the ODMR sequence without a current, the total measurement time is roughly 20 hours. The measurement shows the difference between mean frequency measured to the frequency measured at each pixel in the background field over time.

C.3 High current measurements

When measuring the magnetic field at increasing currents two series of line scans where performed, initially at low current followed by a series of scans at higher current. The first round is shown in the main text, the second series is shown in Fig. C.3. The line scans were performed along the line where the maximum gradient is expected, yet the two series showed a different typical line shape, indicating there was a shift in the scanned line. The line scans demonstrate an increase in the magnetic field measured and in the gradient as a function of increasing current. At a current of

14.2 mA the CFD appears to fail, the ODMR shift measured falls to zero after two measurements. This accumulated effect may indicate that longer wait time could allow the device to continue to function.

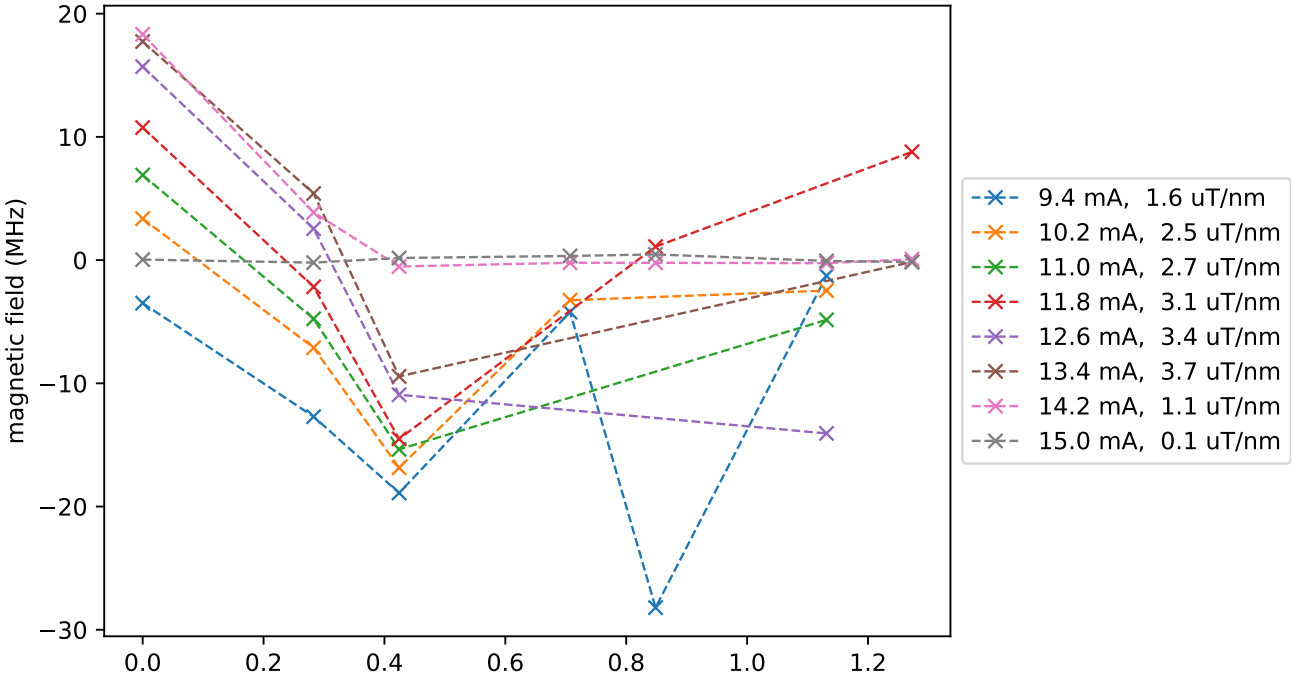

Figure C.3: Magnetic field line scans done at high current. The tip failed at 14.2 mA where the shift in magnetic field is zero.

C.4 Measuring chiral molecules

A confocal scan of the ROI within the diamond where the chiral measurements were conducted, this is shown for future reference in Fig. C.4. The figure shows the relative placement of the diamond to the waveguide and the chosen region E-5. The NVs marked NV 6 and NV 22 showed increased noise due to the chiral SAM, the data in the main text is from NV 6 (Fig. 5.5, while NV 5 did not show an effect and the data in Fig. C.5 was measured on this NV

Below is a second example of a data set measured with a SAM of chiral molecules as described in Ch. 5.3. The data shown here is another NV that is within 50 µm of the NV shown in the main text. Here, the relaxation measured is similar with and without the SAM, highlighting the statistical nature of the measurement.

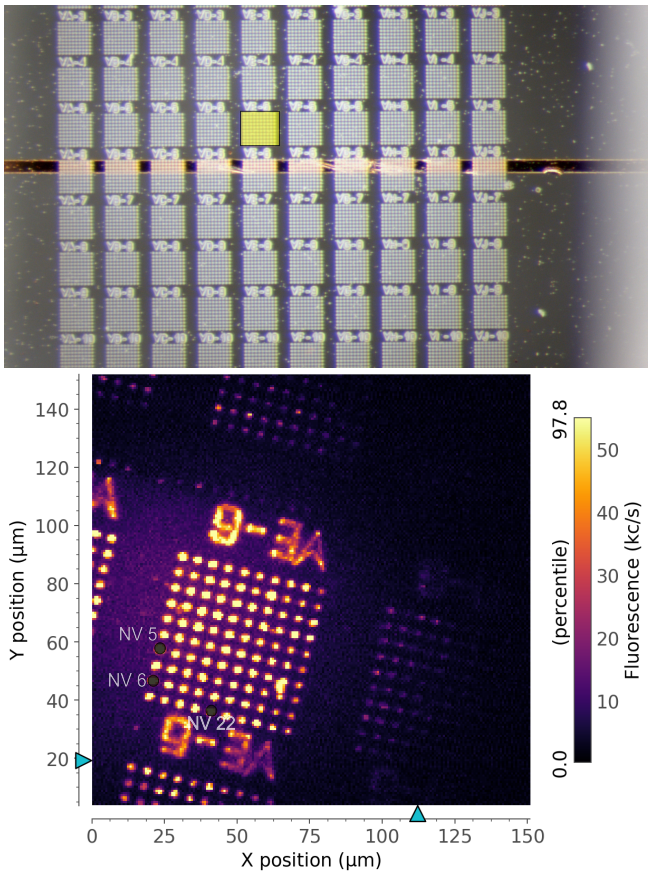

Figure C.4: Image of the diamond and the working region where the measurements were done. (top) Optical microscope image of the diamond showing the relative location to the waveguide, the yellow box highlights the working region, E-5. (bottom) confocal scan of the working region E-5 where the measurements with the chiral SAM were conducted.

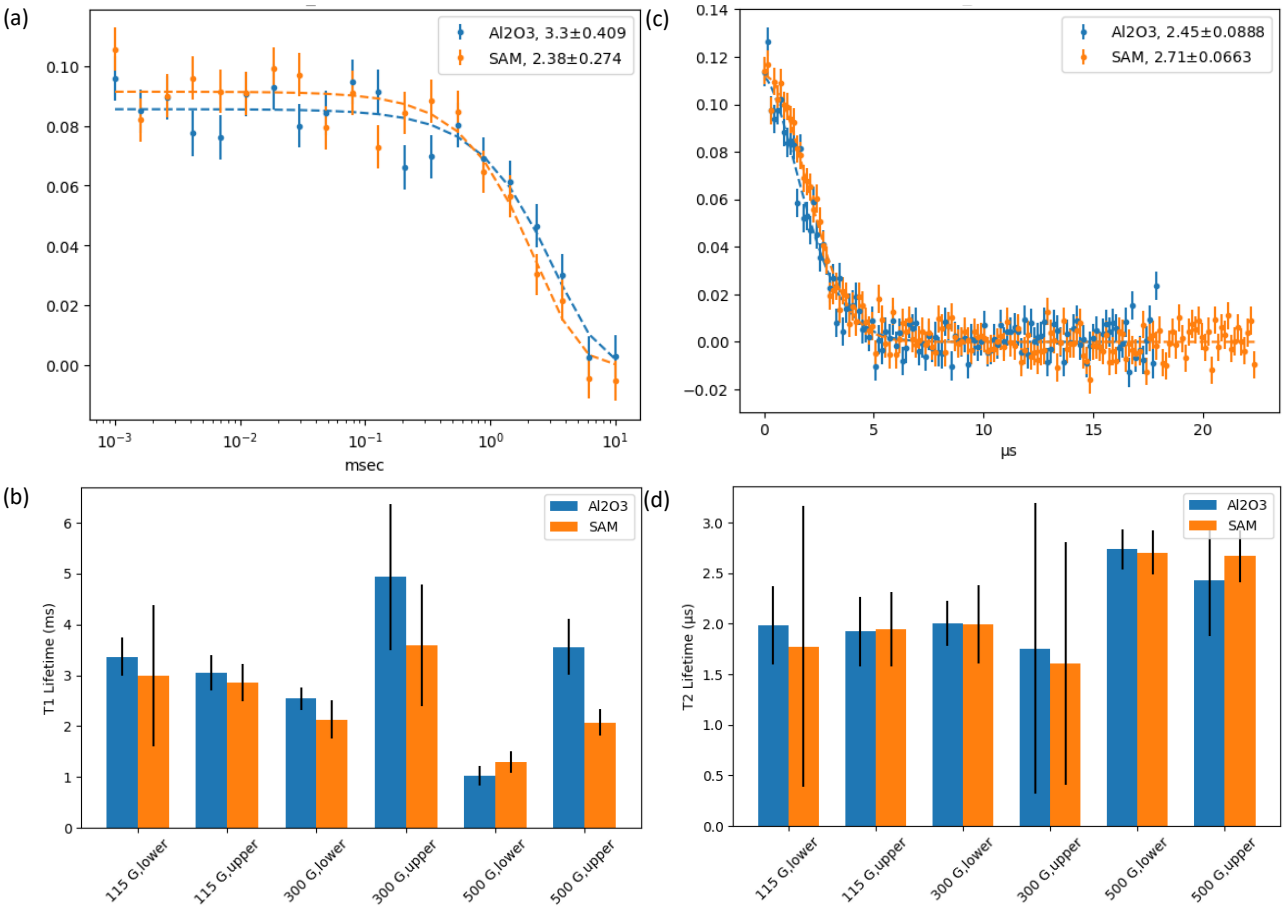

Figure C.5: Relaxation measurements using the pulse sequence for T_1 and T_2 are shown for an NV where the effect of the SAM is not apparent. (a) An example of a single trace from a T_1 measurement, the decay rate with and without the SAM is similar. (b) Combined T_1 data measured on a single NV at different magnetic fields and at both transition frequencies. (c) An example of a single trace from a T_2 measurement, the decay rate with and without the SAM is similar. (d) Combined T_2 data measured on a single NV at different magnetic fields and showing both transition frequencies.

D

Rabi power modification

D.1 The Model

Most simplified analytical models used to model the contribution of metallic tips to the electromagnetic near-fields replace the tip itself with a spherical metallic particle, or an elongated prolate spheroid[152]. Here, due to the proximity of the tip to the surface, and its flat apex, we chose to model it as a stack of oblate spheroids (as shown in Fig. D.1b) to better capture the effect of the flat on the magnetic fields, especially when it is very close to the surface. The aspect ratio we took is 1:35 (long semi-axis of $A_x = 0.7$ μm), and the number of ellipsoids was chosen such that it covers roughly a cylinder with height = diameter of the oblate ellipsoid. Adding more spheroids does not alter the resulting fields significantly, since their field at the position of the NV decays quite rapidly with their distance (roughly as $1/\text{distance}^3$). Since the excitation of the tip is at 2.26 GHz, corresponding to a wavelength of ∼13 cm (or roughly 5 cm in the glass), the scenario is in the deep sub-wavelength (hence quasistatic) regime. Therefore, we used a magnetostatic solution for the response of the metallic tip, where the field exciting each ellipsoid is the magnetic field generated by the CPW. The solution for a single metallic (perfectly electric conductor, or PEC) ellipsoid in a uniform field was obtained by solving the scalar magnetostatic potential problem for a uniform field in $\hat{x}, \hat{z}$[153].

An analytical expression for the field of the co-planar waveguide (CPW) was derived using a conformal mapping technique[154]. Assuming waves propagate along $\hat{z}$ in the CPW (later we rotate

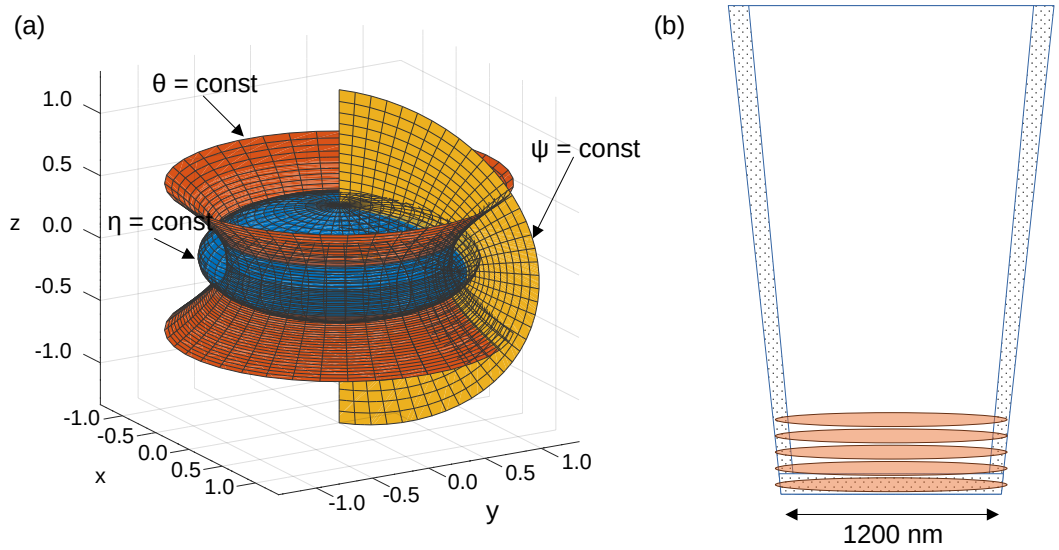

Figure D.1: (a) The oblate spheroidal coordinate system. η defines the spheroid surface, θ the polar angle and ψ the azimuthal angle. (b) Modelling the electromagnetic response of the tip (blue) by an array of ellipsoids (pink).

the result), and the CPW plane is XZ (cross-section plane is XY), we get:

$$E_{\mathrm{x,CPW}}(x,y) = \mathrm{Im}\left(\frac{1}{\sqrt{a^2-(x+iy)^2}\sqrt{b^2-(x+iy)^2}}\right) \tag{D.1}$$

$$E_{\mathrm{y,CPW}}(x,y) = \mathrm{Im}\left(\frac{i}{\sqrt{a^2-(x+iy)^2}\sqrt{b^2-(x+iy)^2}}\right) \tag{D.2}$$

Assuming the mode propagating in the CPW is TEM, we get

$$\mathbf{H}_{\mathrm{CPW}} = \hat{z} \times \mathbf{E}_{\mathrm{CPW}} \tag{D.3}$$

We also assume that the diamond layer does not alter the fields significantly. In practice, it does affect their magnitude, but their direction remains approximately the same, and since the entire effect is linear to the field, this does not affect the results.

Response of ellipsoids

The ellipsoids are defined in an oblate spheroidal coordinate system (see Fig. D.1a), with $2a$ being the distance between the focal points, and $\eta = \eta_0$ defining the spheroid surface. In this case, the magnetic field generated by the ellipsoid itself (eventually, by the tip) can be described using a scalar potential φ_m. These response magnetic fields are generated by the currents induced on the tip by the external magnetic field of the CPW.

For a background field of $H_{0,z}\hat{z}$ we get

$$\varphi_{m,z} = \frac{H_{0,z}\cosh\eta_0}{\cosh\eta_0\,\mathrm{cot}^{-1}(\sinh\eta_0)}\left[\sinh\eta\,\mathrm{cot}^{-1}(\sinh\eta)-1\right]\cos\theta. \tag{D.4}$$

Here θ is the polar angle in the oblate spheroidal coordinate system, and ψ is the azimuthal angle. For a background field of $H_{0,x}\hat{x}$ we get

$$\varphi_{m,x} = C_x \left(\sqrt{1+\zeta^2}\cot^{-1}\zeta - \frac{\zeta}{\sqrt{1+\zeta^2}} \right) \cos\psi \sin\theta, \quad \zeta = \sinh\eta, \tag{D.5}$$

with

$$C_x = \frac{H_{0,x}\sinh\eta_0}{\cosh\eta_0 \left(\frac{\zeta_0 \cot^{-1}\zeta_0 - 1}{\sqrt{1+\zeta_0^2}} - \frac{1}{(1+\zeta_0^2)^{3/2}} \right)}, \quad \zeta_0 = \sinh\eta_0, \tag{D.6}$$

and the associated magnetic fields are obtained by $\mathbf{H} = -\nabla\varphi_m$. At a frequency of 2.26 GHz, the skin depth of gold is 1.6 μm. Since the thickness of the gold layer is only around 0.2 μm, the effective surface current response is weaker than for a perfect conductor. To account for this, we reduce the magnitude of the fields generated by each ellipsoid by a factor of $F_{\text{skin}} = 1 - e^{-200/1600} \approx 0.1175$. Each ellipsoid is subject to the field generated by CPW. Although there exist interactions between the ellipsoids, which will create a strongly non-uniform excitation of each, we will assume that the main contribution to their excitation is by the external field, and ignore the interaction. Finally, due to the proximity to the diamond surface, we need to consider the contribution of the image of each ellipsoid with respect to the diamond dielectric layer (taken to be $\varepsilon_{r,\text{diamond}} = 5.68$ here). Defining $\gamma = (\varepsilon_{r,\text{diamond}} - 1)/(\varepsilon_{r,\text{diamond}} + 1)$, this will multiply the $\hat{x}, \hat{y}$ components of the magnetic fields generated by the tip on the probe (considered right on the surface here) by $1 + \gamma$ and the $\hat{z}$ component of the magnetic field by $1 - \gamma$. The calculated modulation (increase or decrease) in the Rabi power relative to the far-field (when the tip is "far", i.e., more than 2 μm away from the NV in the z direction) is shown in Fig. D.2. As discussed above, the calculation takes into account the change in effective magnetic field created by the CPW on the NV due to the proximity of the metallic tip, with the tip's vertical position taken to be 150 nm above the surface of the diamond.

A simplified analysis can be made by treating each ellipsoid as a single point. Then the analytical expression for the Rabi power becomes

$$\frac{\Omega(z)}{\Omega_0} = 1 + \frac{A}{\Omega_0}\left(1 - \frac{z}{\sqrt{z^2+d^2}}\right), \tag{D.7}$$

where A is a fitting parameter, z is the vertical distance of the NV from the tip, and d is the lateral distance, in our case 360 nm. The data in Fig. 4.9(a) in the main text is fit using Eq. D.7, and plotted as a green curve in Fig. 4.9(a), agreeing with the ellipsoid model up to a small offset, with $A = 2.67\Omega_0$.

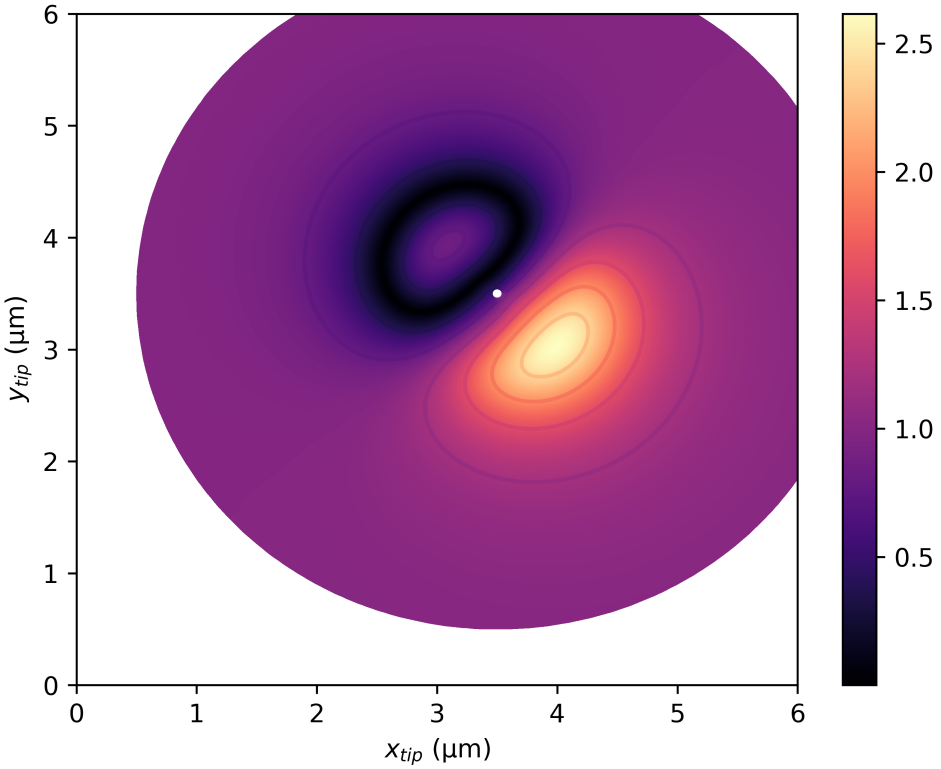

Figure D.2: Calculation of the Rabi power, Ω, as a function of tip position relative to that of the NV center (3.5 µm, 3.5 µm) divided by the Rabi power far-away, Ω_0, i.e., when the tip's vertical position is at least 2 µm away from the NV.

References

[1] Zechariah Haber, Davinder Sharma, K.S. Vijai Selvaraj, and Nir Sade. Is CRISPR/Cas9-based multi-trait enhancement of wheat forthcoming? *Plant Science*, 341:112021, 2024.

[2] C.S. Fadley. X-ray photoelectron spectroscopy: Progress and perspectives. *Journal of Electron Spectroscopy and Related Phenomena*, 178–179:2–32, May 2010.

[3] M.A. Mohamed, J. Jaafar, A.F. Ismail, M.H.D. Othman, and M.A. Rahman. *Fourier Transform Infrared (FTIR) Spectroscopy*, pages 3–29. Elsevier, 2017.

[4] Joseph I Goldstein, Dale E Newbury, Joseph R Michael, Nicholas WM Ritchie, John Henry J Scott, and David C Joy. *Scanning electron microscopy and X-ray microanalysis*. springer, 2017.

[5] Amicia D. Elliott. Confocal microscopy: Principles and modern practices. *Current Protocols in Cytometry*, 92(1), December 2019.

[6] Jian Zhong and Juan Yan. Seeing is believing: atomic force microscopy imaging for nanomaterial research. *RSC Advances*, 6(2):1103–1121, 2016.

[7] Raffi Budakian, Amit Finkler, Alexander Eichler, Martino Poggio, Christian L. Degen, Sahand Tabatabaei, Inhee Lee, P. Chris Hammel, Eugene S. Polzik, Tim H. Taminiau, Ronald L. Walsworth, Paz London, Ania Bleszynski Jayich, Ashok Ajoy, Arjun Pillai, Jörg Wrachtrup, Fedor Jelezko, Yujeong Bae, Andreas J. Heinrich, Christian R. Ast, Patrice Bertet, Paola Cappellaro, Cristian Bonato, Yoann Altmann, and Erik Gauger. Roadmap on nanoscale magnetic resonance imaging. *Nanotechnology*, 35:412001, 2023.

[8] Robin D. Allert, Karl D. Briegel, and Dominik B. Bucher. Advances in nano- and microscale nmr spectroscopy using diamond quantum sensors. *Chemical Communications*, 58:8165–8181, 2022.

[9] Karl D. Briegel, Nick R. von Grafenstein, Julia C. Draeger, Peter Blümler, Robin D. Allert, and Dominik B. Bucher. Optical widefield nuclear magnetic resonance microscopy. *Nature Communications*, 16:1281, 2025.

[10] Harold Weinstock. *SQUID sensors: fundamentals, fabrication and applications*. Springer Science Business Media, 2012.

[11] Mamin H. Jonathon Rugar Daniel Grütter, Peter. Magnetic force microscopy (mfm). in scanning tunneling microscopy ii: Further applications and related scanning techniques. *Berlin, Heidelberg: Springer Berlin Heidelberg*, pages 151–207, 1992.

[12] A. Gruber, A. Dräbenstedt, C. Tietz, L. Fleury, J. Wrachtrup, and C. von Borczyskowski. Scanning confocal optical microscopy and magnetic resonance on single defect centers. *Science*, 276:2012–2014, 1997.

[13] Romana Schirhagl, Kevin Chang, Michael Loretz, and Christian L. Degen. Nitrogen-Vacancy Centers in Diamond: Nanoscale Sensors for Physics and Biology. *Annual Review of Physical Chemistry*, 65:83–105, 2014.

[14] P. C. Lauterbur. Magnetic resonance zeugmatography. *Pure and Applied Chemistry*, 40:149–157, 1974.

[15] Charles P. Slichter. *Principles of Magnetic Resonance*, volume 1 of *Springer Series in Solid-State Sciences*. Springer Berlin Heidelberg, Berlin, Heidelberg, 1990.

[16] P. C. Lauterbur. Image formation by induced local interactions: Examples employing nuclear magnetic resonance. *Nature*, 242:190–191, 1973.

[17] Donald B. Plewes and Walter Kucharczyk. Physics of MRI: A primer. *Journal of Magnetic Resonance Imaging*, 35:1038–1054, 2012.

[18] Malcom. H. Levitt. *Spin Dynamics: Basics of Nuclear Magnetic Resonance*. Wiley, 2008.

[19] Dieter Suter. Sensitivity of optically excited and detected magnetic resonance. *Journal of Magnetic Resonance*, 99:495–506, 1992.

[20] L Ciobanu, D.A Seeber, and C.H Pennington. 3d MR microscopy with resolution 3.7 "μm by 3.3 "μm by 3.3 "μm. *Journal of Magnetic Resonance*, 158:178–182, 2002.

[21] H. J. Mamin, M. Poggio, C. L. Degen, and D. Rugar. Nuclear magnetic resonance imaging with 90-nm resolution. *Nature Nanotechnology*, 2:301–306, 2007.

[22] Christian R. Ast, Piotr Kot, Maneesha Ismail, Sebastián de-la Peña, Antonio I. Fernández-Domínguez, and Juan Carlos Cuevas. Theory of electron spin resonance in scanning tunneling microscopy. *Phys. Rev. Res.*, 6:023126, May 2024.

[23] Lisanne Sellies, Raffael Spachtholz, Sonja Bleher, Jakob Eckrich, Philipp Scheuerer, and Jascha Repp. Single-molecule electron spin resonance by means of atomic force microscopy. *Nature*, 624:64–68, 2023.

[24] John M. Nichol, Tyler R. Naibert, Eric R. Hemesath, Lincoln J. Lauhon, and Raffi Budakian. Nanoscale Fourier-transform magnetic resonance imaging. *Physical Review X*, 3:031016, 2013.

[25] C. L. Degen, M. Poggio, H. J. Mamin, C. T. Rettner, and D. Rugar. Nanoscale magnetic resonance imaging. *Proceedings of the National Academy of Sciences*, 106:1313–1317, 2009.

[26] William Rose, Holger Haas, Angela Q. Chen, Nari Jeon, Lincoln J. Lauhon, David G. Cory, and Raffi Budakian. High-resolution nanoscale solid-state nuclear magnetic resonance spectroscopy. *Physical Review X*, 8:011030, 2018.

[27] Susanne Baumann, William Paul, Taeyoung Choi, Christopher P. Lutz, Arzhang Ardavan, and Andreas J. Heinrich. Electron paramagnetic resonance of individual atoms on a surface. *Science*, 350:417–420, 2015.

[28] C. L. Degen, F. Reinhard, and P. Cappellaro. Quantum sensing. *Reviews of Modern Physics*, 89:035002, 2017.

[29] T. Staudacher, F. Shi, S. Pezzagna, J. Meijer, J. Du, C. A. Meriles, F. Reinhard, and J. Wrachtrup. Nuclear magnetic resonance spectroscopy on a (5-nanometer)^3 sample volume. *Science*, 339:561–563, 2013.

[30] H. J. Mamin, M. Kim, M. H. Sherwood, C. T. Rettner, K. Ohno, D. D. Awschalom, and D. Rugar. Nanoscale nuclear magnetic resonance with a nitrogen-vacancy spin sensor. *Science*, 339:557–560, 2013.

[31] M. S. Grinolds, M. Warner, K. De Greve, Y. Dovzhenko, L. Thiel, R. L. Walsworth, S. Hong, P. Maletinsky, and A. Yacoby. Subnanometre resolution in three-dimensional magnetic resonance imaging of individual dark spins. *Nature Nanotechnology*, 9:279–284, 2014.

[32] J-P Tetienne, L Rondin, P Spinicelli, M Chipaux, T Debuisschert, J-F Roch, and V Jacques. Magnetic-field-dependent photodynamics of single NV defects in diamond: an application to qualitative all-optical magnetic imaging. *New Journal of Physics*, 14(10):103033, 2012.

[33] Z Veksli. Esr spectroscopy for the study of polymer heterogeneity. *Progress in Polymer Science*, 25(7):949–986, 2000.

[34] Bernhard Grotz, Johannes Beck, Philipp Neumann, Boris Naydenov, Rolf Reuter, Friedemann Reinhard, Fedor Jelezko, Jörg Wrachtrup, David Schweinfurth, Biprajit Sarkar, and Philip Hemmer. Sensing external spins with nitrogen-vacancy diamond. *New Journal of Physics*, 13:055004, 2011.

[35] Dan Yudilevich, Rainer Stöhr, Andrej Denisenko, and Amit Finkler. Mapping single electron spins with magnetic tomography. *Physical Review Applied*, 18:054016, 2022.

[36] Bo L. Dwyer, Lila V.H. Rodgers, Elana K. Urbach, Dolev Bluvstein, Sorawis Sangtawesin, Hengyun Zhou, Yahia Nassab, Mattias Fitzpatrick, Zhiyang Yuan, Kristiaan De Greve, Eric L. Peterson, Helena Knowles, Tamara Sumarac, Jyh-Pin Chou, Adam Gali, V.V. Dobrovitski, Mikhail D. Lukin, and Nathalie P. de Leon. Probing spin dynamics on diamond surfaces using a single quantum sensor. *PRX Quantum*, 3:040328, 2022.

[37] H. J. Mamin, M. H. Sherwood, and D. Rugar. Detecting external electron spins using nitrogen-vacancy centers. *Physical Review B*, 86:195422, 2012.

[38] Fazhan Shi, Qi Zhang, Pengfei Wang, Hongbin Sun, Jiarong Wang, Xing Rong, Ming Chen, Chenyong Ju, Friedemann Reinhard, Hongwei Chen, Jörg Wrachtrup, Junfeng Wang, and Jiangfeng Du. Single-protein spin resonance spectroscopy under ambient conditions. *Science*, 347:1135–1138, 2015.

[39] John M. Abendroth, Konstantin Herb, Erika Janitz, Tianqi Zhu, Laura A. Völker, and Christian L. Degen. Single-nitrogen–vacancy nmr of amine-functionalized diamond surfaces. *Nano Letters*, 22:7294–7303, 2022.

[40] Anke Krueger and Daniel Lang. Functionality is key: Recent progress in the surface modification of nanodiamond. *Advanced Functional Materials*, 22:890–906, 2012.

[41] Ming-Hua Hsu, Hong Chuang, Fong-Yu Cheng, Ying-Pei Huang, Chien-Chung Han, Jiun-Yu Chen, Su-Chin Huang, Jen-Kun Chen, Dian-Syue Wu, Hsueh-Liang Chu, and Chia-Ching Chang. Directly thiolated modification onto the surface of detonation nanodiamonds. *ACS Applied Materials & Interfaces*, 6:7198–7203, 2014.

[42] Abraham Wolcott, Theanne Schiros, Matthew E. Trusheim, Edward H. Chen, Dennis Nordlund, Rosa E. Diaz, Ophir Gaathon, Dirk Englund, and Jonathan S. Owen. Surface structure of aerobically oxidized diamond nanocrystals. *The Journal of Physical Chemistry C*, 118:26695–26702, 2014.

[43] A. O. Sushkov, I. Lovchinsky, N. Chisholm, R. L. Walsworth, H. Park, and M. D. Lukin. Magnetic resonance detection of individual proton spins using quantum reporters. *Phys. Rev. Lett.*, 113:197601, 2014.

[44] Sorawis Sangtawesin, Bo L. Dwyer, Srikanth Srinivasan, James J. Allred, Lila V. H. Rodgers, Kristiaan De Greve, Alastair Stacey, Nikolai Dontschuk, Kane M. O'Donnell, Di Hu, D. Andrew Evans, Cherno Jaye, Daniel A. Fischer, Matthew L. Markham, Daniel J. Twitchen, Hongkun Park, Mikhail D. Lukin, and Nathalie P. de Leon. Origins of diamond surface noise probed by correlating single-spin measurements with surface spectroscopy. *Physical Review X*, 9:031052, 2019.

[45] Kristina S. Liu, Alex Henning, Markus W. Heindl, Robin D. Allert, Johannes D. Bartl, Ian D. Sharp, Roberto Rizzato, and Dominik B. Bucher. Surface NMR using quantum sensors in diamond. *Proceedings of the National Academy of Sciences*, 119:e2111607119, 2022.

[46] David R. Glenn, Dominik B. Bucher, Junghyun Lee, Mikhail D. Lukin, Hongkun Park, and Ronald L. Walsworth. High-resolution magnetic resonance spectroscopy using a solid-state spin sensor. *Nature*, 555:351–354, 2018.

[47] Brian P. Bloom, Yossi Paltiel, Ron Naaman, and David H. Waldeck. Chiral induced spin selectivity. *Chemical Reviews*, 124:1950–1991, 2024.

[48] K. Ray, S. P. Ananthavel, D. H. Waldeck, and R. Naaman. Asymmetric scattering of polarized electrons by organized organic films of chiral molecules. *Science (New York, N.Y.)*, 283:814–6, 1999.

[49] B Göhler, V Hamelbeck, T Z Markus, M Kettner, G F Hanne, Z Vager, R Naaman, and H Zacharias. Spin selectivity in electron transmission through self-assembled monolayers of double-stranded DNA. *Science (New York, N.Y.)*, 331:894–7, 2011.

[50] Zouti Xie, Tal Z. Markus, Sidney R. Cohen, Zeev Vager, Rafael Gutierrez, and Ron Naaman. Spin Specific Electron Conduction through DNA Oligomers. *Nano Letters*, 11:4652–4655, 2011.

[51] Oren Ben Dor, Shira Yochelis, Anna Radko, Kiran Vankayala, Eyal Capua, Amir Capua, See Hun Yang, Lech Tomasz Baczewski, Stuart Stephen Papworth Parkin, Ron Naaman, and Yossi Paltiel. Magnetization switching in ferromagnets by adsorbed chiral molecules without current or external magnetic field. *Nature Communications*, 8:14567, 2017.

[52] Eilam Z. B. Smolinsky, Avner Neubauer, Anup Kumar, Shira Yochelis, Eyal Capua, Raanan Carmieli, Yossi Paltiel, Ron Naaman, and Karen Michaeli. Electric Field-Controlled Magnetization in GaAs/AlGaAs Heterostructures–Chiral Organic Molecules Hybrids. *The Journal of Physical Chemistry Letters*, 10:1139–1145, 2019.

[53] I. Meirzada, N. Sukenik, G. Haim, S. Yochelis, L. T. Baczewski, Y. Paltiel, and N. Bar-Gill. Long-time-scale magnetization ordering induced by an adsorbed chiral monolayer on ferromagnets. *ACS Nano*, 15:5574–5579, 2021.

[54] Ron Naaman, Yossi Paltiel, and David H. Waldeck. Chiral molecules and the electron spin. *Nature Reviews Chemistry*, 3:250–260, 2019.

[55] Ferdinand Evers, Amnon Aharony, Nir Bar-Gill, Ora Entin-Wohlman, Per Hedegård, Oded Hod, Pavel Jelinek, Grzegorz Kamieniarz, Mikhail Lemeshko, Karen Michaeli, Vladimiro Mujica, Ron Naaman, Yossi Paltiel, Sivan Refaely-Abramson, Oren Tal, Jos Thijssen, Michael

Thoss, Jan M. van Ruitenbeek, Latha Venkataraman, David H. Waldeck, Binghai Yan, and Leeor Kronik. Theory of chirality induced spin selectivity: Progress and challenges. *Advanced Materials*, 34:e202106629, 2022.

[56] Ai-Min Guo and Qing-feng Sun. Spin-selective transport of electrons in DNA double helix. *Physical Review Letters*, 108:218102, 2012.

[57] R. Gutierrez, E. Díaz, R. Naaman, and G. Cuniberti. Spin-selective transport through helical molecular systems. *Physical Review B*, 85:081404, 2012.

[58] Ernesto Medina, Floralba López, Mark A. Ratner, and Vladimiro Mujica. Chiral molecular films as electron polarizers and polarization modulators. *EPL (Europhysics Letters)*, 99:17006, 2012.

[59] R. Gutierrez, E. Díaz, C. Gaul, T. Brumme, F. Domínguez-Adame, and G. Cuniberti. Modeling spin transport in helical fields: Derivation of an effective low-dimensional hamiltonian. *The Journal of Physical Chemistry C*, 117:22276–22284, 2013.

[60] Ai-Min Guo and Qing-Feng Sun. Spin-dependent electron transport in protein-like single-helical molecules. *Proceedings of the National Academy of Sciences*, 111:11658–11662, 2014.

[61] Ernesto Medina, Luis A. González-Arraga, Daniel Finkelstein-Shapiro, Bertrand Berche, and Vladimiro Mujica. Continuum model for chiral induced spin selectivity in helical molecules. *The Journal of Chemical Physics*, 142:194308, 2015.

[62] Joel Gersten, Kristen Kaasbjerg, and Abraham Nitzan. Induced spin filtering in electron transmission through chiral molecular layers adsorbed on metals with strong spin-orbit coupling. *The Journal of Chemical Physics*, 139:114111, 2013.

[63] Karen Michaeli, Vaibhav Varade, Ron Naaman, and David H Waldeck. A new approach towards spintronics–spintronics with no magnets. *Journal of Physics: Condensed Matter*, 29:103002, 2017.

[64] Yizhou Liu, Jiewen Xiao, Jahyun Koo, and Binghai Yan. Chirality-driven topological electronic structure of dna-like materials. *Nature Materials*, 20:638–644, 2021.

[65] L Rondin, J-P Tetienne, T Hingant, J-F Roch, P Maletinsky, and V Jacques. Magnetometry with nitrogen-vacancy defects in diamond. *Reports on Progress in Physics*, 77:056503, 2014.

[66] Marcus W. Doherty, Neil B. Manson, Paul Delaney, Fedor Jelezko, Jörg Wrachtrup, and Lloyd C.L. Hollenberg. The nitrogen-vacancy colour centre in diamond. *Physics Reports*, 528:1–45, 2013.

[67] N. B. Manson, J. P. Harrison, and M. J. Sellars. Nitrogen-vacancy center in diamond: Model of the electronic structure and associated dynamics. *Physical Review B*, 74:104303, 2006.

[68] Y. Dumeige, F. Treussart, R. Alléaume, T. Gacoin, J.-F. Roch, and P. Grangier. Photo-induced creation of nitrogen-related color centers in diamond nanocrystals under femtosecond illumination. *Journal of Luminescence*, 109:61–67, 2004.

[69] Jiangfeng Du, Fazhan Shi, Xi Kong, Fedor Jelezko, and Jörg Wrachtrup. Single-molecule scale magnetic resonance spectroscopy using quantum diamond sensors. *Reviews of Modern Physics*, 96:025001, 2024.

[70] C. Müller, X. Kong, J.-M. Cai, K. Melentijević, A. Stacey, M. Markham, D. Twitchen, J. Isoya, S. Pezzagna, J. Meijer, J. F. Du, M. B. Plenio, B. Naydenov, L. P. McGuinness, and F. Jelezko. Nuclear magnetic resonance spectroscopy with single spin sensitivity. *Nature Communications*, 5:4703, 2014.

[71] S. Ernst, P. J. Scheidegger, S. Diesch, and C. L. Degen. Modeling temperature-dependent population dynamics in the excited state of the nitrogen-vacancy center in diamond. *Physical Review B*, 108:085203, 2023.

[72] J. M. Taylor, P. Cappellaro, L. Childress, L. Jiang, D. Budker, P. R. Hemmer, A. Yacoby, R. Walsworth, and M. D. Lukin. High-sensitivity diamond magnetometer with nanoscale resolution. *Nature Physics*, 4:810–816, 2008.

[73] N. Bar-Gill, L.M. Pham, A. Jarmola, D. Budker, and R.L. Walsworth. Solid-state electronic spin coherence time approaching one second. *Nat. Commun.*, 4:1743, 2013.

[74] Lucio Robledo, Hannes Bernien, Toeno van der Sar, and Ronald Hanson. Spin dynamics in the optical cycle of single nitrogen-vacancy centres in diamond. *New Journal of Physics*, 13:025013, 2011.

[75] M. L. Goldman, A. Sipahigil, M. W. Doherty, N. Y. Yao, S. D. Bennett, M. Markham, D. J. Twitchen, N. B. Manson, A. Kubanek, and M. D. Lukin. Phonon-induced population dynamics and intersystem crossing in nitrogen-vacancy centers. *Physical Review Letters*, 114:145502, 2015.

[76] Rosa Brouri, Alexios Beveratos, Jean-Philippe Poizat, and Philippe Grangier. Photon antibunching in the fluorescence of individual color centers in diamond. *Optics Letters*, 25:1294, 2000.

[77] M J Biercuk, A C Doherty, and H Uys. Dynamical decoupling sequence construction as a filter-design problem. *Journal of Physics B: Atomic, Molecular and Optical Physics*, 44:154002, 2011.

[78] Martin Berthel, Oriane Mollet, Géraldine Dantelle, Thierry Gacoin, Serge Huant, and Aurélien Drezet. Photophysics of single nitrogen-vacancy centers in diamond nanocrystals. *Physical Review B*, 91:035308, 2015.

[79] J Harrison, M.J Sellars, and N.B Manson. Optical spin polarisation of the N-V centre in diamond. *Journal of Luminescence*, 107:245–248, 2004.

[80] Yumeng Song, Yu Tian, Zhiyi Hu, Feifei Zhou, Tengteng Xing, Dawei Lu, Bing Chen, Ya Wang, Nanyang Xu, and Jiangfeng Du. Pulse-width-induced polarization enhancement of optically pumped n-v electron spin in diamond. *Photonics Research*, 8:1289, 2020.

[81] Lucio Robledo, Lilian Childress, Hannes Bernien, Bas Hensen, Paul F. A. Alkemade, and Ronald Hanson. High-fidelity projective read-out of a solid-state spin quantum register. *Nature*, 477:574–578, 2011.

[82] M. Steiner, P. Neumann, J. Beck, F. Jelezko, and J. Wrachtrup. Universal enhancement of the optical readout fidelity of single electron spins at nitrogen-vacancy centers in diamond. *Physical Review B*, 81:035205, 2010.

[83] F. M. Stürner, Y. Liu, P.-O. Colard, M. Markham, and F. Jelezko. Magnetometry based on the excited-state lifetimes of a single nitrogen-vacancy center in diamond. *Applied Physics Letters*, 119:134001, 2021.

[84] B.J. Shields, Q.P. Unterreithmeier, N.P. de Leon, H. Park, and M.D. Lukin. Efficient readout of a single spin state in diamond via spin-to-charge conversion. *Physical Review Letters*, 114:136402, 2015.

[85] Simon Schmitt, Tuvia Gefen, Felix M. Stürner, Thomas Unden, Gerhard Wolff, Christoph Müller, Jochen Scheuer, Boris Naydenov, Matthew Markham, Sebastien Pezzagna, Jan Meijer, Ilai Schwarz, Martin Plenio, Alex Retzker, Liam P. McGuinness, and Fedor Jelezko. Submillihertz magnetic spectroscopy performed with a nanoscale quantum sensor. *Science*, 356:832–837, 2017.

[86] J. M. Boss, K. S. Cujia, J. Zopes, and C. L. Degen. Quantum sensing with arbitrary frequency resolution. *Science*, 356:837–840, 2017.

[87] L. Childress, M. V. Gurudev Dutt, J. M. Taylor, A. S. Zibrov, F. Jelezko, J. Wrachtrup, P. R. Hemmer, and M. D. Lukin. Coherent dynamics of coupled electron and nuclear spin qubits in diamond. *Science*, 314(5797):281–285, 2006.

[88] T. H. Taminiau, J. J. T. Wagenaar, T. van der Sar, F. Jelezko, V. V. Dobrovitski, and R. Hanson. Detection and control of individual nuclear spins using a weakly coupled electron spin. *Phys. Rev. Lett.*, 109:137602, 2012.

[89] T. Van Der Sar, Z. H. Wang, M. S. Blok, H. Bernien, T. H. Taminiau, D. M. Toyli, D. A. Lidar, D. D. Awschalom, R. Hanson, and V. V. Dobrovitski. Decoherence-protected quantum gates for a hybrid solid-state spin register. *Nature*, 484:82–86, 2012.

[90] Rogerio de Sousa. *Electron Spin as a Spectrometer of Nuclear-Spin Noise and Other Fluctuations*, pages 183–220. Springer Berlin Heidelberg, 2009.

[91] N.V. Vitanov, B.W. Shore, L. Yatsenko, K. Böhmer, T. Halfmann, T. Rickes, and K. Bergmann. Power broadening revisited: theory and experiment. *Optics Communications*, 199(1–4):117–126, November 2001.

[92] A. Dréau, M. Lesik, L. Rondin, P. Spinicelli, O. Arcizet, J.-F. Roch, and V. Jacques. Avoiding power broadening in optically detected magnetic resonance of single nv defects for enhanced dc magnetic field sensitivity. *Physical Review B*, 84(19), November 2011.

[93] Eike Schäfer-Nolte, Lukas Schlipf, Markus Ternes, Friedemann Reinhard, Klaus Kern, and Jörg Wrachtrup. Tracking temperature-dependent relaxation times of ferritin nanomagnets with a wideband quantum spectrometer. *Physical Review Letters*, 113:217204, 2014.

[94] M. S. Grinolds, S. Hong, P. Maletinsky, L. Luan, M. D. Lukin, R. L. Walsworth, and A. Yacoby. Nanoscale magnetic imaging of a single electron spin under ambient conditions. *Nat. Phys.*, 9:215–219, 2013.

[95] G. de Lange, Z. H. Wang, D. Ristè, V. V. Dobrovitski, and R. Hanson. Universal dynamical decoupling of a single solid-state spin from a spin bath. *Science*, 330:60–63, 2010.

[96] Linh M. Pham, Stephen J. DeVience, Francesco Casola, Igor Lovchinsky, Alexander O. Sushkov, Eric Bersin, Junghyun Lee, Elana Urbach, Paola Cappellaro, Hongkun Park, Amir Yacoby, Mikhail Lukin, and Ronald L. Walsworth. Nmr technique for determining the depth of shallow nitrogen-vacancy centers in diamond. *Physical Review B*, 93:045425, 2016.

[97] Stefan Stoll Daniella Goldfarb. *EPR Spectroscopy: Fundamentals and Methods*. John Wiley & Sons, 2018.

[98] Sharon Ruthstein, Alexey Potapov, Arnold M. Raitsimring, and Daniella Goldfarb. Double electron electron resonance as a method for characterization of micelles. *The Journal of Physical Chemistry B*, 109:22843–22851, 2005.

[99] N. Bar-Gill, L.M. Pham, C. Belthangady, D. Le Sage, P. Cappellaro, J.R. Maze, M.D. Lukin, A. Yacoby, and R. Walsworth. Suppression of spin-bath dynamics for improved coherence of multi-spin-qubit systems. *Nature Communications*, 3:858, 2012.

[100] Pengfei Wang, Sanyou Chen, Maosen Guo, Shijie Peng, Mengqi Wang, Ming Chen, Wenchao Ma, Rui Zhang, Jihu Su, Xing Rong, Fazhan Shi, Tao Xu, and Jiangfeng Du. Nanoscale magnetic imaging of ferritins in a single cell. *Science Advances*, 5:aau8038, 2019.

[101] S. Steinert, F. Ziem, L. T. Hall, A. Zappe, M. Schweikert, N. Götz, A. Aird, G. Balasubramanian, L. Hollenberg, and J. Wrachtrup. Magnetic spin imaging under ambient conditions with sub-cellular resolution. *Nature Communications*, 4:1607, 2013.

[102] Jitender Kumar, Dan Yudilevich, Ariel Smooha, Inbar Zohar, Arnab K. Pariari, Rainer Stöhr, Andrej Denisenko, Markus Hücker, and Amit Finkler. Room temperature relaxometry of single nitrogen vacancy centers in proximity to α-$RuCl_3$ nanoflakes. *Nano Letters*, 24:4793–4800, 2024.

[103] Jan M. Binder, Alexander Stark, Nikolas Tomek, Jochen Scheuer, Florian Frank, Kay D. Jahnke, Christoph Müller, Simon Schmitt, Mathias H. Metsch, Thomas Unden, Tobias Gehring, Alexander Huck, Ulrik L. Andersen, Lachlan J. Rogers, and Fedor Jelezko. Qudi: A modular python suite for experiment control and data processing. *SoftwareX*, 6:85–90, 2017.

[104] C.J. Widmann, C. Giese, M. Wolfer, D. Brink, N. Heidrich, and C.E. Nebel. Fabrication and characterization of single crystalline diamond nanopillars with NV-centers. *Diamond Relat. Mater.*, 54:2, 2015.

[105] Kimberly Jean Brown, Elizabeth Chartier, Ellen M. Sweet, David A. Hopper, and Lee C. Bassett. Cleaning diamond surfaces using boiling acid treatment in a standard laboratory chemical hood. *Journal of Chemical Health & Safety*, 26:40–44, 2019.

[106] Farid Atry and Ramin Pashaie. Analysis of intermediary scan-lens and tube-lens mechanisms for optical coherence tomography. *Applied Optics*, 55:646, 2016.

[107] Amit Finkler, Yehonathan Segev, Yuri Myasoedov, Michael L. Rappaport, Lior Ne'eman, Denis Vasyukov, Eli Zeldov, Martin E. Huber, Jens Martin, and Amir Yacoby. Self-aligned nanoscale squid on a tip. *Nano Letters*, 10:1046–1049, 2010.

[108] A. Finkler, D. Vasyukov, Y. Segev, L. Ne'eman, E. O. Lachman, M. L. Rappaport, Y. Myasoedov, E. Zeldov, and M. E. Huber. Scanning superconducting quantum interference device on a tip for magnetic imaging of nanoscale phenomena. *Rev. Sci. Instrum.*, 83:073702, 2012.

[109] Leora Schein-Lubomirsky, Yarden Mazor, Rainer Stöhr, Andrej Denisenko, and Amit Finkler. Pulsed magnetic field gradient on a tip for nanoscale imaging of spins. *Commun. Phys.*, 8:98, 2025.

[110] Loic Quéval. *"BSmag toolbox user manual"*. Dept. Elect. Eng., University of Applied Sciences Düsseldorf, Germany, 2015.

[111] Sutter Instrument. *P-2000 laser-based micropipette puller system operation manual*, 2025.

[112] Kousik Bagani, Jayanta Sarkar, Aviram Uri, Michael L. Rappaport, Martin E. Huber, Eli Zeldov, and Yuri Myasoedov. Sputtered $Mo_{66}Re_{34}$ SQUID-on-tip for high-field magnetic and thermal nanoimaging. *Phys. Rev. Applied*, 12:044062, 2019.

[113] Khaled Karrai and Robert D. Grober. Piezoelectric tip-sample distance control for near field optical microscopes. *Appl. Phys. Lett.*, 66:1842, 1995.

[114] M. Wyss, K. Bagani, D. Jetter, E. Marchiori, A. Vervelaki, B. Gross, J. Ridderbos, S. Gliga, C. Schönenberger, and M. Poggio. Magnetic, thermal, and topographic imaging with a nanometer-scale SQUID-on-lever scanning probe. *Physical Review Applied*, 17:034002, 2022.

[115] S. Bodenstedt, I. Jakobi, J. Michl, I. Gerhardt, P. Neumann, and J. Wrachtrup. Nanoscale spin manipulation with pulsed magnetic gradient fields from a hard disc drive writer. *Nano Letters*, 18:5389–5395, 2018.

[116] Edward H. Chen, Ophir Gaathon, Matthew E. Trusheim, and Dirk Englund. Wide-field multispectral super-resolution imaging using spin-dependent fluorescence in nanodiamonds. *Nano Letters*, 13:2073–2077, 2013.

[117] K. Arai, C. Belthangady, H. Zhang, N. Bar-Gill, S. J. DeVience, P. Cappellaro, A. Yacoby, and R. L. Walsworth. Fourier magnetic imaging with nanoscale resolution and compressed sensing speed-up using electronic spins in diamond. *Nature Nanotechnology*, 10:859–864, 2015.

[118] Mohammad T Amawi, Andrii Trelin, You Huang, Paul Weinbrenner, Francesco Poggiali, Joachim Leibold, Martin Schalk, and Friedemann Reinhard. Three-dimensional magnetic resonance tomography with sub-10 nanometer resolution. *npj Quantum Inf.*, 10:16, 2024.

[119] Felipe Fávaro de Oliveira, Denis Antonov, Ya Wang, Philipp Neumann, Seyed Ali Momenzadeh, Timo Häußermann, Alberto Pasquarelli, Andrej Denisenko, and Jörg Wrachtrup. Tailoring spin defects in diamond by lattice charging. *Nature Communications*, 8:15409, 2017.

[120] Dominik Schmid-Lorch, Thomas Häberle, Friedemann Reinhard, Andrea Zappe, Michael Slota, Lapo Bogani, Amit Finkler, and Jörg Wrachtrup. Relaxometry and Dephasing Imaging of Superparamagnetic Magnetite Nanoparticles Using a Single Qubit. *Nano Letters*, 15:4942–4947, 2015.

[121] S. Ali Momenzadeh, Rainer J. Stöhr, Felipe Fávaro de Oliveira, Andreas Brunner, Andrej Denisenko, Sen Yang, Friedemann Reinhard, and Jörg Wrachtrup. Nanoengineered diamond waveguide as a robust bright platform for nanomagnetometry using shallow nitrogen vacancy centers. *Nano Lett.*, 15:165–169, 2014.

[122] Gunnar W. Reginsson, Nitin C. Kunjir, Snorri Th. Sigurdsson, and Olav Schiemann. Trityl radicals: Spin labels for nanometer-distance measurements. *Chem. Eur. J.*, 18:13580–13584, 2012.

[123] M. H. Abobeih, J. Randall, C. E. Bradley, H. P. Bartling, M. A. Bakker, M. J. Degen, M. Markham, D. J. Twitchen, and T. H. Taminiau. Atomic-scale imaging of a 27-nuclear-spin cluster using a single-spin quantum sensor. *Nature*, 576:411–415, 2019.

[124] A. Molodyk, S. Samoilenkov, A. Markelov, P. Degtyarenko, S. Lee, V. Petrykin, M. Gaifullin, A. Mankevich, A. Vavilov, B. Sorbom, J. Cheng, S. Garberg, L. Kesler, Z. Hartwig, S. Gavrilkin, A. Tsvetkov, T. Okada, S. Awaji, D. Abraimov, A. Francis, G. Bradford, D. Larbalestier, C. Senatore, M. Bonura, A. E. Pantoja, S. C. Wimbush, N. M. Strickland, and

A. Vasiliev. Development and large volume production of extremely high current density $YBa_2Cu_3O_7$ superconducting wires for fusion. *Sci. Rep.*, 11:2084, 2021.

[125] Timm Swoboda, Katja Klinar, Ananth Saran Yalamarthy, Andrej Kitanovski, and Miguel Muñoz Rojo. Solid-state thermal control devices. *Adv. Electron. Mater.*, 7:202000625, 2021.

[126] E. O. Stejskal and J. E. Tanner. Spin diffusion measurements: Spin echoes in the presence of a time-dependent field gradient. *J. Chem. Phys.*, 42:288–292, 1965.

[127] Noam Shemesh, Gonzalo A. Álvarez, and Lucio Frydman. Measuring small compartment dimensions by probing diffusion dynamics via non-uniform oscillating-gradient spin-echo (NOGSE) NMR. *J. Magn. Reson.*, 237:49–62, 2013.

[128] Ruowei Yi, Yayun Mao, Yanbin Shen, and Liwei Chen. Self-assembled monolayers for batteries. *Journal of the American Chemical Society*, 143:12897–12912, 2021.

[129] Th. Wink, S. J. van Zuilen, A. Bult, and W. P. van Bennekom. Self-assembled monolayers for biosensors. *The Analyst*, 122:43R–50R, 1997.

[130] Yunsoo Choi, Hung-Vu Tran, and T. Randall Lee. Self-assembled monolayer coatings on gold and silica surfaces for antifouling applications: A review. *Coatings*, 12:1462, 2022.

[131] Milan Mrksich. Mass spectrometry of self-assembled monolayers: A new tool for molecular surface science. *ACS Nano*, 2:7–18, 2008.

[132] Hannoch Ron and Israel Rubinstein. Alkanethiol monolayers on preoxidized gold. encapsulation of gold oxide under an organic monolayer. *Langmuir*, 10:4566–4573, 1994.

[133] Jacob Henshaw, Pauli Kehayias, Luca Basso, Michael Jaris, Rong Cong, Michael Titze, Tzu-Ming Lu, Michael P Lilly, and Andrew M Mounce. Mitigation of nitrogen vacancy photoluminescence quenching from material integration for quantum sensing. *Materials for Quantum Technology*, 3:035001, 2023.

[134] Scott E. Lillie, David A. Broadway, Nikolai Dontschuk, Ali Zavabeti, David A. Simpson, Tokuyuki Teraji, Torben Daeneke, Lloyd C. L. Hollenberg, and Jean-Philippe Tetienne. Magnetic noise from ultrathin abrasively deposited materials on diamond. *Physical Review Materials*, 2:116002, 2018.

[135] S. Kolkowitz, A. Safira, A. A. High, R. C. Devlin, S. Choi, Q. P. Unterreithmeier, D. Patterson, A. S. Zibrov, V. E. Manucharyan, H. Park, and M. D. Lukin. Probing johnson noise and ballistic transport in normal metals with a single-spin qubit. *Science*, 347:1129–1132, 2015.

[136] Marzhan Sypabekova, Aidan Hagemann, Donggee Rho, and Seunghyun Kim. Review: 3-aminopropyltriethoxysilane (aptes) deposition methods on oxide surfaces in solution and vapor phases for biosensing applications. *Biosensors*, 13:36, 2022.

[137] Abraham Ulman. Formation and structure of self-assembled monolayers. *Chemical Reviews*, 96:1533–1554, 1996.

[138] Wageesha Senaratne, Luisa Andruzzi, and Christopher K. Ober. Self-assembled monolayers and polymer brushes in biotechnology: Current applications and future perspectives. *Biomacromolecules*, 6:2427–2448, 2005.

[139] Claudia Haensch, Stephanie Hoeppener, and Ulrich S. Schubert. Chemical modification of self-assembled silane based monolayers by surface reactions. *Chemical Society Reviews*, 39:2323, 2010.

[140] Limin Wang, Ulrich S. Schubert, and Stephanie Hoeppener. Surface chemical reactions on self-assembled silane based monolayers. *Chemical Society Reviews*, 50:6507–6540, 2021.

[141] D.K. Aswal, S. Lenfant, D. Guerin, J.V. Yakhmi, and D. Vuillaume. Self assembled monolayers on silicon for molecular electronics. *Analytica Chimica Acta*, 568:84–108, 2006.

[142] Mouzhe Xie, Xiaofei Yu, Lila V. H. Rodgers, Daohong Xu, Ignacio Chi-Durán, Adrien Toros, Niels Quack, Nathalie P. de Leon, and Peter C. Maurer. Biocompatible surface functionalization architecture for a diamond quantum sensor. *Proceedings of the National Academy of Sciences*, 119:e2114186119, 2022.

[143] A. Morales, M.M. Ramírez de Agudelo, and F. Hernández. Adsorption mechanism of phosphorus on alumina. *Applied Catalysis*, 41:261–271, 1988.

[144] Ravi Kumar, Saksham Mahajan, Felix Donaldson, Siddharth Dhomkar, Hector J. Lancaster, Curran Kalha, Aysha A. Riaz, Yujiang Zhu, Christopher A. Howard, Anna Regoutz, and John J. L. Morton. Stability of near-surface nitrogen vacancy centers using dielectric surface passivation. *ACS Photonics*, 11:1244–1251, 2024.

[145] Tanja D. Becke, Stefan Ness, Stefanie Sudhop, Hermann E. Gaub, Markus Hilleringmann, Arndt F. Schilling, and Hauke Clausen-Schaumann. Covalent immobilization of proteins for the single molecule force spectroscopy. *Journal of Visualized Experiments*, 138:e58167, 2018.

[146] Yuwaraj Adhikari, Tianhan Liu, Hailong Wang, Zhenqi Hua, Haoyang Liu, Eric Lochner, Pedro Schlottmann, Binghai Yan, Jianhua Zhao, and Peng Xiong. Interplay of structural chirality, electron spin and topological orbital in chiral molecular spin valves. *Nature Communications*, 14:5163, 2023.

[147] Birgit J.M. Hausmann, Mughees Khan, Yinan Zhang, Tom M. Babinec, Katie Martinick, Murray McCutcheon, Phil R. Hemmer, and Marko Lončar. Fabrication of diamond nanowires for quantum information processing applications. *Diamond and Related Materials*, 19:621–629, 2010.

[148] Hen Alpern, Konstantin Yavilberg, Tom Dvir, Nir Sukenik, Maya Klang, Shira Yochelis, Hagai Cohen, Eytan Grosfeld, Hadar Steinberg, Yossi Paltiel, and Oded Millo. Magnetic-related states and order parameter induced in a conventional superconductor by nonmagnetic chiral molecules. *Nano Letters*, 19:5167–5175, 2019.

[149] Yucheng Hao, Zhiping Yang, Zeyu Li, Xi Kong, Wenna Tang, Tianyu Xie, Shaoyi Xu, Xiangyu Ye, Pei Yu, Pengfei Wang, Ya Wang, Zhenhua Qiao, Libo Gao, Jian-Hua Jiang, Fazhan Shi, and Jiangfeng Du. Sensing orbital hybridization of graphene-diamond interface with a single spin. *arXiv*, 2305:09540, 2023.

[150] S. Felton, A. M. Edmonds, M. E. Newton, P. M. Martineau, D. Fisher, D. J. Twitchen, and J. M. Baker. Hyperfine interaction in the ground state of the negatively charged nitrogen vacancy center in diamond. *Physical Review B*, 79:075203, 2009.

[151] Adrian Negrean and Huibert D. Mansvelder. Optimal lens design and use in laser-scanning microscopy. *Biomedical Optics Express*, 5:1588, 2014.

[152] A. Cvitkovic, N. Ocelic, and R. Hillenbrand. Analytical model for quantitative prediction of material contrasts in scattering-type near-field optical microscopy. *Opt. Express*, 15:8550–8565, 2007.

[153] William R. Smythe. *Static and Dynamic Electricity*. CRC Press, 1989.

[154] C.P. Wen. Coplanar waveguide: a surface strip transmission line suitable for nonreciprocal gyromagnetic device applications. *IEEE Trans. Microwave Theory Tech.*, 17:1087–1090, 1969.

List of publications

[P1] Leora Schein-Lubomirsky, Yarden Mazor, Rainer Stöhr, Andrej Denisenko, and Amit Finkler. Pulsed magnetic field gradient on a tip for nanoscale imaging of spins. *Commun. Phys.*, 8:98, 2025.

תקציר

הגילוי של תהודה מגנטית איפשר את פיתוחן של שיטות מגוונות לחקר המבנה וההרכב של דגימות, החל ממולקולות ועד אבקות מוצקות. בתוך ארגז הכלים הזה, דימות תהודה מגנטית (MRI) חולל מהפכה ברפואה בכך שאיפשר דימות של מבנה והרכב של איברים בגוף האדם בצורה לא פולשנית. החזון להביא הישג זה אל סקלת הננומטר ולספק דימות של חלבונים בודדים ומבנים ננומטריים דוגמת שכבות מולקולריות (Monolayers) נמצא כיום במרכזו של תחום מתפתח הקרוי דימות תהודה מגנטית ננומטרית (nanoMRI).

סלקטיביות ספין התלויה בכיראליות (CISS) מתאר קשר בין הכיראליות של מולקולות אורגניות לבין כיוון הספין של האלקטרונים. תופעה זו נצפתה בעיקר בשני הקשרים: הולכת אלקטרונים דרך מולקולות כיראליות, וספיחה של מולקולות כיראליות לחומרים פרומגנטיים או למוליכי-על. מנגנון הפעולה של CISS עדיין אינו מובן במלואו, ובפרט תפקידם של קישור ספין-מסלול (SOC) ושל פני השטח הוא נושא למחקר פעיל.

מרכז חנקן-היעדרות (NV center) ביהלום, שהוא פגם אטומי במבנה הגבישי, מהווה חיישן מגנטי רגיש במיוחד שיכול לשמש כבסיס לפיתוח שיטות דימות תהודה מגנטית ננומטרית. המחקר במרכזי חנקן-היעדרות התקדם רבות בשנים האחרונות, ופיתח פרוטוקולים לגילוי ספינים אלקטרוניים וגרעיניים, תוך שימוש בפגם יחיד בתנאי טמפרטורת חדר. עם זאת, השיטות הקיימות סובלות ממגבלות קונטרסט הנובעות מהשפעה של שדות מגנטיים קבועים שאינם מיושרים עם ציר החנקן-היעדרות וכן ממגבלות בעוצמת השדה.

במסגרת עבודה זו פותחה שיטה לדימות תהודה מגנטית ננומטרית אשר מתגברת על מגבלות השימוש במגנט קבוע, ומאפשרת שליטה בזמן ובמיקום של השדה המגנטי. לשם כך פותח התקן למיקוד זרם (CFD) בצורת חוט מוליך המונח לאורך חוד קוורץ, ומבוקר באמצעות משוב AFM לקרבה לפני השטח. סימולציות תרמיות הראו כי נדרש חוד עם קצה בקוטר של כ-1300 ננומטר כדי לאפשר זרם מבלי לגרום נזק. במקביל, סימולציות שדה מגנטי הראו כי השדה שנוצר חלש דיו ואינו פוגע בקונטרסט הקריאה של מרכז החנקן-היעדרות בשונה משימוש במגנט קבוע. מדידות שבוצעו הראו כי עבור פולס עם זרם של 1.5 מילי-אמפר מתקבל גרדיאנט מגנטי של 1 מיקרו-טסלה לננומטר. נוסף, מדידה הרסנית הדגימה כי המערכת מסוגלת לעמוד בזרמים של עד 13.4 מיל-אמפר מה שמאפשר הגברה של פי 8 בעוצמת הגרדיאנט. באמצעות הגרדיאנט המגנטי הנמוך ניתן יהיה למדוד מיקומים של אלקטרונים ברזולוציה של 3.6 ננומטר. עוד נמצא כי הקרבה של החוד לפני השטח מקצר את זמן הרבי פי 3.5, מה שמאפשר מדידות קצרות יותר ללא הגברת עוצמת המיקרוגל וכך נמנע חימום מיותר. תלות המרחבית של עוצמת הרבי עשויה לשמש בעתיד לבניית גרדיאנט נוסף שיאפשר מיפוי סלקטיבי של ספינים. יתרה מכך, החוד האלקטרומגנטי שפותח עשוי לשמש גם לחקירת תופעות מגנטיות ננומטריות אחרות.

היבט נוסף שנחקר הוא חישה מגנטית של שכבות מולקולריות חד-שכבתיות (SAMs) הנספחות לפני השטח במבנה אחיד. פותחו פרוטוקולים להנחת SAM בסמוך למרכז הפגם ונמדד שכבה עם "Spin label" (סימון מגנטי של אלקטרון חופשי). נמצא כי האות מוסתר ע"י אלקטרונים טבעיים הנמצאים בפני השטח, ויש צורך בשיפור הכנת המשטח. נוסף על כך, המאפיינים המגנטיים של סיפוח מולקלות כיראליות למשטח כפי שנצפו ב CISS-הובילו לבחינת SAM כיראלי באמצעות מרכז חנקן-היעדרות. לשם כך נוצרה שכבה כיראלית בעובי 2 ננומטר על פני אלומינה שעל גבי יהלום, ונמצא כי תנודות מגנטיות אקראיות מתגברות בעקבות ספיחת השכבה הכיראלית. תוצאות אלו יכולות לשמש כבסיס למודל להסברת מנגנון-CISS אשר טרם פותח במלואו.

במבט רחב, שילוב שני הנושאים הנחקרים nanoMRI — וחקר פני שטח מולקולריים — פותח אפשרות לדימות מבנה והרכב של שכבות מולקולריות ברזולוציית ננומטר ואף מעבר לכך.